Université Mouloud MAMMERI, Tizi-Ouzou

Faculté de Génie Électrique et Informatique

Département d'Électrotechnique

ACTES

Séminaire International

MODÉLISATION ANALYTIQUE ET NUMÉRIQUE EN ÉLCTROTECHNIQUE

''ANALYTICAL AND NUMERICAL MODELLING ON ELECTROTECHNICS''

08 - 09 Juin 2024

Tizi-Ouzou, Algérie

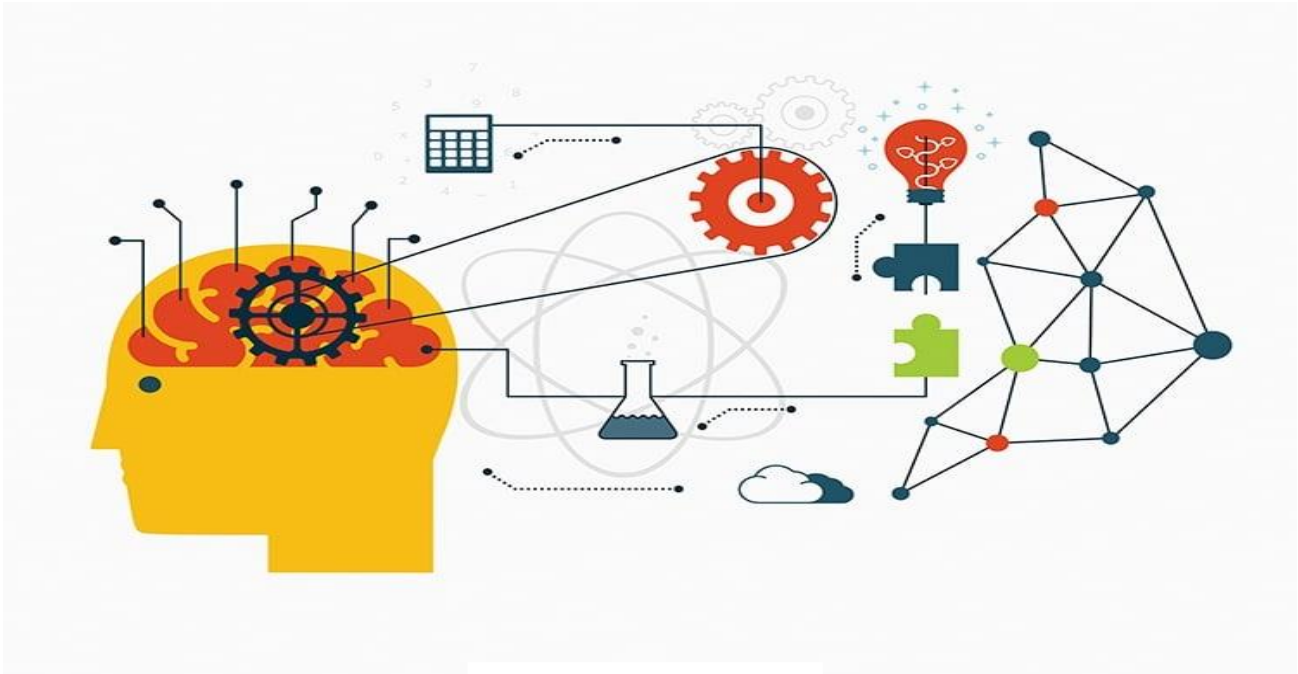

ATRST

Séminaire International

MODÉLISATION ANALYTIQUE ET NUMÉRIQUE EN ÉLCTROTECHNIQUE

''ANALYTICAL AND NUMERICAL MODELLING ON ELECTROTECHNICS''

Organisé par l'Université Mouloud MAMMERI de Tizi-Ouzou

Samedi 08 Juin – Dimanche 09 Juin 2024
Tizi-Ouzou, Algérie

Le séminaire organisé à l'Université Mouloud MAMMERI de Tizi-Ouzou, Faculté de Génie Electrique et Informatique, Département d'Electrotechnique se veut un lieu privilégié de rencontres et d'échanges des chercheurs, des ingénieurs, des étudiants et des industriels qui activent autour de la thématique traitant de la modélisation tant analytique que numérique. Il constitue aussi une occasion pour faire le point sur les développements méthodologiques nouveaux et les innovations technologiques réalisées dans le domaine de l'électrotechnique.

C'est aussi une occasion de relancer les collaborations et consolider les échanges entre chercheurs nationaux et étrangers afin d'entrevoir des perspectives de recherches dans le domaine de l'électrotechnique et du génie électrique.

Je voudrais adresser mes vifs remerciements aux participants au séminaire, aux membres du comité scientifique ainsi qu'aux membres du comité d'organisation qui ont rendu, par leurs contributions, possible la tenue de ce séminaire dans les délais requis.

Je voudrais, par ailleurs, adresser mes vifs remerciements au Recteur de l'université, aux personnels des structures de notre université à savoir : les services du rectorat, le vice rectorat chargé des relations extérieures et des activités scientifiques, la faculté de génie électrique et informatique, La faculté de médecine ainsi que le département d'électrotechnique.

.

Le Président du Comité d'Organisation
Hassane MOHELLEBI
Professeur

Président d'Honneur du Séminaire

Ahmed BOUDA, Rector of Mouloud MAMMERI University, Tizi-Ouzou, Algeria

Président du Comité Scientifique

Souri Mohamed MIMOUNE, Prof., University of Biskra, Algeria

Président du Comité d'Organisation

Hassane MOHELLEBI, Prof, Mouloud MAMMERI University of Tizi-Ouzou, Algeria

Comité Scientifique

Lotfi ALLOUI, Prof., University of Biskra, Algeria
Tarik HACIB, Prof., University of Jijel, Algeria
Mohamed Rachid MEKIDECHE, Prof., University of Jijel, Algeria
Hassane MOHELLEBI, Prof, University of Tizi-Ouzou, Algeria
Kamel SRAIRI, Prof., University of Biskra, Algeria
Abdelouahab MEKHALDI, Prof., Polytec. Nat. School, Algiers, Algeria
Zehor OUDNI, Ass. Prof, University of Tizi-Ouzou, Algeria
Souri Mohamed MIMOUNE, Prof., University of Biskra, Algeria
Bachir MAOUCHE, Prof, University of Bejaia, Algeria
Youcef, OUAZIR, Prof., University of Bab Ezzouar, Algiers, Algeria
M'Hemed RACHEK, Prof., University of Tizi-Ouzou, Algeria
Seddik BACHA, Prof., Grenoble Alpes University, G2Elab, France
Mourad AIT AHMED, Prof., IREENA, University of Nantes, France
Mohamed Fouad BENKHORIS, IREENA, University of Nantes, France
Didier TRICHET, Prof., IREENA, University of Nantes, France
Mykhailo G. PANTELIAT, Dr. Ass. Prof, National Technical University, Ukraine
Jinyi LEE, Prof, Chosun University, Korea
Yasmine GABI, Dr., Fraunhofer Institute, IZFP, Germany
Gang YAO, Prof, Shanghai Maritime University, China
Madjid R. AYATOLLAHI, Prof., Iran University of Science and Technology, Iran

Comité d'Organisation

Hassane MOHELLEBI, Président
Arezki DICHE
Zehor OUDNI
Ghania YOUSFI
Ferroudja BOUALI
Hamid MEHADDENE
M'Hemed RACHEK

SESSIONS PLÉNIÈRES

Conférence Plénière 1

Plénière 1: ''Modélisation analytique en Electronique de Puissance''

Seddik Bacha, Professeur,

G2ELab, Grenoble, France

Résumé :

Le champ applicatif de l'électronique de puissance n'a cessé de s'étendre le long de ces dernières années avec des puissances allant du mW au GW. Les applications, certes font toujours appel aux principes de base de la conversion mais nécessitent davantage de performances et de robustesse dans le sens de la stabilité.

Afin de mieux dimensionner, contrôler et simuler les convertisseurs, des modélisations particulières ont accompagné la généralisation de l'électronique de puissance et sont en général les fruits de compromis entre précision et complexité d'usage.

La conférence se propose de faire un survol des différents modèles analytiques utilisés que cela soit pour la commande, le dimensionnement ou encore les simulations rapides ou en temps différé. Les méthodes et les domaines d'applications seront explicités mathématiquement et seront corroborés par des exemples simples afin d'atteindre un public large.

Abstract :

The range of power electronics applications has continued to expand in recent years, with power ratings ranging from mW to GW. While these applications still require the basic principles of conversion, they demand greater performance and robustness in terms of stability. As a result, traditional models and controllers have reached their limits.

In order to better design, control and simulate the converters, special models have accompanied the generalization of power electronics and are generally the result of compromises between precision and complexity of use.

This conference will provide an overview of the various analytical models used for control, sizing and real-time or off-line simulation. The methods and applications will be explained mathematically and supported by simulations.

Conférence Plénière 2

Plénière 2: Stratégie de Commande des Génératrices Penta-Phasées

Mourad Ait Ahmed, Professeur

Laboratoire IREENA,
Ecole Polytechnique Nantes, France

Résumé :

Avec l'apparition des énergies soutenables les réseaux électriques vivent un grand chamboulement. En effet, on assiste à un changement de paradigme où l'on passe d'un réseau pensé et conçu de manière unidirectionnelle, du producteur au consommateur, donc radial, vers un réseau maillé composé, en plus du réseau classique, de plusieurs micro-réseaux qui sont vus autant comme producteurs décentralisés (distributed generation), composés essentiellement de photovoltaïques, microcentrale hydraulique …, que comme consommateurs. Ainsi, la gestion et le contrôle – commande du nouveau réseau se voit complétement bouleversé et doit donc introduire plus d'intelligence.

Au-delà des régulations classiques de type tension/fréquence ou du rééquilibrage du réseau, de nombreuses possibilités de services réseau s'offrent à ce type de micro réseau. En effet, l'écrêtage du pic ou le support du réseau en cas de défaut font partie des services qui peuvent être offerts par des systèmes communicants et dotés d'une capacité de flexibilité suffisante. Les systèmes auxquels nous nous intéressons sont constitués de sources d'énergies diverses : photovoltaïque, éolien, des charges contrôlables et non contrôlables et du stockage de type stationnaire ou mobile (véhicules électriques).

La commande du système Energie Soutenable – Stockage – Charges doit être une loi capable d'analyser les différentes informations afin de décider du meilleur scénario possible : besoin des charges locales, demande du réseau (assurer les services systèmes), état de production, état de stockage, prévisions météorologiques, profitabilité…

Conférence Plénière 3

Plénière 3: Visualization of Magnrtic Flux Density, for Non Destructive Testing : A Brief Technical Review From Meters to Micrometers

Prof. Jinyi Lee
Department of Electronic Engineering, Chosun University
Gwangju, Republic of Korea

Abstract—The advanced utilization of alloys and steel in critical engineering systems underscores the need for rapid, effective, and reliable nondestructive testing (NDT) methods. This study explores breakthrough NDT techniques by visualizing magnetic flux density (MFD) at the material surface, including magnetic particle inspection (MPI), magnetic flux leakage testing (MFLT), magnetic metal memory (MMM), and Eddy current testing (ECT). Significant advancements in each method are discussed, particularly how they simplify defect detection through advanced integrated image processing techniques. We present innovative approaches for quantitatively imaging MFD, utilizing arrays or scanning magnetic sensors. These techniques have been successfully applied to the nondestructive testing of express train wheels and small-bore piping in heat exchangers. Additionally, we introduce a novel method for three-dimensional vector imaging of MFD within metal grains, offering a comprehensive view of potential defects at the microstructural level

Conférence Plénière 4

Plénière 4: Modeling of Electromagnetic Phenomena Within Laminate Composite

Prof. Didier Trichet

Laboratoire IREENA,

Ecole Polytechnique Nantes, France

Abstract—Laminated composite materials with long conductive carbon fibers and thermoplastic matrix have become an essential part of modern industry. These materials require heat input during many stages in their life cycle. Today, this heat transfer is too slow and too energy-consuming limiting the large-scale development of these materials. Electromagnetic induction is a promising solution for achieving a faster non-contact energy transfer and with high energy efficiency. This contribution discusses the different stages involved in developing a numerical modelling tool for integrating the microscopic behavior of these complex composite materials in order to develop new processes. »

Conférence Plénière 5

Plénière 5 : Fraunhofer NDT System and Numerical Simulation

Dr. Yasmine Gabi

Fraunhofer Institute for Non- Destructive Testing,

Saarbrucken, Germany

Session 1 (Orale):

Numerical and Analytical Solution of PDEs (I)

- Analytical 3D Magnetic Model Calculation for Halbach PM Planar Topology Considering Edge effect
- Modeling and Simulation of Turn-to-Turn Voltage Stress of Electrical Machine Winding Fed by Steep Fronted Pulses
- Modeling of diffusion layer thickness variation of laminate in case of a current supply
- Effect of Misalignment and Coil Diameter on Wireless Power Transfer in an Electric Vehicle

3D Analytical Magnetic Model for Halbach PM Planar Topology considering the Edge Effect

Ammar Abdi , Youcef ouazir , Khaled oussama
Electrical and Industrial Systems Laboratory (LSEI)
Université des Sciences et de la Technologie Houari Boumediene
BP 32, Al-alia Bab-ezzouar, Alger , Algerie

aabdi@usthb.dz , youazir@yahoo.fr, khaled.oussama.ele@gmail.com

Abstract — In this work, a 3D analytical magnetic model to compute magnetic static field and translational motion eddy current in the conducting plate of the planar linear permanent magnet topology is developed. The main objective is to remedy the problem of the transverse edge effect, and hence improving the efficiency of analytical model and the accuracy of results. The developed model also allows fast and precise simulations of 3D magnetic phenomena, and presents an important reduction in computation time compared to 3D finite element simulation.

Keywords— Eddy currents, 3D Analytical solution, Permanent magnet, Induction heating, transverse edge effect, Halbach inductor

I. INTRODUCTION

The end effect is present in any electromagnetic device; in cylindrical structures, this effect is mainly present along the length. It is no longer the same in planar topology where end effects are present, in two directions, especially the finite width effect or edge effect, due to the closing of the currents inside the active part of the armature. Therefore taking into account the three dimensions models in the resolution is desirable [1], because the planar machines have non-negligible edge effects which can induce errors ranging, depending on the application, up to 100% [2],[3],[4] in induction heating devices with 2D-plane models.

Our study geometry Fig.1, presents important magnetic end effects that deserve to be taken into consideration in the modelling. In this model, we are only interested in dealing with the transverse end effect.

In this work, the research methodology is based on analytical development of magneto-static problem, including the electromagnetic boundary problems. A strongly 3D magnetic analytical model is developed; first, the 3D magneto-static field analytical solution derived thanks to the separation of variables technique using a magnetic scalar potential formulation, this helps to define the three-dimensional field distribution. Then, the motional eddy currents are computed using the Ampere law and the finite length extremity effects, the resulting heating power density in the moving conductive work-piece is also calculated. Finally, in order to validate the 3D developed model, the performances of a planar permanent magnet induction-heating device PMIHD (Fig. 1) are calculated. All results in 3D issued from the developed model agree well with these obtained by finite element method (3D FEM).

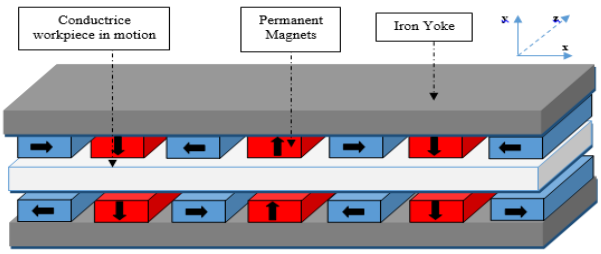

Fig.1. Planar Induction heater geometry with permanent magnets

II. MATHEMATICAL FORMULATION OF THE 3D MAGNETIC MODEL

First, we consider a resolution domain composed of air, iron and permanent magnets (Fig. 3). This assumes that the conductive part has no effect on the magnetic problem. In other words, the magnetic reaction of the currents induced in the part is not taken into account in this model. The hypothesis of considering the permeability of permanent magnets identical to that of air is close to reality if Neodymium-Iron-Boron (NdFeB, μ_r = 1,05) type magnets are used. In the region of air (B_r=0) and in the region of permanent magnets ($Br \neq 0$) we have $\mu r \rightarrow 1$. In iron considered to have infinite relative magnetic permeability ($\mu r \rightarrow \infty$).

The plane y=0 is the plane of symmetry which does not make it possible to reduce the field of study to half Fig.2.

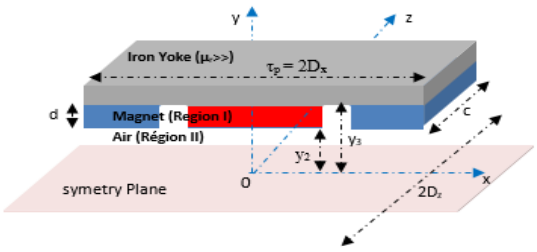

Fig.2. 3D study geometric model

Under the assumptions mentioned previously, the magneto-static problem type is very adapted for a formulation in scalar potential (U), a scalar potential formulation, we have the following equations:

$$\begin{cases} \vec{\nabla}\cdot\vec{\nabla}U = 0, & \text{in region II} \\ \vec{\nabla}\cdot\vec{\nabla}U = \dfrac{1}{\mu_r}\vec{\nabla}\cdot\vec{M}, & \text{in region I} \end{cases} \quad (1)$$

Where $\vec{M}$ is the magnetization vector of the magnets, its decomposition into double Fourier series given by:

$$\vec{M} = M_x(x,z)\vec{u}_x + M_y(x,z)\vec{u}_y \qquad (2)$$

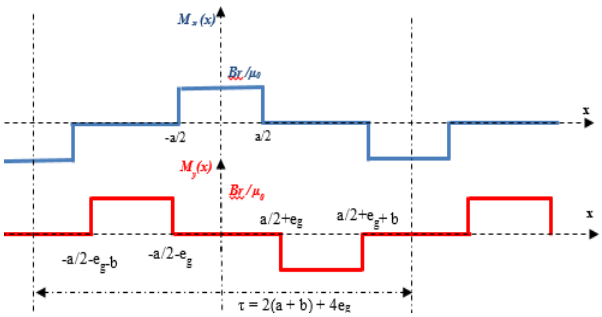

Figure .3. Magnetization (M_y) and (M_x) as a function of x

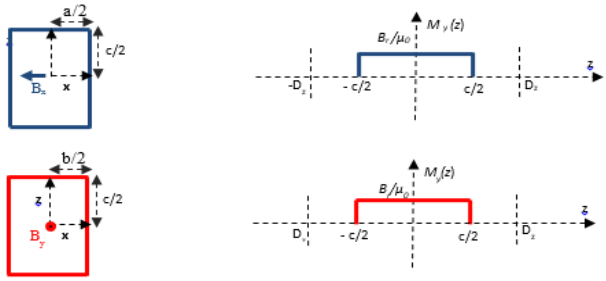

Figure .4. Magnetization (M_y) and (M_x) as a function of z

In complex representation, the magnetization is written:

$$\begin{cases} M_x(x,z) = \Re\left[\sum_{n=1}^{\infty}\sum_{m=1}^{\infty} M_{x,nm} e^{j(W_n x + W_m z)}\right] \\ M_y(x,z) = \Re\left[\sum_{n=1}^{\infty}\sum_{m=1}^{\infty} -j.M_{y,nm} e^{j(W_n x)}\right]\cos(W_m z) \end{cases} \qquad (3)$$

III. Analytical Solution of the 3D Magnetic Problem

The magnetic scalar potentials in the region of the magnets (I) and the region of the air gap (II) are the solution of the Poisson and Laplace equations respectively. In Cartesian coordinates, using the method of separation of variables, the general solutions of the magnetic scalar potential U_I and U_{II}, are given as follows:

$$U_I(x,y,z) = \Re\left[\sum_{n=1}^{\infty}\sum_{m=1}^{\infty}\left(A_{1.nm}e^{ky} + B_{1,nm}e^{-ky} - \frac{jw_n M_{x,nm}}{k^2}\right)\times e^{j(W_n x)}\times\cos(W_m z)\right]$$

$$U_{II}(x,y,z) = \Re\left[\sum_{n=1}^{\infty}\sum_{m=1}^{\infty}\left(A_{2,nm}e^{ky} + B_{2,nm}e^{-ky}\right)\times e^{j(W_n x)}\times\cos(W_m z)\right] \qquad (4)$$

Equations (4) have 4 × n × m unknown coefficients ($A_{1,nm}$, $B_{1,nm}$, $A_{2,nm}$ *and* $B_{2,nm}$) which are determined using the boundary conditions and interface. The eddy currents in an infinite conducting plate are computed using the Ampere law.

IV. Results

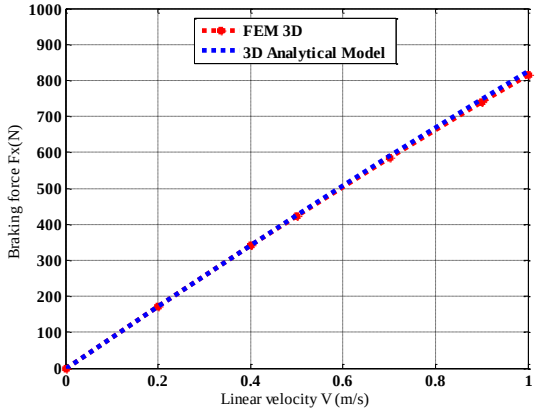

Fig. 4. Braking Force Fx(N) in the conducting workpiece versus velocity values (V).

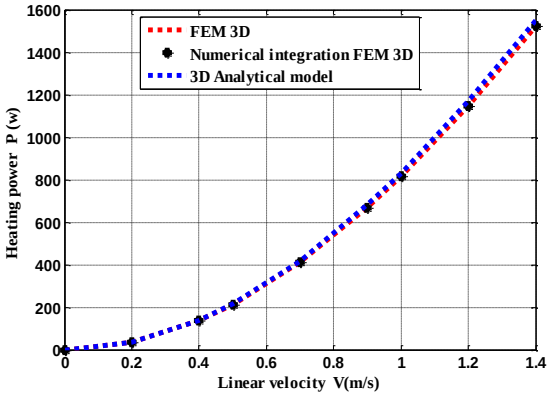

Fig. 5. Total induced Heating power in the conducting workpiece versus velocity values (V).

The analysis and comparison of the results are given in Table. I. The results obtained by the 3D analytical model with those given by the 3D FEM) showed very good agreement with respect to the results obtained by the 2D analytical, corrected analytical and 2D numerical models.

V. Conclusion

The new 3D electromagnetic analytical developed model, makes it possible to calculate the distribution of the magnetic field in 3D in the real geometry and takes into account the transverse edge effect (without approximation in 2D), and consequently it makes it possible to calculate the exact values of the different overall quantities (induced currents, induced power). The developed model presents a very small computation time compared to the simulation by finite element method (3D FEM).

References

[1] A. Diriye ; Y.Amara ; G.Barakat 'Three-Dimensional Modeling of Permanents Magnets Synchronous Machines Using a 3D Reluctance Network '' IEEE explore Pages: 2733 – 2738, 2012 XXth International Conference on Electrical Machines, september 2018, Alexandroupoli, Greece.

[2] A.Abdi, Y.Ouazir, G.Barakat, Y.Amara, "Permanent magnet linear induction heating device: newtopology enhancing performances" COMPEL, vol. 37, no.5, Octebre 2018.

[3] A. Abdi, Y. Ouazir, G. Barakat, Y. Amara, "Transient Quasi-3D Magneto-Thermal Analytical Solution in PM Induction Heating Device" COMPEL , Vol. 39 No. 5, pp. 1131-1144.mai 2020

Modeling and Simulation of Turn-to-Turn Voltage Stress of Electrical Machine Winding Fed by Steep Fronted Pulses

N. Radja and M. Rachek

Department of Electrical Engineering, Mouloud Mammeri University, BP 15000 Tizi-Ouzou, Algeria.
E-mail: n_radja@yahoo.fr, rachek_mhemed@yahoo.fr

***Abstract*—In this paper a numerical simulation method is proposed to determine the distribution of the turn-to-turn and turn-to-ground maximum voltage stress in electrical machine winding, subjected to steep fronted voltage imposed by converters. To evaluate the overvoltage stress, a lumped parameter electric equivalent circuit model of the stator winding is used. The Finite Element Method-Electromagnetic model is used to compute the distributed-circuit parameters such as resistances (R), inductances (L), and capacitances (C) of the multiconductor-insulation system which is inserted in slots. The suitability of the simulation results is validated by comparison with measurements given in [4].**

I. INTRODUCTION

The stator winding insulation plays an important role in electrical machines. The fast-fronted voltage pulses imposed by the inverter cause important over-voltages in machine windings through the electrical transients next each fast-fronted voltage steep [1]. These over-voltages are the main sources dielectric stresses leading to the aging or deterioration of the Electrical Insulation system. Numerous modeling approaches have been proposed to determine the amplitude and distribution of transient overvoltage in machine windings under fast-front pulses [2], [3].

In this paper, the Lumped parameter Electric Equivalent Circuit (LEEC) model is used to simulate the transient behavior of windings in order to determine the turn-to-turn and turn-to-ground maximum voltage of coil fed by fast fronted pulses voltages. The LEEC model consists of turn resistances (R), self and mutual inductances (L), turn-to-turn and turn-to-ground capacitances (C). The RLC parameters are computed using Finite Element Method (FEM). The (RL) parameters are obtained from the coupled model of the magnetic field equation, expressed in term of Magnetic Vector Potential (A) and the total current (I) equations. The capacitances parameters are obtained after solving the electrostatic equation, using floating potential approach. In order to validate the method proposed, the simulation results are compared with experimental results obtained by [4].

II. EQUIVALENT CIRCUIT OF A WINDING

To obtain an equivalent circuit, each turn of the winding is modeled by the elementary RLC lumped parameter equivalent cell, as shown in Fig. 1.

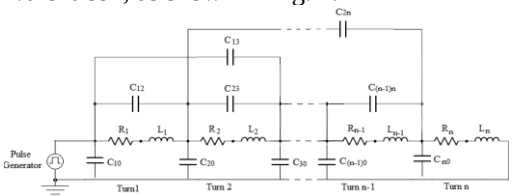

Fig. 1. Lumped parameter equivalent circuit of the n-turns in a Slot

The Finite Element formulation of magnetodynamic-total current coupled (A-I) model is used to compute the resistances (R) and inductances (L) parameters. The skin and proximity effect are considered. Considering two dimensional (x,y) cartesian plane with the source current density $\vec{J}_s$ and $\vec{A}$ have only the component in z-direction. For the N_{nodes} nodes and for the N_c conductors, the Finite Element formulation coupled (A-I) model is given by:

$$\begin{cases} \sum_{j=1}^{N_{nodes}} \iint_{\Omega} \left[\frac{1}{\mu} \left(\frac{\partial N_i}{\partial x} \frac{\partial N_j}{\partial x} + \frac{\partial N_i}{\partial y} \frac{\partial N_j}{\partial y} \right) + j\omega(\sigma + j\omega\varepsilon) N_i N_j \right] \\ \quad .A_z dxdy - \sum_{j=1}^{N_{nodes}} \iint_{\Omega} j\omega\sigma N_i G_{sz} dxdy = 0 \\ \sum_{k=1}^{N_c} \iint_{\Omega_c} \sum_{j=1}^{N_{nodes}} \left(j\omega(\sigma + j\omega\varepsilon) N_i A_z + j\omega\sigma G_{sz} \right) dxdy = I \end{cases} \quad (1)$$

Where ω the pulsation, μ the magnetic permeability, σ the electric conductivity, N_i the shape function of the finite element i and N_j is the approximation function of the magnetic vector potential A_z at node j

The resistance, self and mutual inductance are computed using the impedance formula given by:

$$R_{ij} + j\omega L_{ij} = \frac{[V_{ij}]}{[I_j]} = \left(\frac{[J_{sz}]_{ij}}{\frac{\sigma}{[I_j]}} \right)_{(i,j)=1,2,\ldots,N_c} \quad (2)$$

The indices $i = j$ are related to resistance and self inductance, and $i \neq j$ are related to mutual inductances.

The turn-to-turn and turn-to-ground capacitances are computed using an electrostatic Finite Element Method. The Finite Element formulation of electrostatic model expressed in term of electric scalar potential (V) in the two dimensional cartesian (x,y) plane is given by :

$$\sum_{j=1}^{N_{nodes}} \iint_{\Omega} \varepsilon \left(\frac{\partial N_i}{\partial x} \frac{\partial (N_j V_j)}{\partial x} + \frac{\partial N_i}{\partial y} \frac{\partial (N_j V_j)}{\partial y} \right) dxdy = \quad (3)$$

$$\int_{\Gamma_e} \varepsilon N_i \frac{\partial V(x,y)}{\partial n} \cdot \vec{n} d\Gamma_e$$

$$\begin{cases} V_0 & \text{for excited conductor} \\ 0 & \text{for unexcted conductor} \end{cases} \quad (4)$$

Where N_i the Galerkine shape function of the node $i = 1, \ldots, N_{nodes}$, N_j the approximation function of the electric scalar potential V_j at the node, V_0 the applied voltage on the Γ_d boundaries, ε is the electric permittivity.

The capacitances are computed using the stored electrostatic energy of the i^{th} and j^{th} conductors under the voltage potentials V_i and V_j respectively, such as:

$$W_e = \frac{1}{2}\int_{\Omega}\left(\varepsilon E^2\right)d\Omega = \frac{1}{2}C_{ii}V_i^{\,2} + \frac{1}{2}C_{jj}V_j^{\,2} - C_{ij}V_iV_j \qquad (5)$$

Where C_{ii} and C_{ij} are respectively the i^{th} turn and between i^{th} and j^{th} turn-to-turn capacitances.

The turn-to-ground capacitances are given by:

$$C_{i0} = C_{ii} - \sum_{j=1,\, j\neq i}^{N} C_{ij} \qquad (6)$$

III. APPLICATIONS AND DISCUSSIONS

The geometrical configuration of the coil of 11 kV motor considered in this study is shown in Fig. 2 [4]. The coil consists of nine turns placed in the slot, surrounded by a dielectric relative permittivity $\varepsilon_{r1} = 4$. Each turn of resistivity $\rho = 1.7\times10^{-8}\,(\Omega.\mathrm{m})$ is insulated with a dielectric of relative permittivity $\varepsilon_{r2} = 2.5$.

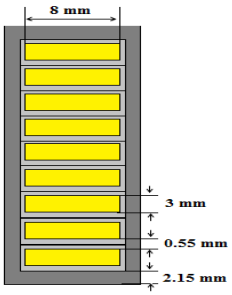

Fig. 2. Electrical machines geometrical slot-multiconductor system.

The RLC parameters obtained from the numerical simulations (FEM-Electromagnetic model) for 50Hz frequency are given in Table I.

Table I. RLC parameters obtained from FEM-Electromagnetic model

Parameter		**Value**
Turn resistance (Ω)		0.015
Turn inductance (μH)		2.24
Turn-to-turn capacitance (pF)		1303.7
Turn-to-ground capacitances	First and last turns of the coil (pF)	944.5
	Middle turns of the coil (pF)	455.5

The simulated transient turn-to-ground voltage has been evaluated by using the FEM-RLC model is shown in Fig.3. The simulations have been realized using a step voltage of 240 V for a rise time 0.024μs. The simulation circuit established by the LEEC of the multiconductor system (see Fig.1) is implemented under MATLAB/Simulink environment based on the RLC parameters obtained by FEM-Electromagnetic model.

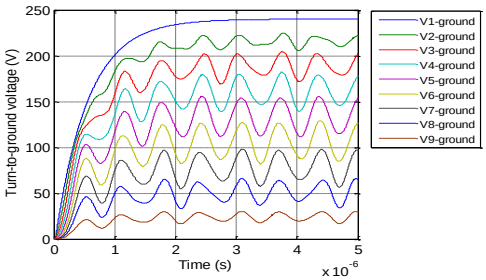

Fig.3. Turn-to-ground transient voltage distribution

The turn-to-turn transient voltages distributions in the coil are presented in Fig.4.

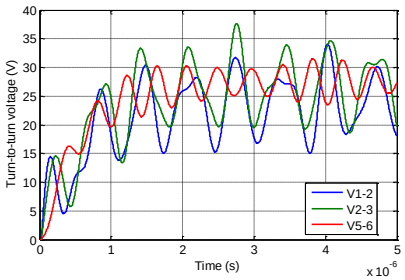

Fig.4. Turn-to-turn V1-2, V2-3 and V5–6 transient voltage distribution

In order to validate the transient model, the maximum peak turn-to-turn voltage obtained by the FEM–RLC model is compared with the measured results obtained in [4] (see Fig. 5).

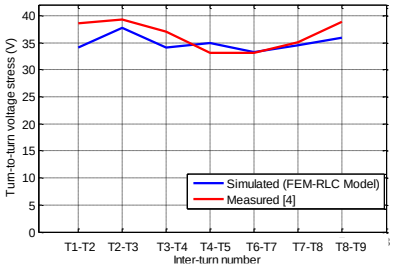

Fig.5. Comparison of the turn-to-turn voltage stress

The turn-to-turn transient voltages distributions in the coil illustrate the uneven distributions of the turn-to-turn voltage stresses, and which can be cause a significant overstresses which can lead to turn-to-turn insulation destruction. From the results obtained we note that, the electrical stress is more on the First turns and on the last turns of the coil are characterized by a higher value in comparison to the others turns due to their position in the slots. The simulation gives results in good agreement with measurement given by [4].

IV. CONCLUSION

In this paper, the turn-to-turn and turn-to-ground maximum voltage stress in electrical machine winding subjected to steep fronted voltage are analyzed and shown. The RLC parameters of turns of the coil were calculated using Finite Element Method. The knowledge of the magnitude and waveform of the transient overvoltage is very important for analyzing and to assess the turn-to-turn and turn-to-ground insulations. The simulation gives results in good agreement with measurement given by [4].

REFERENCES

[1] M. K. Hussain, P. Gomez, "Optimisation Dielectric Design of Stator Medium Voltage Induction Machines Fed by Fast Front Pulses", IEEE Trans. Electri. Dielec. Insul, Vol. 24, No. 2, pp. 837-846, 2017.

[2] G. Lupo, C. Petrarca, M. Vitelli,V. Tucci, "Multiconductor transmission line analysis of steep-front surges in machine windings," IEEE Trans. Dielectr. Electr. Insul.,Vol. 9, No. 3, pp. 467–478, 2002.

[3] R.S. Ferreira, A.C. Ferreira, "Transient model to study voltage distribution in electrical machine windings considering the rotor", Elsevier, Electric Power Systems Research 195 (2021) 107155.

[4] M. Sajid, B. Singhand and M. Suryakalavathi, "Experimental and Theoretical Investigation of Transient Voltage Distribution in an 11 kV Industrial Motor Winding", Elsevier, Energy Procedia 117 (2017) 321-328.

Modeling of diffusion layer thickness variation of laminate in case of a current supply

YOUSFI Ghania
Department of Electrotechnics
Mouloud Mammeri University
Tizi-Ouzou, Algeria
Email: ghania.yousfi@yahoo.fr
ORCID: 0009-0009-2674-8299

MOHELLEBI Hassane
Department of Electrotechnics
Mouloud Mammeri University
Tizi Ouzou, Algeria
Email:hass.2000@yahoo.com
ORCID: 0000-0003-3661-1690

Gabi Yasmine
Fraunhofer Institute
IZFP, Allemagne
Email:.yasmine.gabi@izfp.fraunhofer.de
ORCID: 0000-0002-6148-4008

***Abstract*—This paper discuses the modeling of the diffusion layer thickness variation impact on eddy currents signals. The numerical modeling of laminate with the diffusion layer is realized using finite elements code developed under Matlab environment. The solving of the 2D electromagnetic equation, in (r,z) plane, is performed by considering magnetic permeability variation of diffusion layer. A comparison between the simulation results and experimental signals shows a good agreement.**

Keywords—laminated material, diffusion layer thickness, finite elements, eddy currents signals, experimental results.

I. INTRODUCTION

Multilayer materials are appreciated for their modular properties that conventional materials cannot offer. However, knowledge of their behavior is necessary to be able to fully their potential [1].In this work goal is the modeling of a multilayer material, taking into account the variation of diffusion layer thickness and evaluate the impact on the eddy current signals under several excitation frequencies.

II. ELECTROMAGNETIC EQUATION AND RESOLUTION METHOD

A. 2D Electromagnetic equation

The modeling of the electromagnetic problems is based on Maxwell's equations. From Maxwell's equations, in case of 2D axisymmetric problem, the electromagnetic phenomenon, in (r,z) plane, is governedby equation below:

$$\frac{\partial}{\partial r}\left(\frac{\upsilon}{r}\frac{\partial(rA_\varphi)}{\partial r}\right)+\frac{\partial}{\partial z}\left(\frac{\upsilon}{r}\frac{\partial(rA_\varphi)}{\partial z}\right)-j\frac{\sigma\omega}{r}(rA_\varphi)=-J_S \quad (1)$$

Where A is the magnetic vector potential, υ is the magnetic reluctivity, J_s(A/m^2) is the source current density and σ(S/m) is the electrical conductivity.

B. Finite elements formulation of 2D electromagnetic equation

The finite elements formulation of the 2D electromagnetic equation (1), with Green theorem and by considering homogeneous boundaries conditions, becomes:

$$\iint_\Omega \upsilon\left(\frac{\partial\phi_i}{\partial r}\frac{\partial A}{\partial r}+\frac{\partial\phi_i}{\partial z}\frac{\partial A}{\partial z}\right)\frac{drdz}{r}+j\omega\iint_\Omega \sigma\,\phi_i A\frac{drdz}{r}=\iint_\Omega \phi_i\, J_{s\varphi}\, drdz \quad (2)$$

ϕ_i is the projection function at node ''i'', ϕ_j is the shape function at node "j".

After arrangements we obtain the algebraic system to solve:

$$[M][A]+j\omega[L][A]=[F] \quad (3)$$

[M], [L] and [F] are the matrices of the first and the second terms of (2) and a vector of the right hand of (2).

III. SIMULATION AND RESULTS

The geometric configuration consists of two coils, transmitter and receiver, placed above a multi-layer area (Fig. 1). The first coil consists of 100 turns and excited by a signal of amplitude about 3mA. The second have 300 turns.

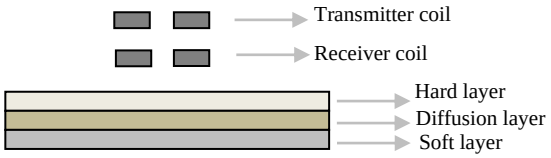

Fig.1. Geometric characteristics of the problem

Table I. Physical and geometrical parameters

	Characteristics
Transmitter and Receiver coil	innerradius: 2mm, outerradius: 4mm width: 2mm electrical conductivity: 59*10^{6}S/m
Hard layer	width:22µm, length: 42 mm , μ_r=230 electrical conductivity: 6.67 *10^6 S/m
Diffusion layer	width : variable, length: 42mm, μ_r:variable electrical conductivity: 3.57 *10^6 S/m
Soft layer	width:1mm, length: 42 mm, μ_r=450 electrical conductivity: 6.67 *10^{6}S/m

A. Solving geometry and boundary conditions

The described geometry in Fig.2 represents the domain resolution of the electromagnetic problem obtained by considering symmetry of the physical phenomenon.

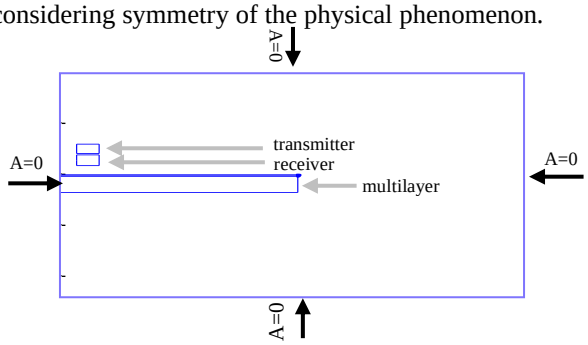

Fig.2. Studied domain and boundary conditions

The meshed domain of the investigated problem is represented in Fig. 3. The number of nodes is 20576 and the number of triangle is about 41059.

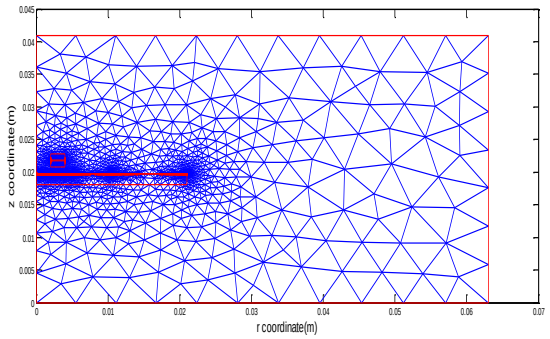

Fig.3. Meshed domain representation

B. *Magnetic vector distribution*

The magnetic vector potential distribution is shown in Fig.4. Then the voltage U around detection coils computed

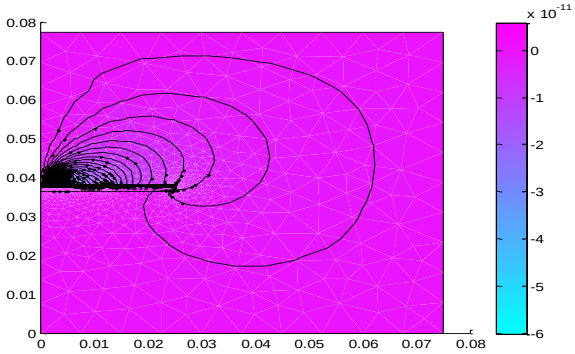

Fig.4. Magnetic vector potential distribution (Real part)

using the relationship below [2]:

$$\vec{B} = \vec{\nabla} \wedge \vec{A} \tag{4}$$

$$U = -\frac{d}{dt}\iint_S \vec{B}.\vec{dS} \tag{5}$$

The following Fig.5 are profiles from experimental signals and calculated via FEM model. The profile denotes the sensitivity of diffusion thickness layer on eddy current signals for various eddy current frequencies.

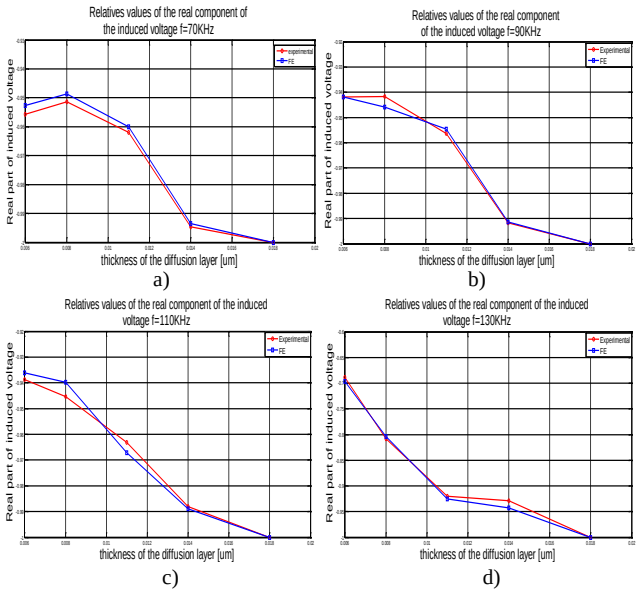

a) b) c) d)

Fig.5. Relatives values of the real component of the induced voltage:

a) f=70 kHz
b) f=90 kHz
c) f=110 kHz
d) f=130 kHz

The numerical calculation is realized for different thicknesses of diffusion layer, which varies in the interval [6-18] µm under different excitation frequencies. The results in Fig.5 and Fig.6 denote the relative values of the real part of the voltage for frequencies f=70 kHz, f=90 kHz, f=110 kHz, f=130 kHz and variation of modulus voltage.

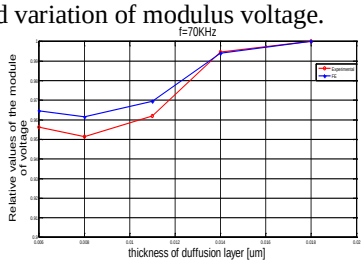

Fig.6. Modulus of induced voltage (Relatives values, f=70 kHz)

The comparison between FEM simulation and experimental data [3] shows good trend with high accuracy. The voltage drops with increasing diffusion layer thickness (Fig.7) while permeability increases with increasing diffusion layer thickness (Fig.8)

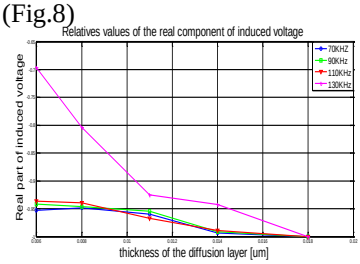

Fig.7. Induced voltage variation with diffusion layer thickness (Real part for different values of frequency)

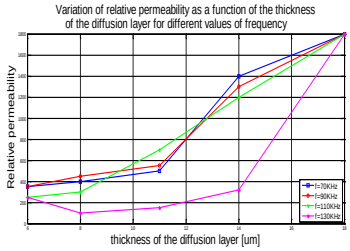

Fig.8. Evolution of magnetic permeability as a function of thickness for different values of frequency

We notice that the magnetic permeability corresponding to frequency of 130 kHz is too small comparing to the others frequencies which could be explained by the impotence of the skin depth (Fig. 8).

I. CONCLUSION

In this paper, the modeling of multi-layer material layer was represented in FEM code. The impact of diffusion layer thicknesses is investigated. The calculated and measured eddy current profiles were compared. A good agreement between data from simulation and experimental data with an accuracy of eddy currents signals.

II. REFERENCES

[1] H.Mohellebi, G.Yousfi, "Evaluation of the non-linear equivalent magnetic permeability of stratified material", IIPhDW, Warsaw, Lublin, Zielona Gora, 2011, Poland, ISBN 978-83-61956-02-0

[2] K.Sidi Ahmed, B.Maouche, Y.Gabi, L.Alloui, B.Strab, B.Wolter, M.Feliachi, "Numerical simulation and experimental investigation of laser hardening depth investigation via 3MA-eddy current technique" Journal of Magnetism and Magnetic Materials 550(2022)169046.

[3] G. Yousfi, Internal Report, Decmber 2023, Tizi Ouzou University, Algeria

Effect of Misalignment and Coil Diameter on Wireless Power Transfer in an Electric Vehicle

Ihab Anis Zergua
Department of Electrical Engineering
University of Jijel
Jijel, Algeria
ihab.zergua@univ-jijel.dz

Naamane Mohdeb
Department of Electrical Engineering
University of Jijel
Jijel, Algeria
mohdeb.naamane@gmail.com

Nabil Ikhlef
Department of Electrical Engineering
University of Jijel
Jijel, Algeria
ikhlefnabil@yahoo.fr

***Abstract*— Electric vehicles (EVs) have emerged as a key component of the strategy to combat climate change, owing to their ability to use renewable energy, therefore decarbonizing the transport sector which accounts for a large share of global greenhouse emissions. However, despite their growing popularity, they continue to face certain limitations, such as bulky charging stations, heavy batteries and long charging durations. The wireless charging of EVs can offer a solution to these problems, but its efficiency remains largely affected by the misalignment and air gap between the primary and secondary coils. This paper aims to study the impact of misalignment and outer coil diameter on wireless power transfer efficiency, to come up with a robust inductively coupled wireless charging system. The results show that for all air gaps and misalignment conditions, coils with a larger outer diameter offer a more optimal wireless power transfer.**

Keywords*— Wireless power transfer, coupling coefficient, electric vehicles, misalignment, coil diameter

I. INTRODUCTION

In the last decade, the use of electric vehicles (EVs) has drastically increased, due to their environmentally friendly nature compared to combustion engine vehicles (ICEVs) which rely on gasoline to function, which causes the release of greenhouse gases into the atmosphere, contributing to climate change [1, 2].

However, EVs face certain limitations that prevent them from unlocking their full potential, namely their reliance on conventional wired charging methods which suffer from drawbacks such as the need for long charging cables that are subject to subject to wear and tear, and which expose consumers to the risk of electrocution and tripping [3, 4]. In addition to requiring space above ground for charging stations to be placed. In contrast, a wireless charging pad can be placed underground, and offers more convenience, robustness and safety [5, 6].

In order to improve the performance of wireless power transfer (WPT), many researchers have taken an interest in studying the effects of misalignment and relative coil positions on the power transfer efficiency. Ghazizadeh et al. [7], as well as Chatterjee et al. [8], studied the effects of misalignment and coil geometry on WPT, concluding that a circular coil design offers a more robust power transfer for a wider range of misalignment conditions. Furthermore, Lo et al. [9] have determined that a coil with a greater outer diameter is able to perform better than the one with smaller outer diameter at different air gaps. In addition, Thein et al. [10] investigated the impact of different coil designs on WPT, finding that the power transfer efficiency is enhanced by increasing the number of turns and spacing between each turn for both coils.

In this context, the present work aims to use numerical analysis tools, namely the MATLAB software, to study the impact of various misalignment parameters, such as the tilt angle, air gap and lateral misalignment, for various coil diameters, on wireless power transfer in an electric vehicle.

II. METHOGOLOGY

A. Equations

The performance of a WPT system is largely affected by its coupling coefficient *k* [11], which is in a linear relationship with the mutual inductance *M*, as shown in (1), with L_1 and L_2 being the self-inductance of the primary and secondary coils, respectively:

$$k = \frac{M}{\sqrt{L_1 . L_2}} \tag{1}$$

The coil inductance *L* is calculated using the method elaborated by Mohan et al. [12]:

$$L = \frac{\mu N^2 d_{aveg} c_1}{2} \left(ln\left(\frac{c_2}{\rho}\right) + c_3\rho + c_4\rho^2\right) \tag{2.1}$$

where d_{avg} is the average diameter and ρ the fill ratio, defined in (2.2) and (2.3), respectively:

$$d_{avg} = \frac{d_{out} + d_{in}}{2} \tag{2.2}$$

$$\rho = \frac{d_{out} - d_{in}}{d_{out} + d_{in}} \tag{2.3}$$

while the coefficients c_i depend on the coil geometry, and in the case of the circular geometry used in this paper, they have the values shown in Table I.

TABLE I. CURRENT SHEET EXPRESSION COEFFICIENTS FOR CIRCULAR GEOMETRY

C1	C2	C3	C4
1	2.46	0	0.20

The coil size is calculated using (3):

$$d_{out} = d_{in} + 2 \cdot [N \cdot d_w + (N - 1) \cdot s] \quad (3)$$

where d_{out} is the outer diameter, d_{in} is the inner diameter, N the number of turns, d_w the wire diameter and s the spacing between turns.

A MATLAB program was developed to resolve the above governing equations, the results of which will be discussed in the next section.

B. *Picking the coils*

From the SAE J2954 standard [13], the maximum outer diameter for the coil used in the wireless charging of an EV is set to be 330 to 360 mm [14], with the air gap between the two coils being ideally half this diameter, the number of turns to achieve an optimal power transfer is between 10 and 20 turns [15].

In [8], it is shown that decreasing the spacing between each turn of the coil increases the mutual inductance, which is important to establish a better coupling coefficient. Hence, a spacing of 1 mm will be used in this paper. In addition to this, the wire diameter is chosen to be 4 mm, with a standard frequency of 85 kHz according to the SAE J2954 standard [13].

Four coils were picked to study the effect of the coil diameter on the coupling coefficient for various misalignment conditions, one transmitter coil made up of 20 turns, and three receiver coils made up of 10 turns each and with varying diameters. The characteristics of the coils are shown in Table II.

TABLE II. COIL CHARACTERISTICS

Coil Parameters	Transmitter Coil	Receiver Coil 1	Receiver Coil 2	Receiver Coil 3
Outer diameter [mm]	300	200	300	400
Inner diameter [mm]	100	100	200	300
Spacing [mm]	1	1	1	1
Wire diameter [mm]	4	4	4	4
Number of turns	20	10	10	10
Self-inductance [µH]	82.88	19.26	39.69	61.83

The coil pairs used in the study as well as their diameters are depicted in Fig. 1.

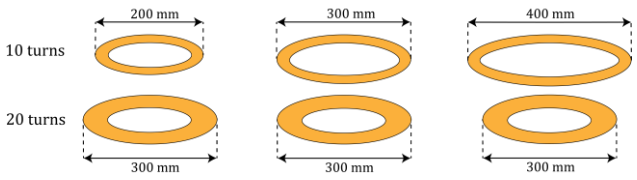

Fig. 1. Coil pairs and their outer diameters

C. *Misalignment types*

The three types of misalignment that were studied are shown in Fig 2.

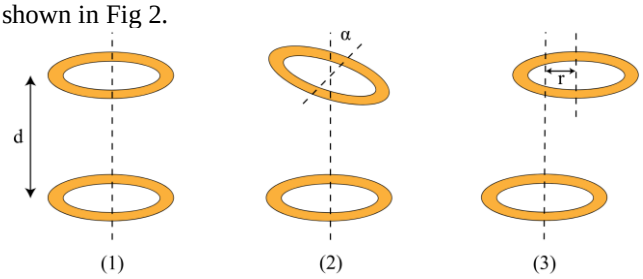

Fig. 2. Types of misalignment studied, (1) vertical misalignment, (2) angular misalignment, (3) lateral misalignment

1. Air gap: which represents the vertical distance separating the coils, also referred to as the vertical misalignment.

2. Tilt angle: which represents the angular misalignment between the two coils.

3. Lateral misalignment: which represents the horizontal displacement of coils with respect to each other.

III. RESULTS AND DISCUSSION

A. *Tile Angle Effect*

To determine the effect of the tilt angle on the coupling coefficient, for each of the three coil pairs, angles ranging from 0° to 90° were examined, at a fixed air gap of 150 mm. The results are shown in Fig. 3 and 4.

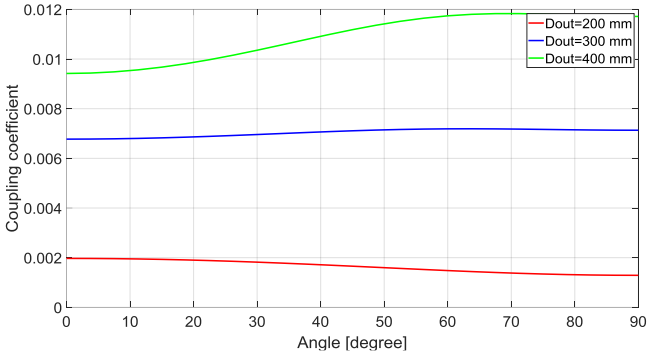

Fig. 3. Coupling coefficient against tilt angle for various coil diameters

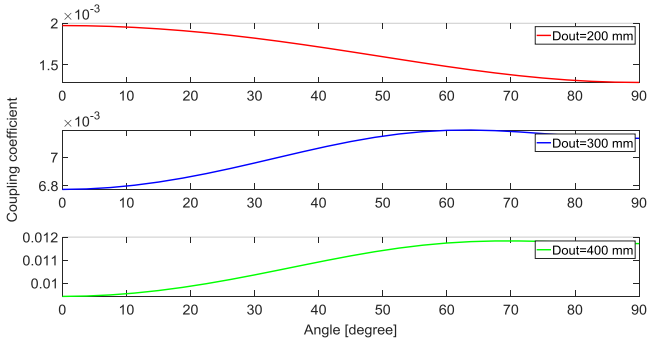

Fig. 4. Individual breakdown of the coupling coefficient against tilt angle for each coil diameter

Figures 3 and 4 show that, for all tilt angles, higher coil diameters offer a higher coupling coefficient. However, in the cases of 300 and 400 mm diameters, the coupling increases when increasing the tilt angle, while in the case of the 200 mm diameter, the coil diameter and tilt angle have an inverse relationship.

B. Air Gap Effect

The effect of air gaps ranging from 10 to 200 mm were studied for the three coil pairs, while maintaining a perfect lateral and angular alignment between them. The results are shown in Fig. 5.

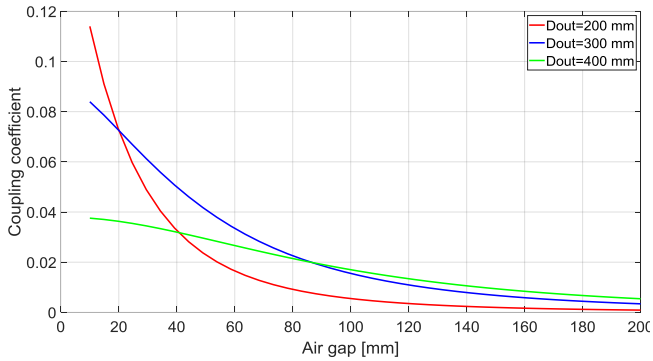

Fig. 5. Coupling coefficient against air gap for various coil diameters

Figure 5 shows that the coupling coefficient decreases hyperbolically with respect to the air gap in the cases of the 200 mm and 300 mm outer coil diameters, and more linearly in the case of a 400 mm diameter. The 200 mm diameter offers the theoretical maximum coupling coefficient for air gaps under 20 mm, while the 300 mm diameter offers the highest coupling coefficient for air gaps ranging between 20 and 86 mm. More importantly, for air gaps exceeding 86 mm, which correspond to the air gaps found in practice in EVs (generally between 100 and 200 mm), a 400 mm outer diameter offers the highest coupling coefficient.

C. Lateral Misalignment Effect

The effect of lateral misalignment was studied by shifting the relative position of the two coils off center between 0 and 300 mm, while maintaining a fixed air gap of 150 mm. The results are shown in Fig. 6.

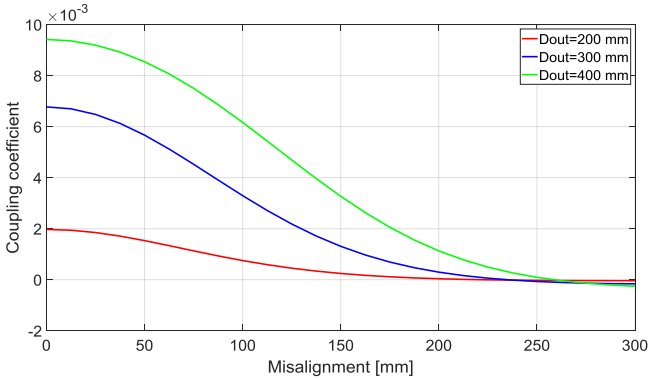

Fig. 6. Coupling coefficient against lateral misalignment for various coil diameters

Figure 6 shows that for all lateral misalignment ranges, higher outer coil diameters offer higher coupling coefficients, with the 400 mm diameter resulting in the the highest coupling coefficient, and the 200 mm diameter being the lowest. The coupling coefficients for all coil diameters converge to zero for lateral misalignment distances above 220 mm.

IV. Conclusion

In this paper, the effects of angular, vertical and lateral misalignment as well as coil diameter on wireless power transfer in an electric vehicle were studied using an analytical model. It has been concluded that:

- A larger outer coil diameter leads to a higher coupling coefficient.
- The relationship between the coupling coefficient and the tilt angle varies depending on the outer coil diameter.
- The coupling coefficient decreases when increasing the air gap.
- The coupling coefficient decreases when increasing lateral misalignment.

References

[1] E. Valsera-Naranjo, A. Sumper, P. Lloret-Gallego, R. Villafafila-Robles, A. Sudria-Andreu, “Electrical Vehicles: State of Art and Issues for their Connection to the Network”, Proceedings of the 10th International Conference on Electrical Power Quality and Utilisation, Lodz, Poland, September 2009, pp. 1 – 3.

[2] A. Mahesh, B. Chokkalingam, L. Mihet-Popa, “Inductive Wireless Power Transfer Charging for Electric Vehicles – A Review”, IEEE Access, Vol. 9, October 2021, pp. 137667 – 137713.

[3] J. M. Miller, O. C. Onar, M. Chinthavali, “Primary-Side Power Flow Control of Wireless Power Transfer for Electric Vehicle Charging”, IEEE Journal of Emerging and Selected Topics in Power Electronics, Vol. 3, No. 1, March 2015, pp. 147 – 162.

[4] S. Hasanzadeh, S. Vaez-Zadeh, A.H. Isfahani, “Optimization of a contactless power transfer system for electric vehicles”, IEEE Trans. Veh. Technol. 2012, 61, 3566–3573.

[5] W. Li, H. Zhao, S. Li, J. Deng, T. Kan, C.C. Mi, “Integrated LCC compensation topology for wireless charger in electric and plug-in electric vehicles”, IEEE Trans. Ind. Electron. 2014, 62, 4215–4225.

[6] L. Zhao, D.J. Thrimawithana, U.K. Madawala, A.P. Hu, C.C. Mi, “A misalignment-tolerant series-hybrid wireless EV charging system with integrated magnetics”. IEEE Trans. Power Electron. 2018, 34, 1276–1285.

[7] S. Ghazizadeh, K. Ahmed, M. Seyedmahmoudian, S. Mekhilef, J. Chandran and A. Stojcevski, “Critical Analysis of Simulation of Misalignment in Wireless Charging of Electric Vehicles Batteries,” Batteries, 9, 106, 2023.

[8] S. Chatterjee, A. Iyer, C. Bharatiraja, I. Vaghasia and V. Rajesh, “Design Optimisation for an Efficient Wireless Power Transfer System for Electric Vehicles,” Energy Procedia, vol. 117, pp. 1015-1023, 2017.

[9] Kon Wui Lo Duncan, Juwono Filbert, Kitt Wong Wei and Ming Chew Ing, “A study on transmission coil parameters of wireless power transfer for electric vehicles,” Serbian Journal of Electrical Engineering, vol. 19, iss. 2, pp. 129-145, 2022.

[10] M. E. Thein, J. Charoensuk, M. Masomtob, W. Onreabroy and A. Kaewpradap, “Investigation of power transfer efficiency: utilizing different coil designs in wireless charging of electric vehicles,” IOP Conference Series: Materials Science and Engineering, vol. 1137, 012019, 2021.

[11] G. Ke, Q. Chen, L. Xu, S. -C. Wong and C. K. Tse, “A model for coupling under coil misalignment for DD pads and circular pads of WPT system,” 2016 IEEE Energy Conversion Congress and Exposition (ECCE), Milwaukee, WI, USA, 2016, pp. 1-6

[12] Sunderarajan S. Mohan, Maria del Mar Hershenson, Stephen P. Boyd, and Thomas H. Lee, “Simple Accurate Expressions for Planar Spiral Inductances”, IEEE Journal of Solid-State Circuits, vol. 34, no. 10, october 1999.

[13] "Wireless Power Transfer for Light-Duty Plug-In/Electric Vehicles and Alignment Methodology," ed: SAE TIR J2954_201605, 2016.

[14] Y. Yang, M. El Baghdadi, Y. Lan, Y. Benomar, J. Van Mierlo, O. Hegazy, “Design Methodology, Modeling, and Comparative Study of Wireless Power Transfer Systems for Electric Vehicles”, Energies, Vol. 11, No. 7, July 2018, pp. 1716.

[15] J. Liu, Z. Wang, M. Cheng, “Optimization of Coils for Wireless Power Transfer System in Electric Vehicle”, Proceedings of the 21st International Conference on Electrical Machines and Systems (ICEMS), Jeju, South Korea, October 2018, pp. 2161-2165.

Session 2 (Orale):

Inductive, Smart sensors and actuators

- Inspection of surface defects on a composite material by the stochastic finite element model
- Contribution to Characterization of Unidirectional Carbon Fiber Reinforced Plastic (CFRP) Using High-Frequency Eddy Current Profiling Device Technology
- Capteur gravimétrique à ondes acoustiques de surface (SAW)
- Numerical modelling of micromagnetic methods in 3MA linear and nonlinear Eddy current methods

Inspection of surface defects on a composite material by the stochastic finite element model

Thinhinane MAHMOUDI [1st]
dept.Electrotechnical
University Mouloud Mammeri
Tizi Ouzou, Algeria
mahmoudi.thinhinane@gmail.com

Zehor MOHELLEBI eps OUDNI [2nd]
dept.Electrotechnical
University Mouloud Mammeri
Tizi Ouzou, Algeria
z_mohellebi@yahoo.fr

***Abstract*— The detection and characterization of defects on a carbon fiber composite material by eddy current non-destructive testing process using a numerical method based on intrusive stochastic finite elements is presented in this paper. The electrical conductivity is considered as a random variable of the Gaussian type characterized by an average value and a standard deviation, distributed over the risk zone presenting the defect in the material.**

A stochastic finite elements code is made under Matlab environment offer the 2D electromagnetic equation resolution, in axisymmetric hypotheses, this conduces to obtain the magnetic vector potential (A) across the solving domain. The impedance of the differential sensor used is then calculated by integrating the values of the magnetic vector potential. Scanning material surface encompassing the defective area allows for the assessment of impedance variation for various standard deviation of the random variable and then indicate a presence or absence of faults.

Keywords*— *composite material, intrusive stochastic finite element, eddy current, impedance, electrical conductivity.

I. INTRODUCTION

Characterization refers to a complete process for studying the structure, proprieties and behavior of composite materials. Overall, this is a crucial process with which one can build a scientific understanding of materials, it also involves the characterization of defects occurring during the manufacturing process or during their life cycle. It's very important to ensure security and quality of carbon fiber composite materials cause nowadays they cover a wide range of fields like aerospace, electrical, rail transportation, aviation [1] and offer many advantages.

Commonly, composite materials are made up of at least two distinct materials which are bound together complementing each other and provide better performance than one constitutes element taken individually. They are composed of reinforcements surrounded by a matrix [1][2][3]. There are essentially three types composites structures: monolayer [4] sandwich or laminate [5][6]. Several techniques aim to characterize these materials [7] among them non-destructive testing NDT such as ultrasonic testing, radiography, eddy current [8][9]. Being electrically conductive, the carbon fiber composite materials CFRP can be inspected by eddy current non-destructive testing NDT-EC [10] which is used in the present work with numerical modeling study for the detection, characterization of defects in CFRP.

A lot of methods for modeling and simulating composite material defects using NDT-EC are found in literature. We have opted in this paper to the stochastic finite element method SEFM, a random approach, the development of the answer is based on the polynomial chaos whose input are the random physical properties [13] considering the longitudinal electrical conductivity σ_L as the random variable of Gaussian type oriented along the x-axis. The key challenge in stochastic finite element method SFEM is the modeling of the uncertainty characterizing the system parameters (input).

II. STOCHASTIC ELECTROMAGNETIC MODEL

A. Deterministic Electromagnetic Model

- Maxwell equations:

$$div(\vec{D}) = \rho \quad (1)$$

$$rot(\vec{E}) = -\frac{\partial \vec{B}}{\partial t} \quad (2)$$

$$div(\vec{B}) = 0 \quad (3)$$

$$rot(\vec{H}) = \vec{J} + \frac{\partial \vec{D}}{\partial t} \quad (4)$$

- Middle relations:

$$\vec{D} = \varepsilon \vec{E} \quad (5)$$

$$\vec{B} = \mu \vec{H} \quad (6)$$

$$\vec{J} = \sigma \vec{E} \quad (7)$$

- Electromagnetic formulation for determinist problem:

$$\vec{\nabla} \wedge (\nu \vec{\nabla} \wedge \vec{A}) + j\sigma\omega\vec{A} = \vec{J_s} \quad (8)$$

B. Electrical conductivity

The electrical conductivity in this type of materials is expressed with a tensor by conductivity in longitudinal direction σ_L , transverse direction σ_T (there are contacts between the fibers), and according to the thickness σ_Z [11] [12], the electrical conductivity of a ply according to referential is expressed by:

$$\sigma_{pli} = \begin{bmatrix} \sigma_L & 0 & 0 \\ 0 & \sigma_T & 0 \\ 0 & 0 & \sigma_Z \end{bmatrix} \quad (9)$$

Ohm's low is then written like:

$$\overrightarrow{J_{pli}} = \sigma_{pli} \overrightarrow{E_{pli}} \quad (10)$$

III. APPLICATION AND RESULTS

The application structure consists of a composite CFRP having dominant longitudinal conductivity, presenting a defect as showing Figure 1. The area of uncertainty is represented by the change of distribution on the electrical conductivity. Non-destructive eddy current testing using a sensor moving towards the abscissa axis placed parallel to the material is used for its detection.

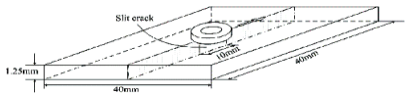

Fig 1. NDT-EC device Coil and CFRP plate with crack.

The electrical conductivity is randomly distributed over the material for two different standard deviations, one being 10% of the average value of the electrical conductivity and the other 90%, the aim being to highlight the variation of the impedance in the area suspected to have a fault. The impedance Z is then calculated. The results obtained are represented by the figures [2-5] where: figure 2 shows us one of the three stochastic solutions of the distribution of the potential vector A. The distribution seems homogeneous when moving the sensor.

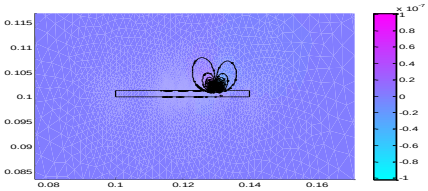
Fig 2. magnetic vector potential A

Figure 3 represents the resistance variation when moving the sensor over a distance of 12mm.

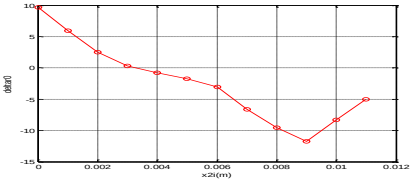
Fig 3. Variation of resistance according to the movement of sensor.

Concerning the figure 4, the variation of one of the stochastic solutions of impedance is represented by Z_0 on a displacement of 14mm. the standard deviation being 100% which results in zero electrical conductivity.

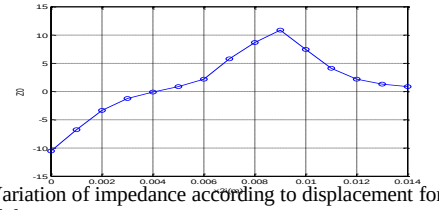
Fig 4. Variation of impedance according to displacement for a defect 100% standard deviation.

Figure 5 illustrates the evolution of the impedance resulting from the stochastic calculation, according to its argument and the displacement for two standard deviations 10% and 90%.

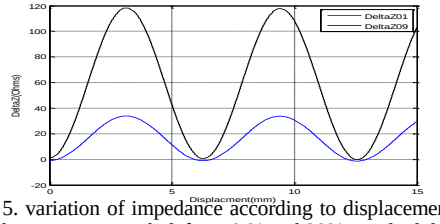

Fig 5. variation of impedance according to displacement and argument theta with comparison with defect 10 % and 90% standard deviation

IV. Conclusion

The inspection and characterization of composite materials being current, the relevance of proposing an approach for the detection of defects has led us to develop a SFEM calculation code under Matlab environment. This approach allows us to distribute the electrical conductivity in the suspected area. The latter is composed of the coefficients calculated from the stochastic polynomial chaos. The calculation code makes it possible to obtain three solutions for a rank equal to two. We started the detection of the defect with one of the solutions in term of magnetic vector potential, using the formulation of the energy, we evaluated the variation of the impedance in the suspected zone. The results obtained allow us to conclude that when the standard deviation is large, the electrical conductivity decreases, which is manifested by a large variation in the impedance, which characterizes the presence of a defect due to lack of material in comparison to a flawless specimen. The stochastic model is a new approach which makes it possible to process the problem and move on to post-processing without requiring an inverse problem. The variation of the electrical conductivity taken as random variable on the stratified materials shows us that in the zone of defect, the impedance is important. The stochastic finite element model tells us about the probability of default when using the correct input variable settings.

References

[1] Z.Wang, Y.Ma, B.Yuan, C.Wu, C.Li, S.Sun, "Development of laser processing carbon-fiber-reinforced plastic," Sensors,23,3659. https://doi.org/10.3390/s23073659, 2023.

[2] J. Cheng, J. Qiu, X. Xu, H. Ji, T.Takagi, T.Uchimoto, "Research advances in eddy current testing for maintenance of carbon fiber reinforced plastic composites" International journal of applied electromagnetics and mechanics 51 261-284 doi 10.3233/JAE-150168 IOS Press, 2016.

[3] S. Sharma, P. Sudhakara, S. Nijjar, S. Saini, G. Singh, "Recent progress of composite materials in vrious novel engineering applications," ScienceDirect 2217-7853 Elsevier, 2018.

[4] H.D.Wagner, L.W. Steenbakkers, "Microdamage analysis of fibrous composite monolayers under tensile stress," journal of materials science 21 3956-3975 1989.

[5] J. Wen, Y. Zeng, C. Wu, Dr. J. Guan, Prof. H. Guo, "Silk Lattice Structures from Unidirectional Silk Fiber– Reinforced Composites for Breaking Energy Absorption" DOI: 10.1002/adem.201900921 FULL PAPER www.aem-journal.com Adv. Eng. Mater, 22, 190092 2020.

[6] J.Galos "Thin-ply composite laminates: a review," School of Engineering, https://doi.org/10.1016/j.compstruct.2020.111920 January 2020 0263-8223/ Elsevier 2020.

[7] A.E. Pasto, D.N. Braski, T.R. Watkins, W.D. Porter, D.N. Braski, T.R. Watkins, W.D. Porter, E. Lara-Curzio, S.B. McSpadden, "Characterization techniques for composites and other advanced materials, " 1359-8368/99/$ - see front matter Elsevier Science Ltd PII: S1359-8368(99)00040-2 1999.

[8] N.Tao A.G. Anisimov, R.M. Goves, "Shearography non-destructive testing of thick GFRP laminates : numerical and experimental study on defect detection with thermal loading," https://doi.org/10.1016/j.compstruct.2021.115008 0263-8223/ Elsevier 2021.

[9] S. Kumar, D. Mahto, "Recent trend in industrial and other engineering application of non-detructive testing: a review", international journal of science & engineering research, volume 4, issue 9 ISSN 2229-5518 2013.

[10] G. Mook, R. Lange, O. Koeser, "Non-destructive characterization of carbon-fibre-reinforced plastics by means of eddy currents," *Composites Science and Technology* 61, 865–873 2001.

[11] G .Wasselynck, D.Trichet, J.Fouladgar, "Determination of the Electrical Conductivity Tensor of a CFRP Composite Using a 3-D Percolation Model, " IEEE Transaction on magnetics, vol. 49, N^{O}. 5, May 2013.

[12] Q. Zhao, K. Zhang, S. Zhu , H. Xu, D.Cao, L. Zhao, R. Zhang, W. Yin, "Review on the Electrical Resistance/Conductivity of Carbon Fiber Reinforced Polymer, " Applied Sciences 9,2390; doi 10.3390/app9112390 2019.

[13] Z. Oudni, M. Féliachi, and H. Mohellebi, "Assessment of the probability of failure for EC nondestructive testing based on intrusive spectral stochastic finite element method," Eur. Phys. J. Appl. Phys., vol. 66, no. 3, p. 30904, June 2014.

Contribution to Characterisation of Unidirectional Carbon Fiber Reinforced Plastic (CFRP) Using High-Frequency Eddy Current Profiling Device Technology

Amirouche HAROUZ[1,*] , Mohammed El Hadi LATRECHE[2], Henning HEUER[3,4], Hassene MOHELLEBI[1].
[1] Faculty of Electrical Engineering and Computer Science, Mouloud MAMMERI University of Tiz-Ouzou, Tizi-Ouzou, Algeria.
[2]Brother MENTOURI University - Constantine 1, Constantine, Algeria.
[3] Fraunhofer Institute for Ceramic Technology and Systems, Material Diagnostic, Dresden, Germany.
[4] TU Dresden, Chair Sensor Systems for Non-Destructive Testing, Dresden, Germany.
[*]E-mail: harouzamirouche@gmail.com

***Abstract*—This paper explores the use of high-frequency eddy currents (EddyCus®) for non-destructive testing of CFRP. Unlike traditional methods, EddyCus® employs frequencies up to 100 MHz to analyze probe impedance changes, revealing properties like permittivity, permeability, resistivity, and conductivity. The method involves scanning CFRP samples with the EddyCus® MPECS system at various frequencies, with the MPECS software generating impedance data profiles for analysis.**

Keywords—CFRP, High-frequency eddy current, Non-destructive characterization, EddyCus®MPECS.

I. INTRODUCTION

Eddy current testing (ECT) is widely used for inspecting electrically conductive materials in engineering [1]. This non-destructive testing (NDT) method is based on electromagnetism theory, analyzing changes in the electromagnetic properties of the tested conductor to detect properties and defects. Generally, ECT uses kHz range AC current for high-electrical conductive materials, but MHz range AC current is used for low-electrical conductive materials like carbon fiber reinforced plastics (CFRP) [2]. ECT technology, a critical tool for composite defect detection, has rapidly developed from advanced NDT. An alternating current in a coil creates a magnetic field, inducing eddy currents in nearby conductors, which generate a secondary magnetic field that opposes the first. Material changes, such as cracks, disrupt these currents and alter the secondary field, detectable by measuring the coil's impedance [3, 5]. When a current of a certain frequency flows into the excitation coil, electromagnetic induction generates eddy currents in the CFRP, which create a magnetic field and affect the coil's voltage and current [8].

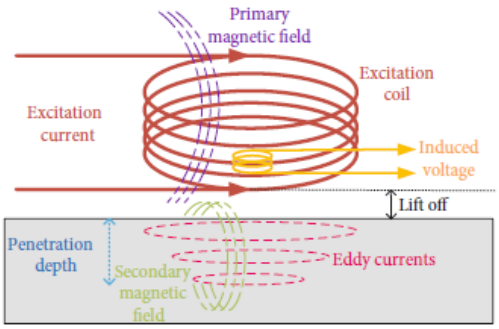

Fig. 1. Schematic diagram of probe and specimen configuration for eddy current testing.

ECT assesses conductivity or permeability using electromagnetism. Higher frequencies (up to 100 MHz) enable probing of less conductive materials, as offered by the "EddyCus®" system [3]. Figure 1 illustrates the fundamental principles of electromagnetic non-destructive testing [5].

II. THEORICAL BACKGROUN

A. Electrical propreties of CFRP

The electrical properties of single-layer, unidirectional carbon fiber materials (CFRP) depend on several factors and exhibit strong anisotropy (direction dependence) [3, 7]:

-Conductivity: longitudinal conductivity can each up to $5*10^6$ S/m, while the lateral conductivity is significantly lower at around $1*10^3$ S/m. These values can vary based on fiber type, orientation, stacking sequence, fiber volume content, density, and compaction around the fibers.

-Permittivity: this property is essential for radio frequency (RF) testing, affecting both the measurement signal and eddy currents. In dry carbon, permittivity is primarily influenced by the fiber coating and surrounding air. However, when CFRP is formed, the air is replaced by a polymer resin, resulting in permittivity dependence on the resin type and processing quality.

The main electrical effects of an alternating magnetic field on CFRP. Three key parameters influence these effects [8]:

1. Fiber Volume Ratio:

This ratio directly affects the average electrical conductivity due to the varying amount of conductive fibers within a specific volume. This value is essential for setting appropriate measurement parameters like frequency and penetration depth.

2. Electrical Connections between Fiber Bundles:

The structure (woven, crimped, etc.), interface chemistry, and consolidation density (achieved through pressing) influence the electrical contact between neighbouring fiber bundles. Even identical materials can display different eddy current propagation due to variations in internal electrical connections. Horizontal electrical connections (in-plane, parallel to the surface) directly impact the contrast in the RF image. Vertical connections (through the depth) affect the interlaminar interfaces and, consequently, the penetration depth.

*3. Capacitive Effect and Displacement Current***:**

Besides the electrical connections, the dielectric properties of the matrix material also influence the complex signal impedance.

B. High-Frequency EddyCus Testing in the frequency range of Radio Waves

The EddyCus® MPECS system uses eddy currents to assess the conductivity of carbon fiber materials (RCF, NCF, CFRP) for quality control. Despite their low conductivity, eddy currents can be induced in the fibers. The

system's high-resolution sensors scan at four frequencies, detecting and separating defects across multiple layers. By processing scanned images, the system can identify flaws such as missing fibers, misaligned threads, and material inconsistencies (Figure 2).

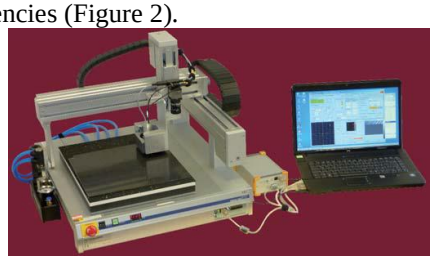

Fig. 2. EddyCus® Multi Parameters Eddy Current Scanner (MPECS).

By the High-Frequency Eddy Current (HFEC) based Impedance the penetration depth is derived as follows [2, 6, 7]:

$$\delta = \sqrt{\frac{2}{\omega\mu\sigma}} \quad (1)$$

where ω is the angular frequency $2\pi f$, μ is the permeability and σ is the electrical conductivity.

The induced voltage is:

$$U_{ind} = -\frac{d\phi}{dt} \quad (2)$$

where $\frac{d\phi}{dt}$ is the rate of change of magnetic flux.

Equation (1) indicates that increasing the frequency reduces the penetration depth, while Equation (2) demonstrates that higher frequencies amplify the signal amplitude. Therefore, lower conductivity or thickness of the specimen necessitates higher frequencies for enhanced sensitivity [6].

III. Experiment, Results and Discussion

The principle involves using the EddyCus MPECS for profiling by applying a frequency train to the sample, with the sensor remaining stationary. The frequency train consists of 255 frequency values (in MHz) represented on the x-axis of the plots (0:254, each point representing a frequency). We analyze the electromagnetic behavior of each sample based on dimension and filling rate. The MPECS software provides impedance (Z) values for each scan. Profiling was conducted on eight samples produced at Fraunhofer IKTS in Dresden, with dimensions of 10mm x 20mm x 2mm and varying fiber volume ratios (20%, 40%, 60%, and 80%).

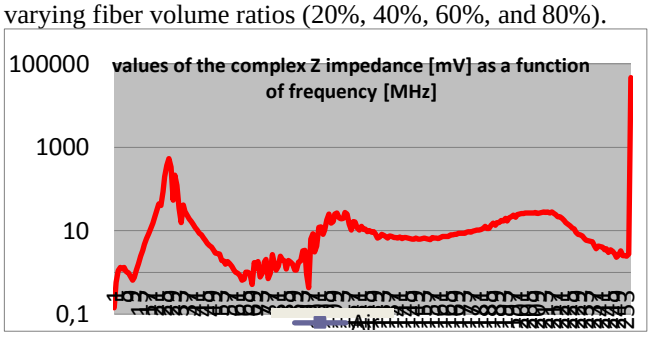

Fig. 3. Plot of the impedance at each frequency train point.

Figures 3 and 4 shows the impedance plots for samples with dimensions 20mm x 20mm x 2mm and filling rates of 40% and 80%, respectively. The change in complex impedance with sensor frequency variation in profiling mode reveals information about the permittivity, resistivity, permeability, and conductivity of the samples. Higher frequencies result in current concentrating on the material's surface due to the skin effect, influencing the density and distribution of induced eddy currents.

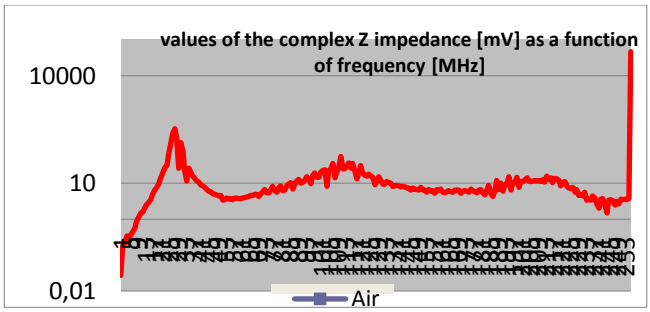

Fig. 4. Plot of the impedance at each frequency train point.

This affects the magnetic field and the measured electrical impedance. At lower frequencies (0.05MHz to 20MHz), where current penetrates deeper, variations in conductivity or permittivity at greater depths significantly impact the measured impedance. At higher frequencies (20MHz to 100MHz), where current is surface-concentrated, surface variations in conductivity or permittivity greatly affect the impedance. An increase in surface conductivity decreases impedance, while a decrease increases it. Permittivity variations affect the electric field distribution near the surface, but its impact on impedance is less pronounced than conductivity changes in an eddy current test.

IV. Conclusion

In an eddy current test of a carbon fiber reinforced polymer (CFRP) matrix composite, varying the frequency affects the measured electrical impedance by altering the current penetration depth into the material. This change influences the distribution of the induced magnetic field and, consequently, the electrical impedance measured by the sensor. Variations in the electrical conductivity or permittivity on the CFRP surface can also modify the distribution of the eddy current-induced electromagnetic field, impacting the measured impedance.

References

[1] Wataru Matsunaga, Yoshihiro Mizutani and Akira Todoroki, "Defect Detection in GFRP Plates Using Electromagnetic Induction Testing Using Autoencoder", Presented at 1st International Electronic Conference on Applied Sciences, 10–30 November 2020.

[2] M. Schulze et al., "Textural analyses of carbon fiber materials by 2D-FFT of complex images obtained by high frequency Eddy current imaging (HF-ECI)", Nondestructive Characterization for composite materials, Aerospace Engineering, Civil infrastructure, and Homeland Security, SPIE Proceedings Vol. 8347, 2012.

[3] Iryna Pastora et al.,"High-Frequency Eddy Current Based Impedance Spectroscopy for Characterization of the Percolation Process of Wet Conductive Coatings", 41st Annual Review of Progress in Quantitative Nondestructive Evaluation AIP Conf. Proc. 1650, 414-423; doi: 10.1063/1.4914637, 2015.

[4] W. Deng, J. Bao, S. Luo, and X. Xiong, "Simulation Analysis of Eddy Current Testing Parameters for Surface and Subsurface Defect Detection of Aviation Aluminum Alloy Plate," Mar. 2022, doi: 10.1155/2022/8111998.

[5] Shu-an Ji , Wei-liang Jin, Ying Jin, Zheng Lin, Sen Wang,1 and Qing Li, "Real-Time Strain Detection Technology for Steel Structures Based on Eddy Current Effect", Hindawi, Journal of Sensors, Volume 2023, Article ID 7491593, 9 pages.

[6] Gaebler S, Heuer H, Heinrich G. "Measuring and imaging permittivity of Insulators using high-frequency eddy current devices, Instrumentation and measurement". IEEE Transactions 2015.

[7] H. Heuer et al., "Non destructive evaluation (NDE) ofcomposites : Eddy current techniques ", pp. 33-35.1. 2013.

[8] Cheng J, Ji H, Qiu J, Takagi T, Uchimoto T, Hu N. "Role of interlaminar interface on bulk conductivity and electrical anisotropy of CFRP laminates measured by eddy current method". NDT&E Int 2014.

Capteur gravimétrique à ondes acoustiques de surface (SAW)

SAIT Smail [1, 2]

[1] *Equipe ondes est acoustique, Laboratoire de Physique des Matériaux, USTHB, BP32 El Alia, 16111, Alger, Algérie*

[2]*Faculté des Sciences, département de physique, UMMTO, BP 17RP, Algérie*

smail.sait@ummto.dz

Résumé. **Le monde industriel cherche de plus en plus les moyens lui permettant de miniaturiser, en affinant leurs capacités, différents systèmes de contrôle et en particulier des capteurs de toutes sortes. La miniaturisation de capteurs basés sur l'exploitation des ondes acoustiques guidées est très recherchée et appréciée pour son efficacité et son innocuité. Les ondes principales pouvant être guidées dans un matériau piézoélectrique ou non piézoélectrique, sont des ondes de différentes natures sollicitant la matière de différentes façons pour vibrer, selon la fréquence à laquelle on les excite.**

L'intérêt des ondes guidées de Love, réside dans le confinement de leur énergie près des surfaces libres du guide d'onde, donc de leur grande sensibilité aux variations du milieu extérieur. Les dispositifs MEMS (Microelectromechanical systems) à base d'ondes de Love sont théoriquement étudiés dans leur rôle potentiel en tant que plate-forme technologique prometteuse pour le développement de capteurs, basés sur la propagation des ondes acoustiques, pour les environnements liquides.

Ce travail, met en évidence l'intérêt d'utiliser des matériaux piézoélectriques comme guides d'ondes pour optimiser la sensibilité d'un capteur à ondes de Love dédié à la mesure de la viscosité d'un liquide Newtonien, en exploitant le mode fondamental de Love L_0

Mots-clés— Piézoélectricité, capteurs, ondes, atténuation, viscosité.

I. INTRODUCTION

Les dispositifs MEMS (Microelectromechanical systems) à base d'ondes de Love ont une grande sensibilité aux variations du milieu extérieur, ils se composent d'un substrat semi-infini piézoélectrique et d'une couche mince. L'onde générée dans le substrat peut être couplée à la couche, à la condition que la vitesse de l'onde de volume transversale dans la couche soit inférieure à celle dans le substrat. L'onde est alors guidée dans la couche (couche guidante), son énergie est principalement répartie dans celle-ci. La sensibilité gravimétrique des capteurs à onde de Love dépend des propriétés des deux matériaux (le substrat semi infini et la couche). La coupe cristallographique (angles d'Euler) et l'épaisseur de la couche [1], sont deux propriétés qui jouent un rôle important dans l'optimisation de la sensibilité à l'effet de masse dans le but de mesurer la viscosité [2].

II. GENERATION DES ONDES DE LOVE

La génération d'ondes de Love s'effectue sur une couche guidante déposée sur un substrat à l'aide de transducteur interdigités. Un transducteur interdigité dans sa version la plus simple est formé de deux peignes identiques et symétriques qui jouent le rôle d'électrodes métalliques (figure 1), l'application d'une tension sinusoïdale aux bornes d'un transducteur interdigité, crée un champ électrique et engendre par effet piézoélectrique inverse une déformation mécanique qui produit des ondes acoustiques de surface. Ces ondes se propagent dans la couche jusqu'au transducteur interdigité récepteur qui convertira la déformation mécanique du guide en courant électrique. La longueur d'onde de l'onde acoustique est imposée par l'écartement des transducteurs ou par la période géométrique des transducteurs.

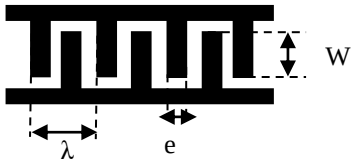

Figure. 1 Transducteur interdigité

L'ouverture W correspond à la distance sur laquelle les doigts des deux électrodes s'interpénètrent. La longueur d'onde λ est égale à la somme de deux largeurs de doigts (e) et de deux distances inter-doigts.

La génération de L'onde de Love exige quelques propriétés physiques sur la couche et le substrat en particulier concernant les vitesses de propagation des ondes transversales dans ces matériaux. La grande différence entre les vitesses entraîne une meilleure sensibilité du système.

III. CAPTEUR A ONDE DE LOVE

Les capteurs à ondes de Love sont constitués d'un substrat, d'une couche guidante et de transducteurs interdigités (figure 2), l'énergie acoustique transportée par l'onde de Love n'est plus répartie dans le volume du substrat comme dans les capteurs à ondes acoustiques de volume mais concentrée en surface, généralement, dans une épaisseur inférieure à la longueur d'onde. Cette particularité les rend beaucoup plus sensibles aux perturbations de surface [1,2].

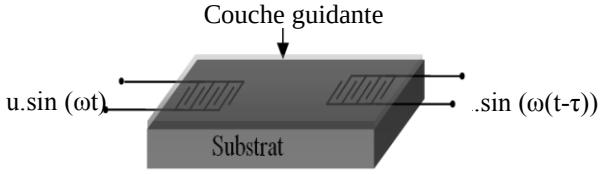

Figure. 2 Schéma d'un dispositif à ondes de Love.

IV. SENSIBILITE GRAVIMETRIQUE

La sensibilité gravimétrique S_m^V (kg.m-2) du capteur à ondes de love est définie comme étant le rapport de la variation relative de vitesse de phase et de la masse surfacique sur la

couche $S_m^V = \frac{\Delta V}{V_{Love}^{air}} \frac{1}{\rho_L \delta}$ avec $\Delta V = V_{Love}^{air} - V_{Love}^{Liquide}$, V_{Love}^{air} est la vitesse de phase du mode de Love sans effet de masse (avant la perturbation, plaque dans l'air) et $V_{Love}^{Liquide}$ la vitesse de phase du mode de Love avec effet de masse (avec la charge du liquide), théoriquement, elle est estimée en calculant le changement de vitesse que les modes subissent lorsque la surface libre de la couche est chargée d'une masse $m_L = \rho_L \delta$ (ρ_L et δ : la densité de masse du liquide ajouté et la profondeur de pénétration de l'onde dans le liquide visqueux), selon l'équation de dispersion.

Cette sensibilité ne reflète pas les véritables performances des capteurs à onde de Love dans les milieux liquide ; la sensibilité du capteur aux propriétés physiques du liquide peut alors être définie comme étant :

$S_\eta^f = \frac{V_{gr}}{V_{ph}} S_m^v \Rightarrow S_\eta^f = \frac{V_{gr}}{V_{ph}} \frac{\Delta V / V_{Love}^{air}}{\rho_L \delta}$ Avec ρ_L [kg.m−3] la masse volumique du liquide et η [Pa.s] sa viscosité en régime newtonien [1-4]

V. Simulation

Deux simulations ont été réalisées pour différents matériaux afin d'apprécier leur sensibilité pour une longueur d'onde λ fixée à 50 µm. L'une concerne l'étude de la variation de la sensibilité en fonction de la combinaison des différents matériaux (couche / substrat) (Fig. 3); et l'autre, concerne l'étude de la variation de la sensibilité en fonction de la longueur d'onde figure 4.

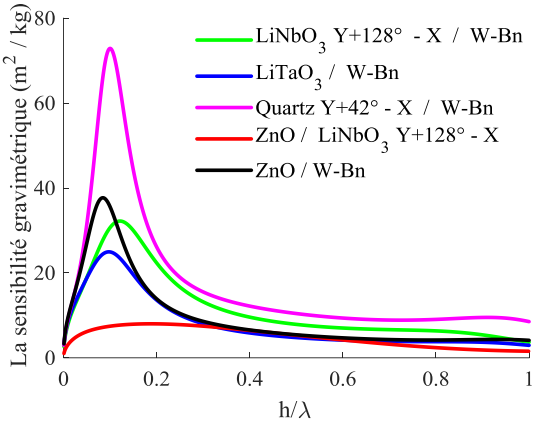

Figure. 3 Courbes des sensibilités gravimétriques pour les différentes combinaisons.

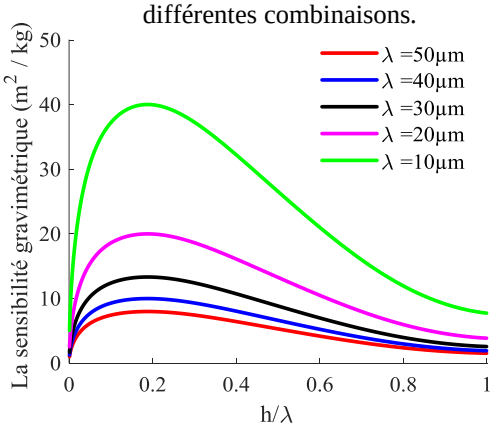

Figure. 4 Evolution de la sensibilité gravimétrique en fonction de la longueur d'onde pour couche ZnO déposée sur le substrat $LiNbO_3$ Y+128°-X.

Les résultats obtenus montrent l'évolution de la sensibilité à l'effet de masse des capteurs en fonction des différentes combinaisons de matériaux pouvant être employés dans les dispositifs à ondes de Love (figure 3). Ces combinaisons (couche/substrat) atteignent toutes un maximum de sensibilité plus ou moins important selon la valeur de h/λ. Cependant, on remarque qu'une meilleure sensibilité est atteinte (72.8 Kg m-2) pour un rapport h/λ = 0.1 dans le cas où le dispositif à onde de Love se compose d'une couche de quartz Y+42°-X et d'un substrat le W-Bn, d'autre part un minimum de sensibilité qui vaut 8.003 Kg m^{-2} est obtenu dans le cas d'une composition ZnO / LiNbO3 Y+128°-X qui correspond à h/λ = 0.187 (figure 4). Le tableau ci-dessous récapitule les différents résultats obtenus en fonction du rapport h/λ, de l'épaisseur de la couche h et de la fréquence de fonctionnement.

Tableau. 1: Tableau récapitulatif des résultats

Couche/substrat	Sensibilité (Kg m^{-2})	h/λ	h (µm)	f(MHz)
Quartz Y+42°-X / W-Bn	72.88	0.100	5	148.14
ZnO / W-Bn	37.70	0.084	4.2	153.04
$LiNbO_3$Y+128°-X / W-Bn	32.21	0.122	6.1	152.70
LiTaO3 /W-Bn	24.96	0.100	5	153.16
ZnO / $LiNbO_3$ Y+128°-X	8.003	0.193	9.4	69.2

On consuls, qu'il est. possible d'avoir une meilleur sensibilité à l'effet de masse dans le cas de ZnO / $LiNbO_3$ Y+128°-X, en jouant sur l'épaisseur de la couche on remarque qu'elle attient 40.02 Kg m^{-2} pour le même rapport h/λ = 0.193 (figure 4), on constate qu'elle augmente de 5% pour une diminution de 5 % de la longueur d'onde

VI. Conclusion

Les simulations montrent la sensibilité gravimétrique des capteurs à ondes de Love, pour différentes combinaisons couches/substrats, dans le but d'optimiser leur sensibilité à l'effet de masse pour la mesure de la viscosité. Il en ressort qu'il est possible d'avoir une meilleure sensibilité à l'effet de masse, en jouant sur l'épaisseur de la couche guidante. Par ailleurs, on remarquera qu'il est possible d'utiliser d'autres combinaisons (de faible sensibilité) pour optimiser un capteur à onde de Love, en faisant varier la longueur d'onde, ce qui a pour effet de diminuer de l'épaisseur de la couche guidante

References

[1] B. A. Auld, Acoustic fields and waves in solids I, John Wiley & Sons, Inc, (1973)

[2] D. Royer, E. Dieulesaint, Elastic waves in solids I, Free and guided propagation, Springer, France, (1996).

[3] G. Kovacs, A. Venema, Theoretical comparison of sensitivities of acoustic shear wave modes for (bio) chemical sensing in liquids, Appl. Phys. Lett, 61, pp639–641,1992.

[4] C. Caliendo, S. Sait, F. Boubenider, Love mode MEMS devices for sensing applications in liquids, Micromachines, 7, 15, 2016.

Numerical modeling of micromagnetic methods in 3MA linear and non-linear eddy current methods

Yasmine Gabi
Fraunhofer-Institute for Nondestructive Testing (IZFP), Campus E3 1, 66123 Saarbrücken, Germany
yasmine.gabi@izfp.fraunhofer.de
ORCID: 0000-0002-6148-4008

Klaus Szielasko
Fraunhofer-Institute for Nondestructive Testing (IZFP), Campus E3 1, 66123 Saarbrücken, Germany
klaus.szielasko@izfp.fraunhofer.de

***Abstract*—**The paper deals about the simulation of linear and non-linear eddy current (EC) techniques in the commercial 3MA NDT systems. Robust numerical computations are established to investigate the properties of bilayer specimens. In linear and non-linear EC, the quasi-static magnetic behaviour is described via the Jiles-Atherton hysteresis model. Magnetic dynamic phenomena are taken into account applying the Bertotti formula. Based on electromagnetic meso-macroscopic behaviour, the experimental signals are reproduced accurately. The analytical model will be assessed in the linear as well as the non-linear case by comparison to experimental signals.

Keywords—ferromagnetic material, multilayer material properties, finite elements, dynamic behavior.

I. INTRODUCTION

The design and construction of specialized Non-Destructive Evaluation (NDE) equipment, e.g. for in-process monitoring, remains crucial for the quality control in European industry. It may be supported via robust calculation tools, in order to optimize the inspection situation to determine the requested measuring targets such as coating thickness, hardness, residual stress, etc. The emerging use of numerical simulation is a major trend in the field with tremendous potential benefits in terms of costs reduction, enhanced diagnosis reliability and consequently increased competitiveness. The simulation of 3MA electromagnetic methods attracted the attention of many experts [1-2]. Some of them worked in development on complete robust physical based models in order to simulate the several 3MA magnetic methods like harmonic analysis and incremental permeability (IP) [3]. These models rely on parametric descriptions of some fundamental electromagnetic properties of different specimen layers, e.g. electrical conductivity and parameters, describing the magnetization, like saturation polarization or initial magnetic permeability or most favourable the complete parameterised B/H hysteresis loop. In 2012, an analytical calculation of eddy current 3MA method was investigated in framework of ANR DPSMMOD project [4]. The purpose was to describe the magnetic signature of 3MA eddy current and incremental permeability (see Fig. 1). In this project, Gabi et al. have developed an analytical model for conventional eddy current investigation.

II. ANALYTICAL EDDY CURRENT MODEL

The model targets a qualitative goal based on simplified aspects, considering a finite sized ferromagnetic samples and the a cylindrical detection coil. Furthermore, it is supposed that a global demagnetizing coefficient influences the amplitude of the field in the different layers of the sample in an isotropic way. Considering these strong simplifications, the problem becomes unidirectional.

Figure 1: 3MA system applied to a lab sample

The geometry configuration consists of two coils placed over the specimen (Fig. 2).

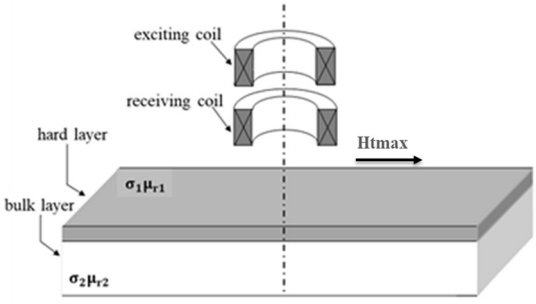

Figure 2: Inspection situation

The first one is the transmitting eddy current coil of 100 turns and 3 mm in diameter. It is excited by a sinusoidal low-amplitude current of about 3 mA and a selected frequency of 60 kHz. The specimen is described as a multi-layer area, in the surface a hard-magnetic zone and soft area in the bulk.

The second coil is indicated as a search coil, which has 300 turns. Coherent demodulation is applied in order to obtain the real and imaginary part of the voltage. Besides this, it is considered that a low-frequency magnetic field is present,

which is homogeneous in the small sample investigation area. The amplitude of this field is quite high, where operating point is around coercive field and the magnetization frequency is around 200 Hz.

Firstly, the calculation is focused only on the EC – linear method. The geometry of the flux lines flowing through the eddy current detection coil is, in fact, very complex to describe. In [4], it is developed an analytical physics-based model for the conventional eddy current method. The development leads to the following equations 1, 2 for the magnetic induction B in both sample zones. Both parameters β1 and β2 are parameters to be defined. The calculation are described in details in [4]

In zone 1

$$\langle B_1 \rangle = \beta_1 \frac{2\delta_1}{(1+i)c} sh\left[\frac{1}{2}(1+i)\frac{c}{\delta_1}\right]\exp(i\omega t) \quad (1)$$

In zone 2

$$\langle B_2 \rangle = \beta_2 \frac{\delta_2 \exp(i\omega t)}{(1+i)d}\left\{sh\left[\frac{(1+i)}{\delta_2}\left(d+\frac{c}{2}\right)\right] - sh\left[\frac{1}{2}(1+i)\frac{c}{\delta_2}\right]\right\} \quad (2)$$

C, d represent respectively the total sample thickness and surface layer thickness.

The skin depth is defined as following:

$$\delta_k = \frac{1}{\sqrt{\mu_0 \mu_{rk} \sigma_k \pi f}} \quad (3)$$

The value of the permeability μ_{rk} depends on the EC signal excitation type (linear and non-linear).

It is known that in conventional linear EC techniques, the excitation is performed in linear Rayleigh area, where the value of permeability is equal to initial permeability. Fig. 3 compares simulation results (FEM code and analytical calculation) to experimental data for the imaginary part of the voltage in case of EC linear (f_{ec} = 50 kHz) excitation for inspection situation of hardening depth. A high correlation between simulation results and measurement is observed.

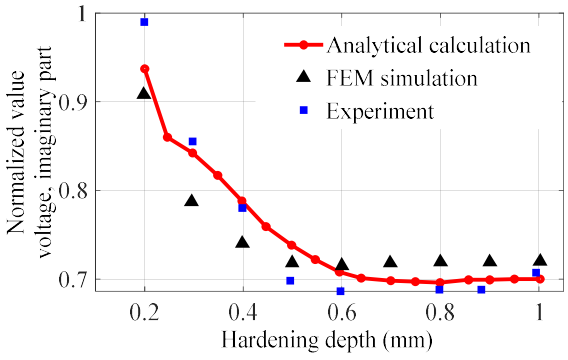

Figure 3: Validation with experimental signals

In case of the non-linear EC method, the μ_{rk} has a non-linear profile due to the intrinsic hysteresis properties. It was proven in [5], that μ_{rk} is an anisotropic tensor which depends on magnetization direction. Furthermore, is linked to the differential permeability. The simulation was performed at f_{ec} = 50 kHz, a low-frequency tangential field strength amplitude of H_{tmax} = 50 A/cm and a magnetization frequency of f = 200 Hz.

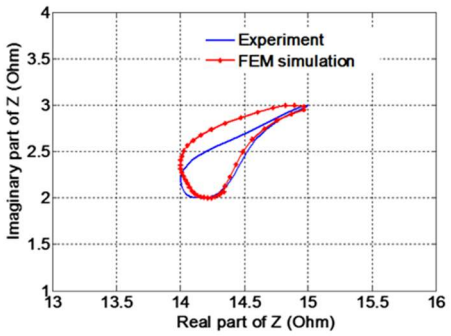

Figure 4: Non-linear eddy current validation

The analytical model is able to reproduce the measured signals of non-linear eddy current technique in 3MA technology with quite good accuracy. The mean deviation between both signals is less than 25 %.

III. CONCLUSION

In this work, the EC analytical model is extended to take into account the non-linear aspect of ferromagnetic material at higher magnetization level by integration of incremental permeability calculated via Jiles-Atherton hysteresis model. Besides this, the dynamic phenomena are described using the Bertotti formula. The assessment of the 3MA linear and non-linear EC (IP) is performed by comparison of computed data and experimental signals.

In future work, the multi-layer approach will be analyzed and validated in case of the non-linear eddy current technique, where the impact of surface layers will be studied.

IV. REFERENCES

[1] G. Dobmann, "Physical Basics and Industrial Applications of 3MA - Micromagnetic Multiparameter Microstructure and Stress Analysis", European Federation for Nondestructive Testing (EFNDT), European Conference on Nondestructive Testing (10): ECNDT. 2010, Vortrag 1.1.1.

[2] B. Wolter, C. Boller, C. Conrad, H.G. Herrmann, R. Kern, H. Kopp. Future trends in steel development, processing technologies and applications: bringing the automotive, supplier and steel industries together. Düsseldorf, (2014) 698-705.

[3] C. Conrad, R. Kern, 3rd General Motors PHS Suppliers Forum. Nürnberg: Grundig Akademie, (2015) 224–230.

[4] K. Szielasko, I. Mironenko, I. Altpeter, H.G. Herrmann and C. Boller. Minimalistic Devices and Sensors for Micromagnetic Materials Characterization. IEEE Trans. Magn. 49 (2013) 101-104. doi: 10.1109/TMAG.2012.2217943.

[5] Y. Gabi, A. Kedous-Lebouc, G. Meunier, B. Wolter, O. Geoffroy, P. Meilland, P. Labie, C. Guérin, and O. Martins, in Proc. 19th Conf. Comput. Electromagn. Fields (2013). 48.

Y. Gabi, K. Jacob, B. Wolter, C. Conrad, B. Straß and J. Grimm, Analysis of incremental and differential permeability in NDT via 3D-simulation and experiment. Journal of Magnetism and Magnetic Materials, 505, (2020), 166695.

Session 3 (Orale):

Semi-Analytical and Fast Resolution Methods

- New semi-analytical approach to study the interactions between conventional and superconducting coil
- High Frequency Impedance computation of exciting coil using Coupled Electric Circuits Method
- Elaboration de modèles semi-analytiques pour la récupération d'énergie
- Modeling of Skin/Sensor Contact Impact on EEG Signals Encountered in Neurosciences

New semi-analytical approach to study the interactions between conventional and superconducting coil

Roujaina BOUGANDOURA
Electrical Engineering and Industrial Electronics Laboratory (L2EI)
University of Jijel
Jijel, Algeria
roujaina.bougandoura@univ-jijel.dz

Hocine BOUCHEKHOU
Electrical Engineering and Industrial Electronics Laboratory (L2EI)
University of Jijel
Jijel, Algeria
hbouchekhou@gmail.com

Ibrahim HEDOUACHE
Electrical Engineering and Industrial Electronics Laboratory (L2EI)
University of Jijel
Jijel, Algeria
ibrahim.hedouache@univ-jijel.dz

Hicham ALLAG
Electrical Engineering and Industrial Electronics Laboratory (L2EI)
University of Jijel
Jijel, Algeria
allag_hic@yahoo.fr

***Abstract*—In this paper, we present a study on the interactions between a conventional copper coil, powered with a DC voltage, and a superconducting one. Partial element equivalent circuit (PEEC) method is adapted for the calculation of self and mutual inductance, partial electrical resistance and induced currents distribution in superconducting coil. The power law model is considered in 2D modeling of superconducting material behaviour, and we implement an iterative calculation system for the proposed semi-analytical approach.**

Keywords— Copper coil, superconducting coil, self and mutual inductance, resistance, Partial Element Equivalent Circuit (PEEC) method.

Introduction

Superconducting (SC) materials represent a major advancement in electrical engineering field. With the continuous improvement of cryogenic systems, SC coils have found applications in various fields such as energy storage, wireless energy transfer, induction heating and electric machines, thereby offering exceptional performance and capabilities [1-2]. During operation, these materials are generally exposed to external magnetic fields that will affect strongly the behavior of superconductors. So, it's very interesting to study the behavior and operating limits of these materials before their use in different electromagnetic devices.

In this paper, we develop a semi-analytical approach to calculate the total partial inductances and resistances results of the interaction between an excitation copper (EC) coil and a SC one. 2D Partial element equivalent circuit (PEEC) method is applied in order to obtain a full impedance matrix containing resistances, self-inductances and mutual inductances between each elementary conductor. We propose an iterative system process for calculation of these quantities. In this work, we also calculate the induced currents distribution on SC coil surface.

I. FORMULATION OF THE BASIC PROBLEM

Fig. 1 illustrates the geometry of the problem under consideration. It shows a EC coil placed below a SC one. Both coils have an air core and a rectangular cross-sectional area, and the air gap between them is 4 cm. The studded system is considered as a 2D problem, where the conducting forms are composed of multiple long parallelepipeds represented by juxtaposed rectangular surfaces, as illustrated in fig. 1. Each conductor has its resistance and self-inductance. We denote by M and N the total number subdivisions of SC and EC coil respectively. EC coil is supplied by the voltage (U1-U2).

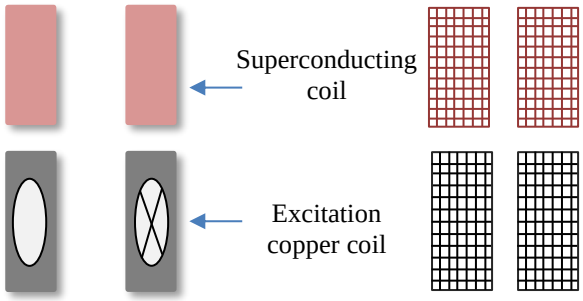

Fig. 1. Geometry and 2D discretization of global studied structure.

II. CALCULATION OF ELECTRICAL PARAMETERS

A. Resistances calculation of the elements EC and SC coil

For EC coil, we assume that the resistivity is constant. Therefore, according to Ohm's law, the resistance expressions of EC and SC coil are written as

$$\boldsymbol{R_{EC} = \rho_c \frac{l}{S}} \tag{1}$$

l is the coil longitudinal length, $\rho_c = 1{,}7.10^{-8}\ \Omega.\mathrm{m}$ is the resistivity of copper and S is the cross-sectional area of EC coil.

$$R_{SC} = \rho_{SC} \frac{l}{S_{SC}} \tag{2}$$

The power law model for SC coil is

$$\rho_{SC} = \left(\frac{E_c}{J_c}\right)\left(\frac{|J|}{J_c}\right)^{n-1} + \rho_0 \tag{3}$$

J is the current density in SC coil, $J_c = 2 \times 10^8\ \mathrm{A/m^2}$ is the critical current density, $E_c = 10^{-6}$ V/m and $\rho_0 = 10^{-16}$ Ω.m critical electric field and initial resistivity value respectively. The n value is considered at 30.

B. *Self and mutual inductances calculation for the elements of EC and SC coil*

The calculation of inductance through Green's functions (U and V), using the geometric mean distance (ln D) for the specific case illustrated in fig. 2, of two parallel rectangles with widths (A, a) and thicknesses (B, b) separated respectively by T and Q, is given by

$$lnD = -\frac{25}{12} + \frac{1}{2(4ab)(4AB)}\sum_{i=0}^{1}\sum_{j=0}^{1}\sum_{k=0}^{1}\sum_{l=0}^{1}(-1)^{i+j+k+l}f(U,V) \quad (4)$$

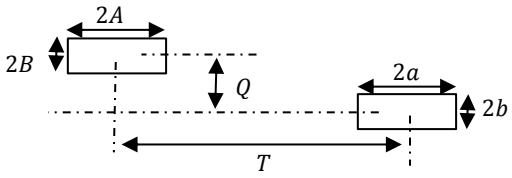

Fig. 2. Geomitrical parameters for inductances calculation.

$$f(U,V) = \left(\frac{U^2V^2}{4} - \frac{U^4}{24} - \frac{V^4}{24}\right) ln(U^2+V^2) + \frac{U^3V}{3} tan^{-1}\left(\frac{V}{U}\right) + \frac{UV^3}{3} tan^{-1}\left(\frac{U}{V}\right) \quad (5)$$

With

$$U = T - (-1)^i a + (-1)^j A \quad (5)$$

$$V = Q - (-1)^k b - (-1)^l B \quad (7)$$

The mutual inductance for the two conductors is given by

$$M_p \cong \frac{\mu_0}{2\pi} l \left(ln\frac{2l}{D} - 1\right) \quad (8)$$

Also, the self-inductance is given as follows

$$L_p \cong \frac{\mu_0}{2\pi} l \left(ln\frac{2L}{a+b} + \frac{1}{2}\right) \quad (9)$$

III. Applications and Results

In this specific application (Fig.1), the EC coil dimensions are (90mmx30mm) outer and inner diameter, 70mm of height and 100mm length. This coil is powered by a voltage ramp function *U=K.t* with *K=300 V/s* and *t* is the considered time. The SC coil dimensions are (90mmx30mm) outer and inner diameter, 25mm of height and 100mm the length.

Fig. 3 shows the distribution of electrical resistances in SC coil. Resistance values vary from 0 to 1.2 ohms in the SC surface. A partial translation of the SC state in these (resistive) regions due to the applied field with EC coil near these surfaces.

Fig. 4 presents the distribution of inductances in SC coil surface. It's observed that the near places to EC coil have a higher inductance value than those that are distant from it.

At the voltage U=12V (0.04s) for a time step 0.002s, we observe a good symmetry of current penetration for both the output and input parts of SC coil, fig. 5. The penetration is stronger in the region that applied magnetic field is important. For these reasons, we observe that the penetration at the bottom of SC coil is stronger than at the top.

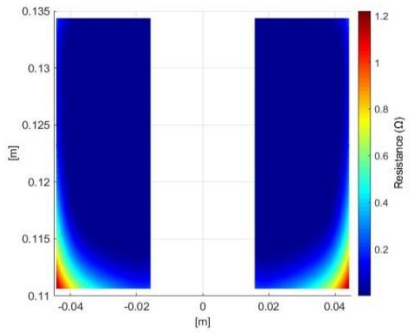

Fig. 3. Electrical resistance in SC coil.

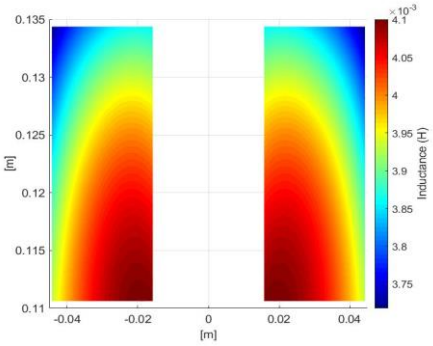

Fig. 4. Distribution of inductances in SC coil.

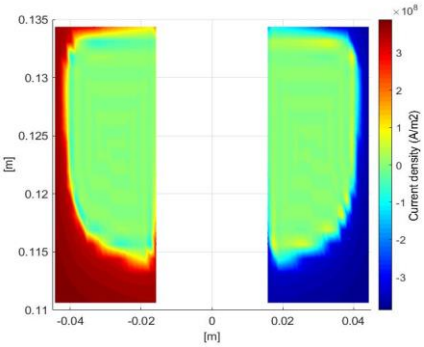

Fig. 5. Penetration of current densities into SC coil surface.

IV. Conclusion

The semi-analytical approach (PEEC) applied in this work has proven its effectiveness in studying the interactions between conventional and SC coils. We have accurately calculated the induced currents, resistances, self and mutual inductances. This method offers a balance between accuracy and computational efficiency, compared with numerical methods, which can require significant calculations.

References

[1] J. Ciceron, A. Badel, P. Tixador, and F. Forest, "Design considerations for high-energy density SMES", IEEE Transaction on applied superconductivity, vol. 27, p. 1-5, June 2017.

[2] R. Inoue, T. Iwamoto, H. Komoda, H. Ueda, and S. Kim, " Basic experimental study on a 1 kW-class WPT system using HTS and copper coils for EVs", IEEE Transaction on applied superconductivity, vol. 34, May 2024.

High frequency impedance computation using coupled electric circuits method

BOUALI Ferroudja
Department of Electrotechnics
Mouloud Mammeri University
Tizi-Ouzou, Algeria
Email: fer.bouali@yahoo.fr
ORCID: 0000-0000-000-0000

MOHELLEBI Hassane
Department of Electrotechnics
Mouloud Mammeri University
Tizi Ouzou, Algeria
Email:hass.2000@yahoo.com
ORCID: 0000-0003-3661-1690

***Abstract*—-This work presents the impedance computation of exciting coil at high frequency by using coupled electric circuits method that uses the mutual inductance's computation approach. The main advantages of the method are that allows the calculation of physical quantities compared to those that exploit an intermediate mathematical unknown as magnetic vector potential. The considered exciting coil is subdivided into thin elementary turns for which the Kirchhoff laws are applicable. The eddy currents are calculated for high frequency power supply the electrical parameters of single and multi-coils are then deduced. The obtained results are compared to existing ones.**

***Index Terms*—Analytical method, coupled circuit method, eddy currents, mutual inductance, three dimensional modeling.**

I. Introduction

The method of coupled electrical circuits is used instead of numerical methods as finite elements; boundary coupled finite elements boundary elements methods. The partial equivalent electric circuits (PEEC) which is dedicated to Cartesian geometries is also used but the coupled electric circuits method has some advantages as precision and calculation time specially in case of 3D computation. The method is applied for the representation of 3D cylindrical structures.

II. Coupled Electrical Circuits Equations

The calculus to express the self-inductance, the resistance of each elementary turn and mutual inductances between turns are given by equations (1), (2) and (3).

$$R_i = \rho_i \frac{\ell_i}{S_i} \tag{1}$$

R_i the resistance of elementary turns i, ρ_i: electrical resistivity, S_i: cross-section of the elementary turn, ℓ_i: length of the elementary coil. The mutual inductance m_{ij} between two elementary turns i and j is given by [1]:

$$m_{ij} = \frac{\mu_0}{4\pi} \int_{s_i} \int_{s_j} \frac{ds_i \cdot ds_j}{\left|\vec{r}_j - \vec{r}_i\right|} \tag{2}$$

The self-inductance is obtained using the expression below:

$$L_{pi} = \mu_0 r_i \left(\ln\left(\frac{8r_i}{D_i}\right) \right) \tag{3}$$

μ_0 : Magnetic permeability of vacuum, r_i and r_j are radii of the elementary turns i and j respectively. ''D_i'' is the width of elementary turn of the copper conductor [2].

Kirchhoff's law allows us to write the corresponding electrical equations (4) and (5) for the elementary turn. L_{ij} is the total inductance, M_{ij} and L_{pi} are mutual and self inductances of elementary turn respectively.

$$U_i = R_i\, I_i + j\omega \sum_{j=1}^{n} L_{ij} I_j \tag{4}$$

$$L_{ij} = M_{ij} + L_{pi} \tag{5}$$

III. Coupled Electrical Circuit Models

A. Coupled electrical circuit discretization

A coupled electrical circuit model is developed from Newmann formula with a non wired turn and a height of (z_{ai} , z_{bi}) and (z_{aj} , z_{bj}) (Fig. 1). The development of a 3D model is proposed by considering the turn of radius r with a variation of the height z and the width r. Figure 1 illustrates the volume taken into account in the development of the proposed 3D model which consider the variation of the physical phenomenon according to the height and the width of turns.

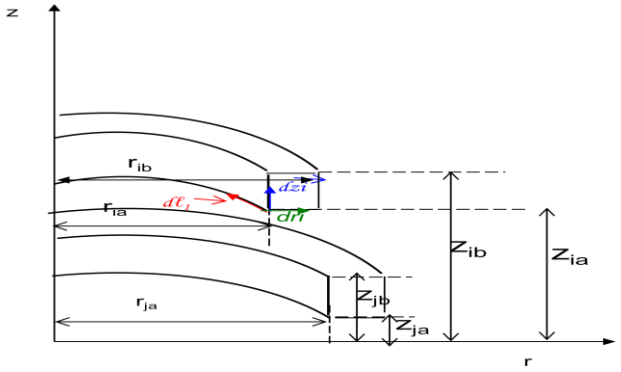

Fig.1. 3D Two circular and coaxial turns representation

The total inductance L_{ij} between ''n'' elementary turns i and j of the conducting ring is obtained using expression (6):

$$L_{ij} = \frac{1}{n^2} \sum_{i=1}^{n} \sum_{\substack{j=1 \\ j \neq i}}^{n} m_{ij} + \frac{1}{n} \sum_{i=1}^{n} L_{p_i} \tag{6}$$

$$m_{ij} = \frac{N_1 N_2}{a_i a_j} \frac{\mu_0}{4\pi} \oint_i \int_{a_i} \oint_j \int_{a_j} \frac{dl_i\, dl_j}{r_{ij}} da_i da_j \tag{7}$$

da_i and da_j elementary surface of elementary coil "i" and "j"

respectively. N_1 and N_2 are the number of elementatry turns of coils. dl_i and dl_j are a portion of the arc of a circle corresponding to the radii r_i and r_j respectively.

B. Impedance computation

The computation of the impedance of the exciting coil is possible by using Kirchhoff laws.
For n subdivisions of a single exciting coil, the equivalent electric circuit is as presented hereafter:

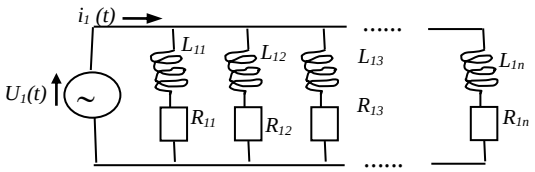

Fig.2. Equivalent electric circuit of single coil

The impedance formula is obtained by using the expression:

$$\frac{1}{Z_{eq}} = \frac{1}{Z_{11}} + \frac{1}{Z_{12}} + \frac{1}{Z_{13}} \ldots\ldots \frac{1}{Z_{1n}}$$

$$Z_{eq} = R_{eq} + j\omega L_{eq}$$

R_{11}, R_{12}, R_{13}, ..., R_{1n} and L_{11}, L_{12}, L_{13} ,..., L_{1n} are resistances. and inductances of elementary coils respectively.
R_{eq}, L_{eq} and Z_{eq} are equivalent resistance, inductance and impedance of the coil.

IV. Applications and Results

The model proposed taking account of the 3D effects is applied for two kinds of arrangements involving two coaxial coils configurations.

A. Application to a multi-turns coil

The application considered concerns a 2D and 3D current distribution in a thick conductor [3].

In Fig. 3 are presented the single and two coils with the considered coupled circuit discretizations in (r, z) plane.

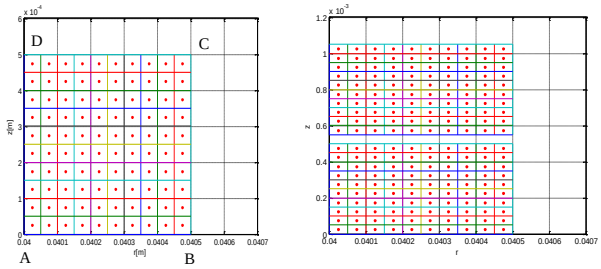

Fig.3. 2D discretization of single and two coils

The geometry characteristics of the first configuration are: inner radius: 40 mm, outer radius: 45 mm, high: 5mm, lift off: 0.5mm [3]. The eddy currents behavior along ABCDA frontier for different configurations is presented in Fig. 5.a and Fig.5.b for 2D and 3D studies respectively. The results given in Fig.5.a (2D) are very close to those given in [3]-[4]. This result is the first quantitative validation of the study. In Fig. 5.b are given the results for simplified 3D model proposed. The difference highlighted in the results obtained between the 2D and 3D models are considered encouraging, presaging support for 3D effects by the proposed 3D model. The experimental achievement would confirm the results.

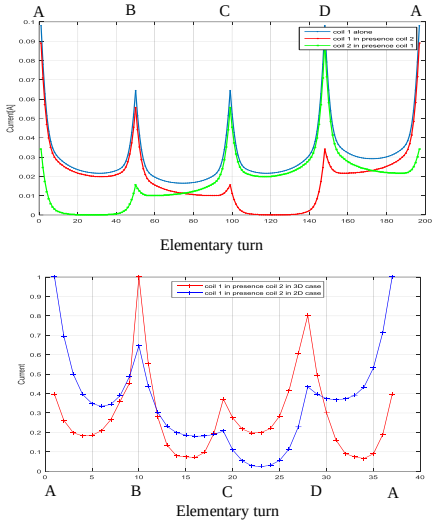

Fig.5. Eddy current computation for 2D and 3D along ABCDA lines

The impedance computation is performed for two configurations. The validation of the developped programm is done by comparing to existing results of configuration 2 which inner and outer radii are 250 mm and 255mm respectively with 5 mm width [3]. In Table I are given the results related to the impedance for several configurations.

TABLE I. EMECTRIC PARAMETERS COMPUTATION

	Single coil (Configuration 2)		Two coils (Configuration 1)	
	Computed	Experimental	2D	3D
R (Ω)	5.6e-3	5.6e-3	1.2e-3	1.3e-3
L (H)	1.32e-6	1.34e-6	0.248e-6	0.2409e-6

V. CONCLUSION

In the present work an analytical 3D model based on the coupled electric circuits approach is applied. The eddy current distribution is computed and a comparison with existing results permits the validation of the 2D study. The developed 3D model shown some capabilities in modeling thick coils and taking acount of proximity effects. The impedance is computed for a single and a two coils. The results for sigle coil are very close to experimental data when the 3D ones seems to be acceptable and experimental validation is needed.

References

[1] M. J. Sablik, R. E.Beissner and A. Choy, ‘’An alternative numerical approach for computing eddy currents: case of the doube-layered plate," IEEE, Transactions on Magnetics, vol. 46, n°9, pp. , 2010

[2] Slobodan Babic, Cevdet Akyel,‘’ New Formulas for Mutual Inductance and Axial Magnetic Force Between Magnetically Coupled Coils: Thick Circular Coil of the Rectangular Cross-Section-Thin Disk Coil(Pancake ’’, IEEE, Transactions on Magnetics, vol. MAG-20, n°3, 1984.

[3] D. Delage, R. Ernst," Prédiction de la répartition des courants dans un inducteur à symétrie de révolution," Revue Générale d'Electricité (RGE), 1984.

[4] B. Maouche, Etude et développement semi-analytique de l'équation de diffusion Electromagnétique avec terme de déplacement dans le cas de dispositifs axisymétriques excités en courant ou en courant, These de Magister, Universite de Bejaia, 1996, Algerie.

Elaboration de modèles semi-analytiques pour la récupération d'énergie

1st Badea Idir
Laboratoire de génie électrique, faculté de technologie,
Université de Bejaia06000, Algérie
badea.idir@univ-bejaia.dz

2nd Bachir Maouche
Laboratoire de génie électrique, faculté de technologie,
Université de Bejaia06000, Algérie
bachir.maouche@univ-bejaia.dz

3nd Sakina Zerguini
Laboratoire de génie électrique, faculté de technologie,
Université de Bejaia 06000, Algérie
sakina.zerguini@univ-bejaia.dz

***Résumé*— Cette contribution présente une modélisation semi-analytique d'un récupérateur d'énergie électromagnétique issu du mouvement d'aimant à l'intérieur d'une bobine. Cette modélisation, du côté électromagnétique, est basée sur la méthode des circuits couplés et est limitée à la récupération de la tension à vide. Les phénomènes électromagnétiques et mécaniques sont alors découplés. Le modèle élaboré est ensuite comparé à celui de l'approximation dipolaire et validé par des résultats déjà publiés.**

***Mots clés :* moment dipolaire, circuits couplés, énergies vibratoires, aimant, bobine.**

I. INTRODUCTION

De nos jours l'alimentation des appareils électroniques portables constitue un enjeu majeur, d'où l'importance de l'exploitation de l'énergie ambiante, l'énergie cinétique sous forme de mouvement ou de vibrations émerge comme une solution prometteuse pour ces appareils, offrant une disponibilité constante et un coût modéré [1,3]. Les récupérateurs électromagnétiques se révèlent particulièrement adaptés grâce au développement des supers aimants.

Cet article propose une étude comparative de modèles de calcul de la tension électromotrice induite par le mouvement sinusoïdal d'un aimant à travers une bobine en mettant en évidence l'efficacité et la complexité du modèle des circuits couplés et la simplicité du modèle issu de l'approximation dipolaires.

II. MODÉLISATIONSELECTRMAGNETIQUES

A. *Principe des circuits électromagnétiques couplés*

Soient deux circuits électriques, p et q circulaire. Le circuit q est une source de champ magnétique et le circuit p est un récepteur de ce champ [4]. Pour décrire les phénomènes présents entre ces deux circuits, les équations de base de Maxwell et la loi de Biot-Savart aboutissent aux deux équations couplées suivantes :

$$\begin{cases} \vec{A}_{pq}(r,z) = \dfrac{\mu_0}{2\pi} G_{pq}(r,z)\vec{I}_q & (a) \\ u_p(r) = 2\pi \dfrac{\vec{r}_p \cdot d\vec{A}_{pq}(r,z)}{dt} & (b) \end{cases} \quad (1)$$

Où $\vec{A}_{pq}$ [T.m] est le potentiel vecteur magnétique généré par le circuit q et reçu par le circuit p. $\vec{I}_q$ [A] est l'intensité de courant source. u_p [V] est la tension à vide du récepteur, $\mu_0=4\pi10^{-7}$ [H/m] est la perméabilité du vide.

G_{pq} représente la réponse du système au point p(r,z) [4]. E_1 et E_2 sont des fonctions elliptiques de Legendredu premier et du deuxième type.r_q et r_p sont les coordonnées radiales respectives de la source et du récepteur. z_q et z_p sont leurs hauteurs respectives,Fig.2.

$$\begin{cases} G_{pq}(r,z) = \sqrt{\dfrac{r_q}{r_p}} \dfrac{(2-k^2)E_1(k) - 2E_2(k)}{k} & (a) \\ k(r,z) = \sqrt{\dfrac{4r_p\, r_q}{(r_p + r_q)^2 + (z_p - z_q)^2}} & (b) \end{cases} \quad (2)$$

Le système étant axisymétrique, le potentiel vecteur magnétique et la densité de courant électrique sont réduits à leurs composantes angulaires.

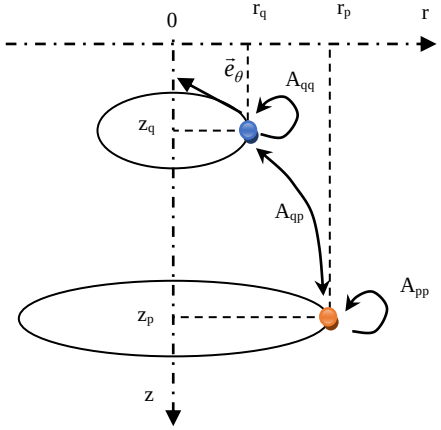

Fig.1. Principe des circuits couplés

B. *Description du récupérateur d'énergie*

Fig. 2 présente la forme du récupérateur, composé d'un aimant de hauteur (h_a) et de rayon moyen (r_a), aligné le long de l'axe z et en déplacement à travers une bobine. Cette bobine est constituée d'un nombre de spires (N), d'une hauteur (h_b) et d'un rayon moyen pour chaque spire (r_b).

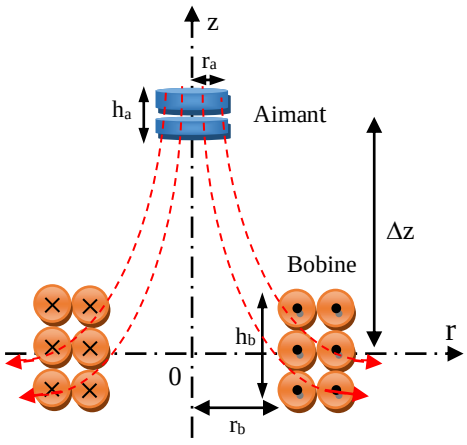

Fig.2. Principe du récupérateur électromagnétique

C. *Modèle des circuits couplés*

L'aimant est représenté par un courant équivalent exprimé à travers le théorème d'Ampère. Pour un aimant de hauteur $h_a$et d'induction magnétique résiduelle B_a, le courant est donné par :

$$I_a = \frac{B_a h_a}{\mu_0} \tag{3}$$

En exploitant le modèle des circuits couplés tel que défini par (1), pour le système aimant-bobine en considérant que le mouvement de l'aimant est axial de vitesse v_z,on parvient à exprimer la tension induite normalisée aux bornes de la bobine à vide comme suit :

$$U_{CCn} = \frac{U}{v_z} = \frac{B_a h_a}{4} \sum_{p=1}^{N} r_p G_{pq}^{Br}(r,z) \tag{4}$$

Où N estle nombre de spires de la bobine.

$$\text{On pose : } G_{pq}^{Br}(r,z) = \frac{dG(r,z)}{dz} \tag{5}$$

Tel que :

$$\left\{ G_{pq}^{Br}(r,z) = \frac{z_p - z_q}{r_p\sqrt{r_p r_q}} \left(\frac{2-k^2}{1-k^2} E_2(k) - 2E_1(k) \right) k \right. \tag{6}$$

D. *Modèle par approximation dipolaire*

Dans cette approche où le rayon de l'aimant est très faible devant la distance où on calcule champ magnétique (r_a<<ρ), (Fig.3),en coordonnées sphériques (ρ,θ,φ), les différentes composantes du champ sont données par [4]:

$$\begin{cases} B_\rho = \dfrac{B_a \tau_a}{2\pi} \dfrac{\cos\varphi}{\rho^3} & (a) \\ B_\varphi = \dfrac{B_a \tau_a}{4\pi} \dfrac{\tau_a \sin\varphi}{\rho^3} & (b) \\ B_r = B_\rho \sin\varphi + B_\varphi \cos\varphi & (c) \end{cases} \tag{7}$$

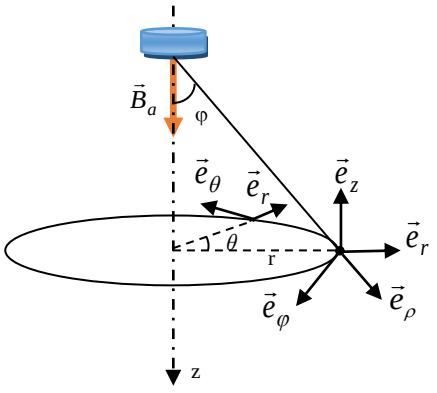

Fig .3. Représentation sphérique et cylindrique

En note par $\Delta z = z_p - z_a$, on exprime la composante radiale Br du champ magnétique [4] et de la tension induite normalisée aux bornes de la bobine par l'approximation dipolaire comme suit :

$$B_r(r,z) = \frac{3B_a r_a^2 h_a}{4} \frac{r\Delta z}{\left(r^2 + \Delta z^2\right)^{5/2}} \tag{8}$$

$$U_{ADn} = 2\pi r B_r = \frac{3\pi B_a r_a^2 h_a}{2} \sum_{p=1}^{N} \frac{r_p^2 \Delta z_p}{\left(r_p^2 + \Delta z_p^2\right)^{5/2}} \tag{9}$$

III. APPLICATION ET RESULTATS

Pour exploiter les deux modèles, nous avons repris une configuration aimant-bobine déjà traitée en [3].

L'aimant de type NdFeB, de hauteur 1.52mm et de rayon intérieur et extérieur respectivement de 1.59mm et 4.76mm. La bobine, composée de 1960 spires, a une hauteur de 4mm, de rayon intérieur de 6mm et extérieur de 11mm.

A. *Comparaison entre circuits couplés et approximation dipolaire*

La figure 4 montre la comparaison entre la tension induite normalisée calculée par les circuits couplés et celle de l'approximation dipolaire.

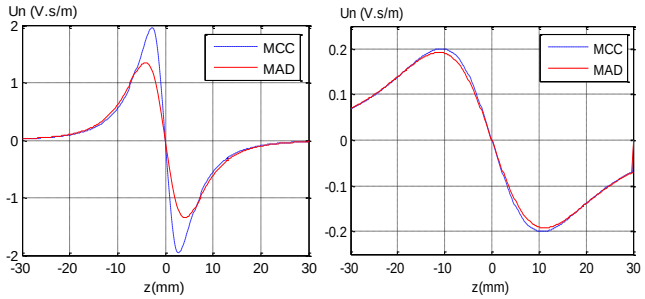

(a): $r_a/r_b = 0.75$ (b): $r_a/r_b = 0.24$

Fig .4. Tension normalisée : modèle des circuits couplés et modèle par approximation dipolaire

Dans Fig. 4.a, des écarts de résultats sont observés entre les deux modèles particulièrement dans la zone où l'aimant est proche de la bobine (-5<z<5) où l'approximation dipolaire n'est pas valable. Cependant, lorsque ra≪ρ, les résultats concordent bien. Dans Fig. 4.b, les deux modèles convergent avec une erreur qui ne dépasse pas 5% pour un rapport de 24%.

IV. CONCLUSION

Pour réduire le temps de calcul et de l'espace mémoire, le modèle de l'approximation dipolaire est adopté,lorsque l'aimant est suffisamment loin de la bobine. Dans le cas contraire et pour plus de précision, on utilise le modèle des circuits électromagnétiques couplés.

REFERENCES

[1] A. Munaz, B. C. Lee, and G. S. Shung, "A study of an electromagnetic energy harvester using multi-pole magnet,", Korea, Sensors and Actuators A 201,pp.134– 140, 2013 .

[2] B. Maouche, R. Alkama,and M. Feliachi, "Semi-analytical calculation of the impedance of a differential sensor for eddy current non-destructive testing,",Algeria, pp.573–580, 2009.

[3] S-D Kwon1, J. Park2 , K. Law, "Electromagnetic energy harvester with repulsively stacked multilayer magnets for low frequency vibrations",Smart Materials and Structures,vol22,2013.

[4] G Donoso, C L Ladera ,P Mart´ın, "Magnet fall inside a conductive pipe: motion and the role of the pipe wall thickness", European Journal Of Physics, 855–869, 30 ,2009.

Modeling of Skin/Sensor Contact Impact on EEG Signals Encountred in Neurosciences

Assia Ait Hamou
Electrotechnics Department, Faculty of Electrical Engineering and Computer Science
Mouloud Mammeri University,
Tizi Ouzou, Algeria
aichourassia612@gmail.com

Sara Sahraoui
Orthophony Department.Faculty of Humanity and Social Sciences
Mouloud Mammeri University,
Tizi Ouzou, Algeria
sara.sahraoui@ummto.dz

Hassane Mohellebi
Electrotechnics Department, Faculty of Electrical Engineering and Computer Science
Mouloud Mammeri University,
Tizi Ouzou, Algeria
hass.2000@yahoo.com

***Abstract*—The present work concerns the development of a model which have the capability to represent accurately the skin/sensor contact in an electromagnetic problem study. The later consist of elctro-encyphalography (EEG) signals encountered in neuroscience health diagnosis. The electromagnetic problem studied is governed by Poisson's equation and solved using finite element method. The skin/sensor contact is modeled by an analytical solution, which is coupled to finite element resolution. The signals induced by neuronal equivalent current are presented and investigated. A comparison with existing results is then performed.**

Keywords—numerical modeling, analytical solution, skin/sensor contact, EEG signal, neuroscience, diagnosis.

I. INTRODUCTION

Inter-cerebral activity of electrical origin generates a potential difference between two positions of the human scalp. The signals resulting from this potential difference are recorded using an encephalogram (EEG). In the case of the development of mental processes such as: sensation, perception, cognitive processing, intentional mechanisms, motor acts or mental imagery a change in electrical potential appears near the surface of the scalp [1].

The current study focuses on the modeling of the skin/sensor contact with an analytical solution on the air-gap area governed by 2D Laplace's equation. The latter is solved using separation variables method [2]. The others parts of the solving domain are solved by finite elements method. A coupled model between finite elements and analytical solutions is then build and applied to the study of EEG signal produced by an equivalent neuronal current [3]. The results obtained using coupled model are compared to those given by finite elements solution. The capability of the coupled model to take account of thin air-gap is highlighted compared to the use of finite elements method.

II. POISSON'S EQUATION SOLUTION

A. Poisson's Equation

The 2D Poisson's equation to be solved in the current study is deduced from Maxwell's equations (1) and (2) by considering static mode. In this case, the unknown variable to be considered is the electric scalar potential V.

$$\vec{\nabla}.\vec{D} = \rho \tag{1}$$

$$\vec{\nabla} \wedge \vec{E} = 0 \tag{2}$$

$$\vec{D} = \varepsilon\, \vec{E} \tag{3}$$

From (2), we deduce: $\vec{E} = -\vec{\nabla}V$ (4)

$$\varepsilon = \varepsilon_0 \varepsilon_r \tag{5}$$

By introducing (3) and (4), equation (1) becomes:

$$\vec{\nabla}.\left(-\varepsilon_0 \varepsilon_r\, \vec{\nabla}V\right) = \rho \tag{6}$$

The partial differential equation form in Cartesian coordinates is given as following:

$$\frac{\partial}{\partial x}\left(\frac{\partial V(x,y)}{\partial x}\right) + \frac{\partial}{\partial y}\left(\frac{\partial V(x,y)}{\partial y}\right) = -\frac{\rho(t)}{\varepsilon_0 \varepsilon_r} \tag{7}$$

$\vec{E}$ is the electrical field vector [V/m],$\vec{D}$ is the displacement current [A.s/m^2] and ρ(t) is the electrical charge density considered as analytical function of time[C/m^3] [1].
ε_0 is the electric permittivity of vacuum [F/m] and ε_r is the relative electric permittivity.

B. Solution of Laplace Equation in the air-gap

The Laplace equation in air-gap between skin and sensor is:

$$\frac{\partial^2 V(x,y)}{\partial x^2} + \frac{\partial^2 V(x,y)}{\partial y^2} = 0 \tag{8}$$

The solution of (8) is obtained using variables separations technique with the associated boundary conditions f(x) and shown in Fig. 1.

$$V(b,y) = 0 \quad (9.a)$$
$$V(0,y) = 0 \quad (9.b)$$
$$V(x,y_1) = g(x) \quad (9.c)$$
$$V(x,y_2) = f(x) \quad (9.d)$$

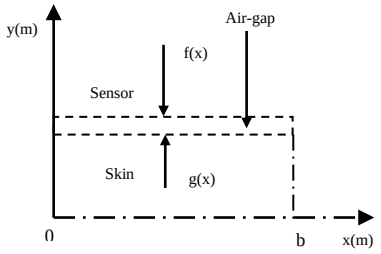

Fig. 1. Air-gap (Skin/sensor interface)

The analytical solution obtained after resolution, using variables separation method, is given by as follows [4]:

$$V^{an}(x,y) = \sum_{i=1}^{n\,t}\Big(\sum_{n=0}^{\infty} V_{ni}\frac{N_{ni}}{D_{ni}}\sin(\lambda_n x)\Big)V_i \tag{10}$$

$$N_{ni} = \sinh(\lambda_n y) - \tanh(\lambda_n\, dy')\cosh(\lambda_n y) \tag{11}$$

$$D_{ni} = \sinh(\lambda_n\, dy') - \tanh(\lambda_n\, dy)\cosh(\lambda_n\, dy') \tag{12}$$

$$\lambda_n = \frac{n\pi}{b} \tag{13}$$

if i= 1, 2,…, n_1 then dy'= y_2 and dy= y_1

if i= n_1+1,…, n_t then dy'=y_1 and dy =y_2
The normal derivative of analytical solution is given by:.

$$\frac{\partial V^{an}}{\partial n} = \vec{\nabla} V^{an} . \vec{n} \qquad (14)$$

$\vec{n}$ is the normal derivative vector.

The condition at the air-gap frontiers is assumed to be:

$$\varepsilon_1 \frac{\partial V^{FE}}{\partial n} = \varepsilon_2 \frac{\partial V^{an}}{\partial n} \qquad (15)$$

V^{FE} and V^{an} are the Finite elements analytical unknowns respectively.

.

C. *Finite Elements Formulation*

The finite element formulation of Poisson's equation using Galerkin method is expressed as fellow:

$$\iint_{\Omega} \left(\vec{\nabla}\phi_i . \vec{\nabla} V\right) dxdy - \int_{\Gamma} \phi_i \frac{\partial V^{FE}}{\partial n} d\Gamma - \iint_{\Omega} \phi_i \frac{\rho}{\varepsilon} dxdy = 0 \quad (16)$$

By introducing (12) in (13) and after assembly, we obtain the algebraic system bellow:

$$([S]+[I])[V]=[K] \qquad (17)$$

$$S_{ij} = \iint_{\Omega} \left(\vec{\nabla}\phi_i . \vec{\nabla}\phi_j\right) dxdy \quad (18) \qquad I_{ij} = \int_{\Gamma} \phi_i \frac{\partial \phi_j^{an}}{\partial n} d\Gamma \quad (20)$$

$$K_i = \iint_{\Omega} \phi_i \frac{\rho}{\varepsilon} dxdy \qquad (19)$$

The resolution of the algebraic system (17) at each time step permits the computation of the electric potential in the meshed and the non-mesh sub domains with fixed air-gap.

III. Application and Results

The coupled model developed is applied to study the effect of the air-gap between skin and sensor on electroencephalograph signal of a neuroscience device. The solving domains related to the coupled problem are shown in Fig. 2. The electric potential distribution is shown in Fig. 3.

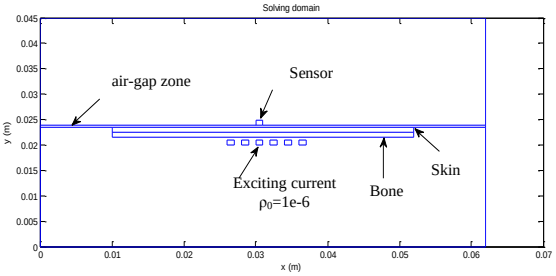

Fig. 2. Geometry of the solving domain

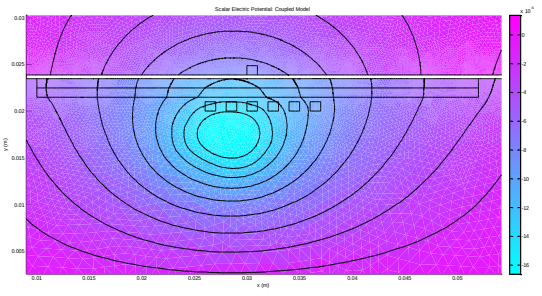

Fig. 3. Electric potential distribution (Coupled model)

We note that with 2µm of air-gap the FE mesh is not possible because of very small surface of triangles (Table I). In Fig. 4 and Fig. 5 are given the FE results for air-gap higher than 2µm. The coupled finite elements-analytical model permits to realize a simulation by considering the air-gap width less than 2µm in the FE-AN model with analytical solution because air-gap is note meshed (Fig. 3 and Fig.7).

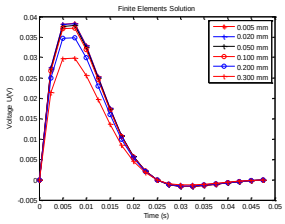

Fig. 4. Voltage variation (FE)

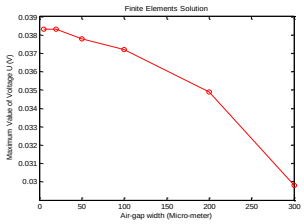

Fig. 5. Maximum Voltage (FE)

In Table I are given the nodes numbers considered for each finite elements and coupled (FE-AN) resolutions according to the air-gap thickness variation. We can see that the number of unknowns grows drastically in case of FE model and induces a higher computational resolution time.

TABLE I. TNodes Numbers Comparison

Air-gap (µm)	50	20	5	2	1
Nodes (FE)	118853	181169	288470	-	-
Nodes (FE-AN)	19433	29676	38609	17416	17416

In Fig. 6 are presented relatives values of the sensor voltage for both FE and FE-AN models. The results are quit comparable and then permits to conclude to the validity of the developed model. The results given in Fig. 7 shows the sensor voltage obtained for small air-gaps (1 µm, 2 µm and 5µm). This allows us to confirm the high capability of the FE-AN model than the FE one for contact modeling.

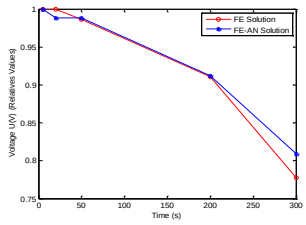

Fig. 6 Maximum Voltage

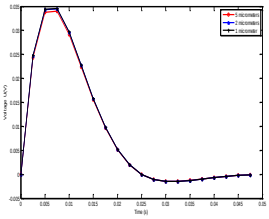

Fig. 7 Voltage variation (FE-AN)

The capability of the proposed FE-AN model in the modeling of the contact between sensor and the skin highlight the effects on the sensor voltage level. The later could influence EEG signal received and consequently the diagnostic nature knowing that the equivalent neuronal current source level for a macro column of neurons is made up of the activity of 10^4 to 1 million neurons.

References

[1] R. A. Salidoruiz," Problèmes inverses contraints en EEG : Applications aux potentiels absolus et à l'influence du signal de référence, " Thèse Ph. D., Université de Lorraine, 2012, France.

[2] H. Mohellebi, A. Ait Hamou,'' Current density computation of NDT probe taking into account of velocity effect,'' ENDE'2023 , 28-30 June 2023, Thessaloniki, Grèce.

[3] L. Garnero, S. Baillet, & B. Renault," Magnétoencéphalographie /E1ectroencephalographie et imagerie cérébrale fonctionnelle", *Annales de L'Institut Pasteur/ actualites*,vol. 9, no. 3, pp. 215-226, 1998.

[4] Internal Report, september 2023, Tizi-Ouzou University, Algeria.

Session 4 (Orale):

Numerical and Analytical Solution of PDEs (II)

- Visualization of Magnetic Flux Density for Non-Destructive Testing: A Brief Technical Review from Meters to Micrometers Resolution
- Modélisation 3D de l'influence des dépendances de la température ou du champ magnétique sur la courbe d'hystérésis dans les supraconducteurs à HTc
- General Properties of Global and Blow-up Solutions For Parabolic Equation of Fractional Order
- Transient hybrid model based on the strong coupling of magnetically coupled electric circuits and reluctance network
- Analytical Modeling and Simulation of Self-excited Double Stator Induction Generator for Autonomous Operating Mode
- L'influence de la densité de courant Jc sur le comportement magnétothermique de limiteur du courant de défaut supraconducteur (SFCL)

Visualization of Magnetic Flux Density for Non-Destructive Testing: A Brief Technical Review from Meters to Micrometers Resolution

Jinyi Lee
Department of Electronic Engineering
Chosun university
Gwangju, Republic of Korea
0000-0001-9470-2000

I Dewa Made Oka Dharmawan
Interdisciplinary Program in IT-Bio Convergence System
Chosun university
Gwangju, Republic of Korea
0000-0003-4425-9463

***Abstract*—The advanced utilization of alloys and steel in critical engineering systems underscores the need for rapid, effective, and reliable nondestructive testing (NDT) methods. This study explores breakthrough NDT techniques by visualizing magnetic flux density (MFD) at the material surface, including magnetic particle inspection (MPI), magnetic flux leakage testing (MFLT), magnetic metal memory (MMM), and Eddy current testing (ECT). Significant advancements in each method are discussed, particularly how they simplify defect detection through advanced integrated image processing techniques. We present innovative approaches for quantitatively imaging MFD, utilizing arrays or scanning magnetic sensors. These techniques have been successfully applied to the nondestructive testing of express train wheels and small-bore piping in heat exchangers. Additionally, we introduce a novel method for three-dimensional vector imaging of MFD within metal grains, offering a comprehensive view of potential defects at the microstructural level.**

Keywords—magnetic flux density,nondestructive testing,Faraday effect,sensor array,train wheel, heat exchanger, grain, domain

I. INTRODUCTION

The increased use of advanced alloys and steel in engineering systems has driven the need for rapid, straightforward, and dependable methods to maintain their structural integrity. As societies and economies rely heavily on the optimal performance of these materials, it becomes essential to conduct regular structural assessments. These evaluations ensure that the systems not only operate safely but also achieve their intended performance over their entire design lifespan. Nondestructive testing (NDT) plays a crucial role in these assessments by providing a means to inspect materials, parts, and structures without compromising their integrity. This capability is particularly important in sectors where the failure of a component could lead to significant financial loss or, worse, catastrophic safety incidents.Among the NDT techniques employed, those measuring magnetic flux density (MFD) at the material surface are particularly noteworthy. These include magnetic particle inspection (MPI), magnetic flux leakage testing (MFLT), magnetic metal memory (MMM), and eddy current testing (ECT).Here, ECT measures the amplitude and phase of time-varying induced MFD.

On the other hand, we know that visualizing and imaging the distribution of MFD offers the advantage of easily identifying defects, and various image processing methods can be actively utilized to improve their capabilities. In this study, we will explore the recent breakthroughs in MFD measurement and their specific applications for NDT. It includes case studies that quantitatively measure and image MFD by arraying or scanning magnetic sensors (referred to hereafter as a 'magnetic camera') and using them for NDT of express train wheels and the small-bore piping in heat exchangers. Additionally, we present a three-dimensional vector imaging method for MFD in metal grains.

II. VISUALIZATION OF MFD AND APPLICATION IN NDT

A. Magneto-Optical Non-Destructive Inspection

The Magneto-optical (MO) Faraday Effect, commonly referred to as MOE, is an intriguing and effective method for imaging the distribution of static and time-varying MFD in surface inspection. MOE operates based on the Faraday rotation (FR) effect, which corresponds to the transformation of polarized light transmitted through magnetic material. In non-destructive inspection, MOE contributes to investigating the distribution of distorted magnetic domains caused by the presence of defects. The MO non-destructive inspection (MONDI) system operates based on the Faraday rotation effect, which affects the behavior of light propagation through a magnetized medium [1–4]. An MO sensor is used to detect the MFL distribution around a crack, offering high spatial resolution. In this presentation, the prediction of the shape and direction of a defect using the transfer learning method and the MONDI system will be presented.

B. Train Wheels Inspection using Magnetic Camera[5]

Two individual InSb Hall sensors are combined to form a single differential-type Hall sensor (D-HaS) spaced 0.52 mm apart. Each pair of sensors measures the differential magnetic field at the position of each sensor. The D-HaSs are arranged on a NiZn ferrite wafer to create a large detection area. The differential magnetic intensity can be measured by crossing an input signal row with an output signal column.

To inspect the large wheel tread area while avoiding the train's weight, sensors are embedded into each rail half. Permanent magnets (Nd–Fe–B) are placed beneath the sensors to induce a vertical magnetic field in the wheel, with a maximum field strength of 200 mT. These magnets and sensors are supported by a flexible fixture jig, which protects the system from the train's weight and any contact with the wheel. Each half of the wheel tread can be inspected sequentially over the course of the first- and second-wheel rotations. Additionally, a photodiode is positioned near the first sensor to signal the train's entry into the sensor region.This presentation will cover how to inspect wheel tread at train speeds ranging from approximately 1.17 to 30 km/h.

C. *Small Bore Piping of Heat Exchanger* [6,7]

When a time-varying magnetic field is applied using one or two exciting coils, the current density induced in a metallic specimen becomes distorted and changes at the location of a defect. Consequently, the distribution of MFD varies not only in amplitude, which reflects the size of the defects, but also in phase, indicating their position. By employing a cylindrical array of semiconductor-based magnetic sensors, such as Hall sensors or GMR sensors, with sizes ranging from 0.5 to 1.3 mm, it is possible to assess the existence, location, and size of defects. On the other hands, a biased electric motive force (EMF) can occur due to domestic magnetization in δ-ferrite structures of metallic specimens, ferromagnetic foreign materials, and high permeability components such as a tube support plate (TSP). This bias affects not only coil sensors but also semiconductor-based magnetic sensors, as the local magnetization direction influences the sensor readings.

Bobbin-type magnetic cameras that array semiconductor-based magnetic sensors circumferentially in the axial direction. And cylinder-type magnetic camera integrates multiple bobbin-type sensor array. A wide bobbin coil is wound at the top side where the sensors are positioned. By applying alternating current to the bobbin coil and activating a column of circumferentially arrayed magnetic sensors, the device effectively constructs a bobbin-type magnetic camera. Here, the exciting coil generates the Lissajous signal typical of first-generation ECT, while the magnetic sensors detect the time-varying MFD characteristic of third-generation ECT.Furthermore, by positioning a cylinder-type magnetic camera where a defect signal is detected and activating matrix-type array sensors through electrical scanning, it is possible to eliminate the bias EMF signal caused by mechanical scanning. Since the output around defects induced by the exciting coil is alternating current, the bias DC output resulting from localized magnetization applied to the sensor can be efficiently filtered out using a high pass filter (HPF). Therefore, this system not only outputs first, second, and third-generation ECT signals but also removes bias output signals generated by localized magnetization of the specimen.

D. *3D Magnetic Flux Density Inside a Grain [8]*

We have developed a measurement system capable of imaging the three-dimensional distribution of MFD in a ferromagnetic material. Our methodology combines a three-axis tunnel magnetoresistance (TMR) sensor with microscopic imaging to visualize the MFD distribution within a grain. By integrating surface polishing techniques, we captured the MFD on each surface layer, and by slicing through these layers, we achieved a detailed visualization of the MFD across a single bulk grain.

One of the major intellectual challenges was merging TMR data with microscopic images, requiring precise alignment and integration of data from diverse sources. To accurately track the specimen's position based on TMR data alone, we coiled three turns of a 0.1-mm enameled wire around the specimen. This coil setup served as an anchor, allowing precise tracking of the material's position based on the edge effect of the stray field. Furthermore, we then compiled all the collected MFD data, aligning it with the boundary coordinates from three orthogonal perspectives to construct a comprehensive 3D representation of the MFD within the grain (Figure 1).

ACKNOWLEDGMENT

This research was supported by the National Research Foundation of Korea and funding from the Ministry of Science and Technology, Republic of Korea. (No.RS-2023-00242712).

REFERENCES

[1] J. Lim, H. Lee, J. Lee, and T. Shoji, "Application of a NDI method using magneto-optical film for micro-cracks," KSME International Journal, vol. 16, no. 5, pp. 591–598, May 2002, doi: 10.1007/BF03184808

[2] C. Xu, G. Xu, J. He, Y. Cheng, W. Dong, and L. Ma, "Research on rail crack detection technology based on magneto-optical imaging principle," Journal of Physics: Conference Series, vol. 2196, no. 1, p. 012003, Feb. 2022, doi: 10.1088/1742-6596/2196/1/012003.

[3] M. Le, J. Lee, T. Shoji, H. M. Le, and S. Lee, "A Simulation Technique of Non-Destructive Testing using Magneto-Optical Film," 2011. https://www.researchgate.net/publication/267261713

[4] J. Lee and T. Shoji, "Development of a NDI system using the magneto-optical method 2 Remote sensing using the novel magneto-optical inspection system," Hihakai Kensa, vol. 48, no. 4, pp. 231–236, 1999

[5] M. Le, J. Jun, J. Kim, J. Lee, "Nondestructive testing of train wheels using differential-type integrated Hall sensor matrixes embedded in train rails", NDT&E International, Vol.55, pp.28-35, 2013.

[6] M. Le, H. H. T. Vu, D. Wang, and J. Lee, "Development of Electromagnetic Cylinder-Type Probe for Inspection of Heat Exchanger Tubes," IEEE Transactions on Magnetics, vol. 58, no. 3, pp. 1–9, Mar. 2022

[7] M. Le, J. Kim, J. Kim, H. S. Do, and J. Lee, "Nondestructive testing of moisture separator reheater tubing system using Hall sensor array," Nondestructive Testing and Evaluation, vol. 33, no. 1, pp. 35–44, Jan. 2018, doi: 10.1080/10589759.2017.1331231.

[8] I. Dharmawan, J. Lee, D. Wang, J. Kim, "Measurement of three-dimensionjal distribution of magnetic flux density inside a gran of ferromagnetic materials: An experimental investigation," Measurement,vol.222,p.1-16,2023

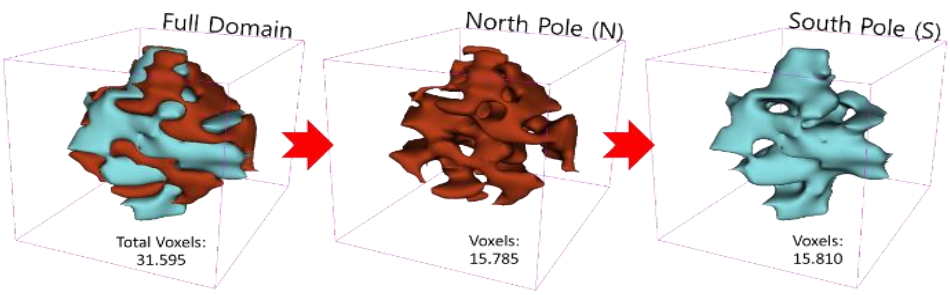

Fig. 1. Visualizing the 3D distribution of MFD within a grain

Modélisation 3D de l'influence des dépendances de la température ou du champ magnétique sur la courbe d'hystérésis dans les supraconducteurs à HTc

Khene Mohamed Lotfi, Lotfi Alloui*, Benmebarek Fethi, Mimoune Souri Mohamed,
Electrical Engineering and Industrial Electronics Laboratory (L2EI)
Département d'Electrotechnique Laboratoire de Modélisation des Systèmes Energétiques LMSE, Université de Biskra
Biskra, Algérie
*email :lotfi.alloui@univ-biskra.dz

***Résumé**--cet article présente les résultats de simulation de l'influence de la dépendance en température et en champ magnétique sur la courbe d'hystérésis magnétique dans les matériaux supraconducteurs a HTC. La méthode des volumes finis dans sa version tridimensionnelle est utilisée pour discrétiser les EDP décrivant les phénomènes électromagnétiques et thermiques couplés pour l'étude de la courbe d'hystérésis dans ce type de matériaux.*

***Mots Clés-** Supraconducteur, Hystérésis magnétique, Modélisation 3D, Méthode des volumes finis, modèle de KIM.*

I. INTRODUCTION

Un matériau supraconducteur est défini par une résistivité zéro et un flux magnétique zéro à l'intérieur de celui-ci, tandis que les supraconducteurs de type II présentent une pénétration partielle de flux, où le flux traverse de petits tubes dans l'état normal. Les tubes de flux entraînent une mémoire qui provoque une hystérie, entraînant ainsi des pertes. En produisant un courant de transport adéquat, une force de Lorenz se produit, ce qui entraîne des tubes de flux, ce qui entraîne la disparition de l'effet mémoire inhérent, ainsi que de l'hystérie. Il est possible d'observer une saturation dans les mesures de perte lorsque le courant critique approche [1]. L'étude de l'hystérésis magnétique dans les matériaux supraconducteurs est essentielle pour comprendre les pertes de courant électrique, car elles sont l'une des principales causes de pertes dans ces câbles [2]. Pour cela, dans cet article nous avons développé un code de calcul 3D basés sur la formulation A-V et qui utilise la méthode de volume fini MVF pour résoudre le problème électromagnétique et thermique non linéaire couplé en vue l'étude de l'influence de la dépendance en température et en champ magnétique sur la courbe B(H).

II. METHODES D'ANALYSE MATHEMATIQUE ET NUMERIQUE

La courbe d'hystérésis dans les supraconducteurs doit être simulée après la magnétisation par l'application d'un champ magnétique alternatif. Afin de trouver une solution au problème électromagnétique, nous avons utilisé une formulation électromagnétique en trois dimensions (3D) en A-V fournie par [3-4]. le problème thermique est résolu par résolution de l'équation de diffusion de la chaleur [5-10].

III. LES PARAMTRES DE SIMULATION

Dans notre étude, nous utilisons un matériau supraconducteur à haute température critique (SHTc) en GdBaCuO de taille rectangulaire 33x33x20 mm^3. Celle-ci est placé au centre d'un solénoïde magnétisant traversé par une impulsion de courant (Fig. 1). Le solénoïde produit un champ magnétique extérieur sinusoïdal avec une fréquence de 50 Hz pendant une durée de 20 ms (Fig. 1).

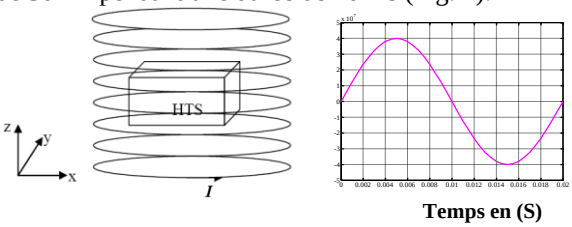

Fig.1. Dispositif d'étude. allure du champ magnétique appliqué.

Résultats et interprétations

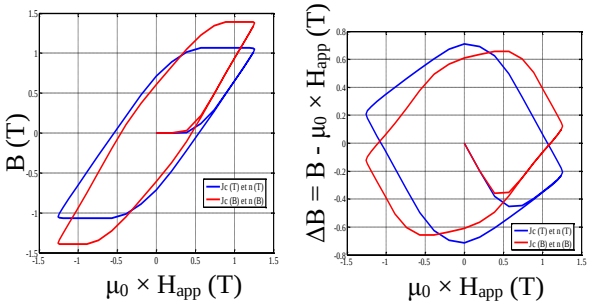

Fig.2. Évolution de l'induction magnétique dans le supraconducteur en fonction de champ magnétique appliqué pour les deux modèles (***E-J-T)*** et (***E-J-B)***.

L'induction magnétique piégée B dans la pastille en fonction du champ magnétique appliqué est représentée dans la Fig.2. L'échantillon est dans l'état diamagnétique lorsque le champ magnétique appliqué commence à augmenter à partir de zéro. La magnétisation augmente lorsque certains courants pénètrent dans la pastille supraconductrice. La fig.3. présente la courbe d'hystérésis magnétique ΔB = B–μ0×Happ en fonction de champ magnétique applique pour μ0×Happ dans le SHTc pour les deux modèles, le premier modèle prend en compte la dépendance en température ***(E-J-T)*** et le second avec la dépendance en champ magnétique ***(E-J-B)***. Les cycles d'hystérésis montrent le comportement diamagnétique des matériaux SHTc (inclinaison négative à l'origine) et le supraconducteur présente une aimantation négative en dessous de la température critique lorsqu'il est refroidi sous champ. Ainsi, l'allure de la courbe d'hystérésis présentée dans la fig.3. Elle explique la différence entre les deux modèles, ***E-J-T*** et ***E-J-B.***

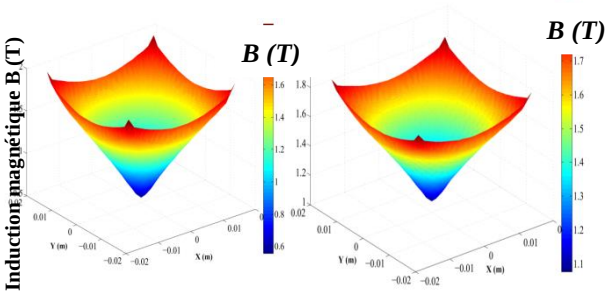

Fig.3. Distribution de l'induction magnétique piégé B à z = 5 mm au dessus de la surface supérieur du matériau SHTc avec le modèle qui prend la dépendance en température (***E-J-T) et* (*E-J-B)***.

La distribution du champ magnétique B qui est atteinte au régime permanent par le matériau SHTc aimanté est illustrée à la Figu.3. La première figure avec le modèle qui prend en compte la dépendance en température (***E-J-T)*** et la seconde avec la dépendance en champ magnétique (***E-J-B)***. Le champ magnétique présenté est calculé à z = 0,5 mm sur la surface supérieure du matériau SHTc aimanté pour Hm = 4×10^7 A/m. Les résultats montrent que le champ magnétique piégé a une forme concave pour les deux modèles.

La distribution de la température au sein de la pastille supraconductrice est illustrée dans la fig.4. pour les deux modeles (***E-J-T) et*** (***E-J-B)***. La température à l'intérieur de la pastille augmente graduellement au fil du temps. La température se répartit d'une manière non homogène à l'intérieur de la pastille, le centre de la pastille semble le plus froid, mais la température est plus élevée aux extrémités de la pastille, ce qui peut être expliqué par la variation du champ magnétique appliquée pendant l'aimantation de la pastille SHTc, ce qui provoquera une densité de courant critique plus élevée et, par conséquent, l'augmentation de la densité de puissance et par conséquent l'augmentation de la température au sein de la pastille supraconductrice. Selon les résultats de simulation présentés, la température maximale du supraconducteur pour le modèle de dépendance en température atteint une valeur maximale de 28°K, mais pour le modèle qui prend la dépendance en champ magnétique, le supraconducteur atteint une température maximale de 25.5°K.

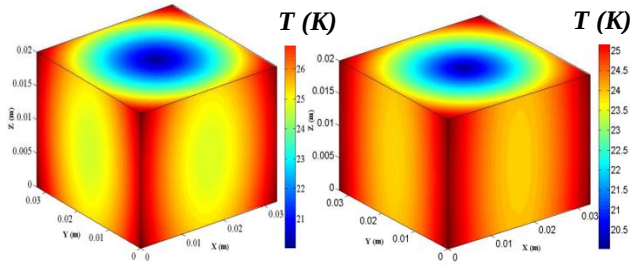

Fig.4. Répartition spatiale de la température T au sein du matériau SHTc avec le modèle qui prend la dépendance en température ***(E-J-T) et*** (***E-J-B)***.

IV. Conclusion

Dans ce document, nous avons utilisé deux modèles de comportement différents pour simuler le comportement magnétique et thermique du matériau supraconducteur à la base de la MVF pour étudier le cycle d'hystérésis magnétique. Le premier prend en compte la dépendance en T, tandis que le second prend en compte la dépendance en B. Les résultats de la simulation ont montré qu'il existe une différence entre les deux modèles, donc des mesures expérimentales doivent être menées pour valider les résultats de la simulation.

References

[1] Mårten Sjöström, " Possibilities and limitations of using Preisach model for hysteresis in superconductors s", Physica B: Condensed Matter, Volume 306, Issues 1–4, 2001, Pages 256-260.

[2] E. Pardo, A. Sanchez and C. Navau, "Theoretical AC susceptibility of superconducting multifilamentary tapes in a perpendicular field," in IEEE Transactions on Applied Superconductivity, vol. 13, no. 2, pp. 3566-3569, June 2003

[3] M.L. KHENE, L. ALLOUI, F. BOUILLAULT, A. KAMENI, S.M. MIMOUNE, et M. FELIACHI " 3-D Numerical Evaluation of Trapped Magnetic Field and Temperature of a Rectangular GdBaCuO Bulk Magnetized by MMPSC Method ", IEEE TRANSACTIONS ON MAGNETICS, VOL. 51, NO. 3, 2015.

[4] M.L. KHENE, L. ALLOUI, S.M. MIMOUNE, F. BOUILLAULT, et M. FELIACHI " 3D analysis of applied field effect on trapped magnetic field during pulsed field magnetization of bulk superconductor " , EPJ Applied Physics, 66: 10601, 2014.

[5] L. Alloui, F. Bouillault and S.M. Mimoune, 'Numerical study of the influence of flux creep and of thermal effect on dynamic behaviour of magnetic levitation systems with a high-Tc superconductor using control volume method,' Eur. Phys. J. Appl. Phys. 45, 20801. 2009.

[6] MOHAMED LOTFI KHENE, LOTFI ALLOUI, SOURI MOHAMED MIMOUNE, MOULOUD FELIACHI, et FRÉDÉRIC BOUILLAULT " Comparison of Trapped Magnetic Field of HTS Bulk during Magnetization Process with MPSC and MMPSC Methods ", NUMELEC, Conférence Européenne sur les Méthodes Numériques en Electromagnétisme, 2015.

[7] L. M. Khene, L. Alloui, F. Benmebarek, S. M. Mimoune, '3D Simulation of the influence of the external magnetic field on superconducting permanent magnets'. Physica C, Superconductivity and its applications 609. 2023.

[8] F. Benmebarek, L. Alloui, L.M. Khene, A. Kameni, H. Becha, T. Azib, S.M. Mimoune, '3D modeling of magneto-thermal phenomena in superconductors with defects', Physica C: Superconductivity and its Applications, Volume 613, 2023.

[9] R. BOUMARAF, S. M. MIMOUNE, L. ALLOUI et M. L. KHENE " Increasing flux density by HTS shielding pellet in superconducting synchronous machine based on flux concentration ", Int J Syst Assur Eng Manag 5(4) : 637–644, 2014.

[10] K. BERGER, J. LÉVÊQUE, D. NETTER, B. DOUINE, et A. REZZOUG " Influence of Temperature and/or Field Dependences of the E J Power Law on Trapped Magnetic Field in Bulk YBaCuo ", IEEE TRANSACTIONS ON APPLIED SUPERCONDUCTIVITY, VOL. 17, NO. 2, 2007.

General Properties of Global and Blow-up Solutions For Parabolic Equation of Fractional Order

1st Bilal Basti
Department of Mathematics
Ziane Achour University of Djelfa
Djelfa, Algeria
bilalbasti@gmail.com

2nd Rabah Djemiat
Department of Mathematics
Mohamed Boudiaf University of M'sila
M'sila, Algeria
rabahdjemiat19@gmail.com

***Abstract*—This paper investigates the problem of existence and uniqueness of global or blow-up solutions under the traveling profile forms for a free boundary problem of a one-dimensional space-fractional heat equation. It does so by applying the properties of Schauder's and Banach's fixed point theorems. For application purposes, some examples of explicit solutions are provided to demonstrate the usefulness of our main results.**

***Index Terms*—fractional heat equation, global or blow-up solutions, existence and uniqueness**

I. Introduction

This paper particularly addresses and discusses some analytical studies on the existence and uniqueness of global or blow-up solutions under the traveling profile forms for a free boundary problem of diffusion equations of moving fractional order as follows

$$\partial_t \omega = \kappa \partial_x^{\alpha} \omega,\ \kappa \in \mathbb{R}^*,\ m-1 < \alpha \leq m \in \mathbb{N}_0 - \{0,1\}, \quad (1)$$

where $\partial_x^{\alpha} \omega = \mathcal{I}_{b(t)}^{m-\alpha} \partial_x^m \omega$, with b is a real function of time t. Also $\omega = \omega(x,t)$ is a scalar function of a space and time variables $(x,t) \in \Omega$ with

$$\Omega = \{(x,t) \in \mathbb{R} \times [0,T];\ b(t) \leq x \leq a(t) + b(t)\},$$

$a(t) > 0$ for any $t \in [0,T]$ and T may be an infinite or a finite nonnegative constant.

It does so by applying the properties of Schauder's and Banach's fixed point theorems.

The equation (1) becomes the transport equation for $\alpha = 1$ and the linear dispersive equations of Airy type for $\alpha = 3$.

Therefore, for $m = 2$, the space-fractional diffusion equation (1) becomes a space-fractional heat equation, in which the existence problems of its self-similar solutions and its scale-invariant solutions have been discussed in [2], [5], [8].

Our main goal in this work is to determine the existence, uniqueness and main properties of the global or blow-up solution in time of the fractional-order's PDE (1), under the traveling profile form (see [4]), which is

$$\omega(x,t) = c(t)\, \varphi\left(\frac{x - b(t)}{a(t)}\right), \quad (2)$$

This work has been supported by the General Direction of Scientific Research and Technological Development (DGRSTD)- Algeria.

the functions $a(t)$, $b(t)$ and $c(t)$ depend on time t and the basic profile φ are not known in advance and are to be identified.

This method permits us to reduce the fractional-order's PDE (1) to a fractional differential equation; the idea is well illustrated with examples in our paper. This approach (2) is very promising and can also bring new results for other applications in FPDEs.

II. Main Results

Throughout the rest of this paper, we have $J = [0,1]$ and $m-1 < \alpha \leq m$, with $m \geq 2$ is a natural number, $\kappa \in \mathbb{R}^*$ and $\lambda, \beta, \gamma, c_0, c_1 \in \mathbb{R}$. Also the functions $a(t)$, $b(t)$ and $c(t)$ depend on time t given by (2).

A. Statement of the Free Boundary Problem and Main Theorems

In this part, we first attempt to find the equivalent approximate to the following free boundary problem of the diffusion equation of moving fractional order

$$\begin{cases} \partial_t \omega = \kappa \partial_x^{\alpha} \omega, \ \ (x,t) \in \Omega, & \kappa \in \mathbb{R}^*, \\ \omega(b(t),t) = c_0 c(t), & c_0 \in \mathbb{R}, \\ \partial_x \omega(b(t),t) = c_1 \frac{c(t)}{a(t)}, & c_1 \in \mathbb{R}, \\ \partial_x^k \omega(b(t),t) = 0,\ k = 2, \ldots, m-1, & m \geq 3, \end{cases} \quad (3)$$

under the traveling profile form

$$\omega(x,t) = c(t)\, \varphi(\eta), \text{ with } \eta = \frac{x - b(t)}{a(t)}, \quad (4)$$

where

$$a(0) = c(0) = 1,\ b(0) = 0.$$

Now, we give the principal theorems of this work.

Theorem 1: Let $a(t)$, $b(t)$ and $c(t)$ be three real functions of time t, given by the traveling profile form (4). If for all $t \in (0,T)$

$$\frac{a^{\alpha}(t)}{|\kappa|}\left[\alpha\left(\left|\frac{\dot{a}(t)}{a(t)}\right| + \left|\frac{\dot{b}(t)}{a(t)}\right|\right) + \left|\frac{\dot{c}(t)}{c(t)}\right|\right] < \Gamma(\alpha+1), \quad (5)$$

then the problem (3) has at least one solution in the traveling profile form (4), which is global in time when $\dot{a}(t) > 0$, and it blows up in a finite time

$$0 < t < T = -\frac{a^{1-\alpha}(t)}{\alpha \dot{a}(t)} \text{ when } \dot{a}(t) < 0 \text{ and } \dot{c}(t) > 0.$$

Theorem 2: Let $a(t)$, $b(t)$ and $c(t)$ be three real functions of time t, given by the traveling profile form (4). If we put for all $t \in (0, T)$

$$\left(|\dot{a}(t)| + \left|\dot{b}(t)\right|\right) a^{\alpha-1}(t) < |\kappa| \Gamma(\alpha)$$

and

$$\frac{a^{\alpha}(t) |\dot{c}(t)|}{|\kappa| \Gamma(\alpha) - \left(|\dot{a}(t)| + \left|\dot{b}(t)\right|\right) a^{\alpha-1}(t)} < \alpha c(t), \quad (6)$$

then the problem (3) admits a unique solution in the traveling profile form (4), which is global in time when $\dot{a}(t) > 0$, and it blows up in a finite time

$$0 < t < T = -\frac{a^{1-\alpha}(t)}{\alpha \dot{a}(t)} \text{ when } \dot{a}(t) < 0 \text{ and } \dot{c}(t) > 0.$$

B. Existence and Uniqueness Results of the Basic Profile

We should first deduce the equation satisfied by the function φ in (4) and used for the definition of traveling profile solutions.

Theorem 3: The transformation (4) reduces the partial differential equation problem of space-fractional order (3) to the fractional differential equation of the form

$${}^{C}\mathcal{D}^{\alpha}_{0^+} \varphi(\eta) = g(\eta), \ \eta \in J, \quad (7)$$

where

$$g(\eta) = \lambda \varphi(\eta) + (\beta \eta + \gamma) \varphi'(\eta),$$

with the conditions

$$\begin{cases} \varphi(0) = c_0, \ \varphi'(0) = c_1, \text{ for any } m \geq 2, \\ \varphi^{(k)}(0) = 0, \ k = 2, 3, \ldots, m-1, \text{ for } m \geq 3, \end{cases} \quad (8)$$

where

$$(\lambda, \beta, \gamma) = \frac{a^{\alpha}(t)}{\kappa} \left(\frac{\dot{c}(t)}{c(t)}, -\frac{\dot{a}(t)}{a(t)}, -\frac{\dot{b}(t)}{a(t)} \right), \quad (9)$$

for some $\lambda, \beta, \gamma \in \mathbb{R}$.

In what follows, we present some significant lemmas to show the principal theorems.

Lemma 1: The problem (7)–(8) is equivalent to the integral equation

$$\varphi(\eta) = c_0 + c_1 \eta + \mathcal{I}^{\alpha}_{0^+} g(\eta), \ \forall \eta \in J. \quad (10)$$

where $g \in C(J, \mathbb{R})$ satisfies the functional equation:

$$g(\eta) = \lambda \left(c_0 + c_1 \eta + \mathcal{I}^{\alpha}_{0^+} g(\eta)\right) + (\beta \eta + \gamma) \left(c_1 + \mathcal{I}^{\alpha-1}_{0^+} g(\eta)\right).$$

Theorem 4: If we put

$$\alpha (|\beta| + |\gamma|) + |\lambda| < \Gamma(\alpha + 1), \quad (11)$$

then the problem (7)–(8) has at least one solution on J.

Theorem 5: If we put $|\beta| + |\gamma| < \Gamma(\alpha)$ and

$$\frac{|\lambda|}{\Gamma(\alpha + 1) - \alpha (|\beta| + |\gamma|)} < 1, \quad (12)$$

then the problem (7)–(8) admits a unique solution on J.

III. Conclusion

In this paper, we have discussed the existence and uniqueness of solutions for a class of two-dimensional space-fractional heat equations, which is known as the one-dimensional space-fractional heat equation with mixed free boundary conditions under the traveling profile form. The behavior of these solutions depends on some parameters that satisfy some conditions which make their existence global or local in a time T. For that we used the Banach contraction principle and Schauder's fixed point theorem, while Caputo's fractional derivative is used as the differential operator.

Acknowledgments. This work has been supported by the General Direction of Scientific Research and Technological Development (DGRSTD)- Algeria.

References

[1] B. Basti, Y. Arioua and N. Benhamidouche, *Existence results for nonlinear Katugampola fractional differential equations with an integral condition*, Acta Math. Univers. Comenianae, **89**(2) (2020), 243–260.

[2] B. Basti and N. Benhamidouche, *Existence results of self-similar solutions to the Caputo-type's space-fractional heat equation, Surveys in Maths. and its Applications*, **15** (2020), 153–168.

[3] B. Basti and N. Benhamidouche, *Global existence and blow-up of generalized self-similar solutions to nonlinear degenerate diffusion equation not in divergence form*, Appl. Math. E-Notes, **20** (2020), 367–387.

[4] N. Benhamidouche, *Exact solutions to some nonlinear PDEs, travelling profiles method*, Electronic Journal of Qualitative Theory of differential Equation **15** (2008), 1–7.

[5] E. Buckwar and Y. Luchko, *Invariance of a partial diffrential equation of fractional order under the Lie group of scaling transformations*, J. Math. Anal. Appl. **227**, No 1 (1998), 81–97.

[6] K. Diethelm, *The Analysis of Fractional Differential Equations*, Springer Berlin, 2010.

[7] A. A. Kilbas, H. H. Srivastava and J. J. Trujillo, *Theory and Applications of Fractional Differential Equations*, Elsevier B.V, Amsterdam, 2006.

[8] Y. Luchko and R. Gorenfl, *Scale-invariant solutions of a partial diffrential equation of fractional order*, Fract. Calc. Appl. Anal. **1**(1) (1998), 63–78.

[9] K. S. Miller and B. Ross, *An Introduction to the Fractional Calculus and Differential Equations*, John Wiley, New York, 1993.

[10] T. Pierantozzi and L. Vázquez, *An interpolation between the wave and diffusion equations through the fractional evolution equations Dirac like*, J. Math. Phys. **46** (2005), 113512.

[11] Polyanin A. D., Zaitsev V. F., *Handbook of Nonlinear Partial Equation*, Chapman&Hall/CRC, Boca Raton (2004).

Transient hybrid model based on the strong coupling of magnetically coupled electric circuits and reluctance network

Y. Messaoudi[1], M. Rachek[1], T. Merzouki[1],

[1]Department of Electrotechnics, Faculty of electrical and computer engineering, Mouloud Mammeri University, Algeria

This paper presents the development of an internal transient hybrid model based on the coupling between the voltage fed electric circuits modelled using on the Magnetically Coupled Electric Circuits approach (MCEC) and the magnetic components based on the Reluctance Network Method (RNM). The coupling between the (MCEC) and (RNM) models is insured through the magnetic flux and then lead to a transient differential algebraic equations system solved using the classical Runge-Kutta method. The calculated physical variables for transient operating are the currents in the electrical circuits, the fluxes and the magnetic potentials respectively of the magnetic branches and the nodes of the networks. The developed two-dimensional strongly coupled hybrid (MCEC)-(RNM) model can be used as an accurate and efficient tool for the optimal design and diagnosis of electromagnetic actuators.

***Index Terms*— Electromagnetic modeling, Magnetically coupled electric circuit, Magnetic reluctance network.**

I. Introduction

THE MODEL presented is able to accurately predict transient performances and behaviors of electromagnetic actuators fed from voltage source under various operation conditions. The proposed model is based on the **R**eluctance **N**etwork **M**ethod (RNM) which take in charge the magnetic components according the theirs geometrical topology and materials properties, strongly coupled with the **M**agnetically **C**oupled **E**lectric **C**ircuits (MCEM) approach associated with a the voltage fed windings configurations. The (MCEM) and (RNM) transient models coupled through the magnetic flux leads to differential equations system which solution at each time permit the behavioral analysis of electromagnetic phenomena's. The developed transient hybrid (MCEM)-(RNM) models code with an automated network mesh generator implemented under Matlab software.

II. Magnetic Reluctance Network Model

The magnetic circuit is discretized by magnetic branche Fig.1., which constitute the two-dimensional (2D) reluctance network mesh [1-2].

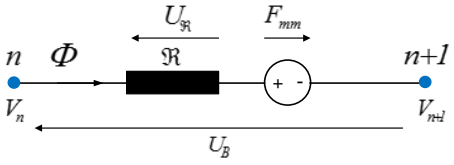

Fig.1. Magnetic potential differences in the active branch

The magnetic potential in the two nodes n and $n+1$ are respectively V_n and V_{n+1}, however the magnetic potential differences vector V expressed by equation (1) is established from Hopkinson law.

$$\{V\}=[A_{cm}]^T\{V\}=\{U_{\Re}\}-\{F_{mm}\}=[\Re]\{\Phi\}-[W]\{i\} \qquad (1)$$

Where $\{V\}$ is the nodes magnetic potentials vector, $[\Re]$ is $(b\times b)$ magnetic reluctance diagonal matrix, $\{i\}$ is the currents vector in of the electric circuits, and $[W]$ the $(b\times Q)$ transformation matrix of currents of the electric circuit into magnetomotive forces sources of the magnetic core.

In order to determine the node magnetic potentials vector is replaced in equation (2), and then we obtain:

$$[A_{cm}][\Re]^{-1}[A_{cm}]^T\{V\}+[A_{cm}][\Re]^{-1}[W]\{i\}=0 \qquad (2)$$

Finally, the magnetic algebraic equations system of the flux and the magnetic potentials differences is obtained as follow:

$$\begin{cases}\{V\}=\left([A_{cm}][\Re]^{-1}[A_{cm}]^T\right)^{-1}\cdot\left(-[A_{cm}][\Re]^{-1}[W]\{i\}\right)\\ \{\Phi\}=[\Re]^{-1}[A_{cm}]^T\{V\}+[\Re]^{-1}[W]\{i\}\end{cases} \qquad (3)$$

The algebraic equations system (3) describes the magnetic state of a reluctance networks according to the electric current due to the transient voltage fed winding's.

III. Electric Cicruit Magnetically Coupled

From the Ohm and Kirchhoff laws, the analytical relations between the voltages, the currents and the fluxes, can be expressed by the following matrix system:

$$\{v\}=[R]\cdot\{i\}+[L]\frac{d}{dt}\{i\} \qquad (4)$$

Where $\{v\}$ is the voltages vector, $[R]$ and $[L]$ are the resistances and inductances matrix respectively.

The time stepping hybrid model is based on the simultaneous resolution by the use of well-known Runge-Kutta algorithm of (MCEM) electrical equation (4) and (MRN) magnetic equations (3), to get the electric currents, magnetic flux, magnetomotive force and the magnetic force computed using the Lorentz formula.

IV. Application And Simulation

A. Problem definition

The studied electromagnetic actuator with detailed dimensions are given in [3] and shows by the Fig.2. The electromagnet magnetic circuit and the plate have the relative permeability of μ_r =2777. The coil of R=1 Ω resistance.

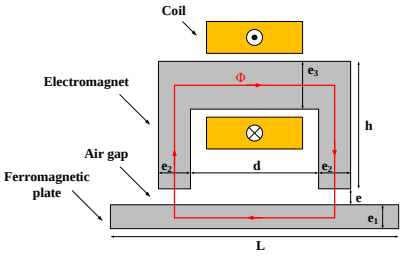

Fig.2. Electromagnetic actuator structure

The 2D mesh of electromagnetic actuator which is given by (Fig.2) is presented by Fig.3.

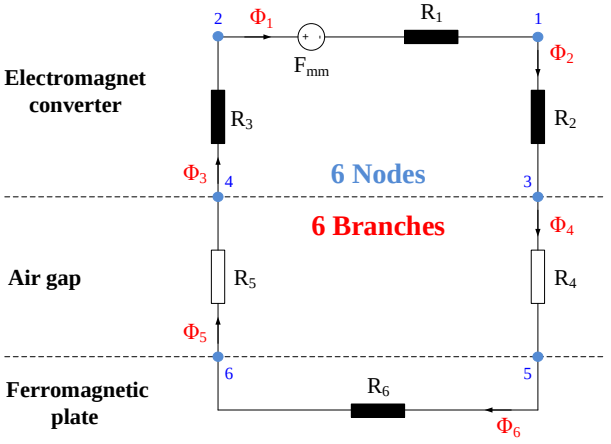

Fig.3. Reluctance network mesh

B. Simulations & discussions

The coil is supplied with sinusoidal voltage of 80V magnitude and frequency of 50Hz.

The Fig.4 gives expected behaviour of the current and magnetic flux. The phase difference between the current and the voltage is due to the inductive nature of the load.

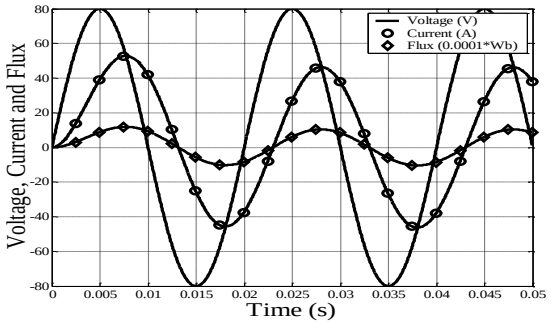

Fig.4. Voltage, current and flux

The Fig.5 shows that the magnetic potential difference in branch 6 (plate) is more important than magnetic potential difference in branch 2 with sinusoidal variations following the voltage source. In the Fig.6 we note the sinusoidal variations of the magnetic potential differences. The Fig.7 shows the transient and periodic evolution of the force applied on the ferromagnetic plate

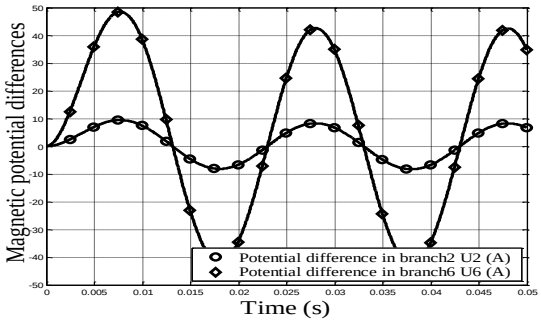

Fig.5. Potential differences - Ferromagnetic materials

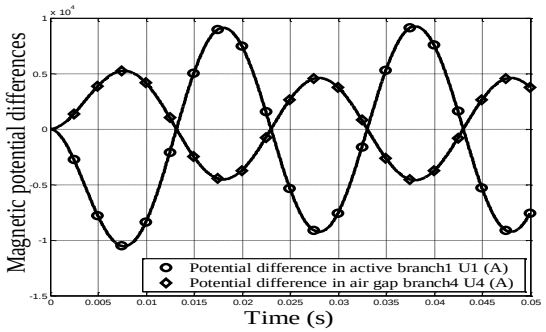

Fig.6. Potential differences - Air gap and active branch

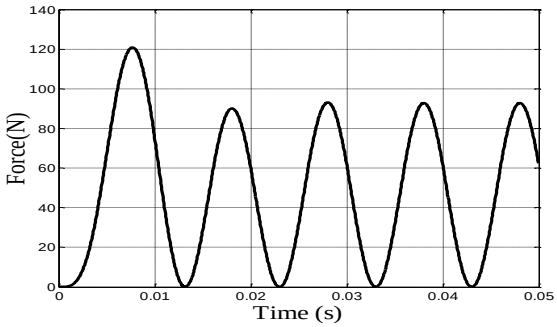

Fig.7. Force applied on the plate – Sinusoidal voltage supply

V. Conclusion

In this paper a method for the electric and magnetic transient analysis of electromagnetic devices, based on the hybrid coupled equivalent magnetic circuit and magnetically coupled electric circuits, was described. The (MCEM)-(RNM) hybrid model reduce computation time with accuracy results, and take into account various geometry, the materials properties under multiple supply voltages. Therefore, the tool developed can be used in the optimal design of electromagnetic devices and also in the diagnosis area.

References

[1] J. Perho, Reluctance network for analyzing induction machines, D. thesis, University of Helsinki, 2002

[2] D. Petrichenko, Calculation and simulation of turbogenerators using permeance network. Optimization application, D. thesis, University of Lille, 2007

[3] B. Benali, Contribution à la modélisation des systèmes électrotechniques à l'aide des formulations en potentiels : application à la machine asynchrone, D. thesis, University of Lille, 1997

Analytical Modeling and Simulation of Self-excited Double Stator Induction Generator for Autonomous Operating Mode

1st Fatma Lounnas [1], 2nd Salah Haddad [2]

[1] *Mouloud Mammeri University of Tizi-Ouzou 1st author, Tizi-Ouzou, Algeria*

fat_lounas@yahoo.fr

[2] *Mouloud Mammeri University of Tizi-Ouzou 2nd author, Tizi-Ouzou, Algeria*

hddsalah@yahoo.fr

***Abstract*— This work is dedicated to the analytical modeling and simulation of a self-excited double-stator induction generator (SEDSIG). Based on the electrical and magnetic equations a model of the (SEDSIG) is developed under Matalb/Simulink environment.**

It is well known that in the self-excited induction machine, the linear model is divergent and saturation must be taken into account. In this paper the magnetic saturation is taken into account by considering the magnetizing inductance as a function of the magnetizing current. For this purpose, an experimental test bench was set up in our laboratory and the obtained variation curve of the magnetizing inductance as a function of the magnetizing current is approximated by a polynomial function.

Simulation results are presented and discussed.

Keywords*— *Analytical Modelingt, Self-excited Double Stator Induction Generator, Simulation, magnetic saturation).

I. INTRODUCTION

Wind energy is important because it is a clean and renewable resource that can be used to generate electricity. It helps reduce environmental pollution and dependence on fossil fuels.

A double stator induction generator (DSIG) offers other advantages over the traditional three-phase induction generator, such as power segmentation, rotor losses minimization, torque ripples and current harmonic reduction [1].

Several studies deal with the modelling of the dual stator induction generator. A detailed dynamic, steady state modeling and experimental analysis of a self-excited six phase induction generator have been discussed in [2,3]. In these works, shunt and series capacitors are utilized for excitation and voltage regulation. Analysis of an off-grid self-excited dual wound rotor asynchronous generator for wind power generation is presented in [4]. [5] focuses on the working modes of a multiphase induction machine, determining the static performance of the self-excited generator at no and under load conditions. In [6] complex vector modelling technique is utilized to develop and simulate a dual stator winding induction machine with squirrel-cage rotor.

In the literature, a variety of methods for modelling the double-stator induction machine has been proposed by several authors, in which they have taken into consideration the influence of the mutual leakage inductance between the two stators [7,8].

This work is dedicated to the modeling of the SEDSIG under Matalb/Simulink environment taking into account the saturation effect by means of a variable magnetic inductance as a function of the magnetic current.

The paper is organized as follows: Section II: Description and modeling of the (SEDSIG), Section III: Simulation results, Section IV: conclusion.

II. DESCRIPTION AND MODELING OF SELF EXCITED DOUBLE STATOR INDUCTION GENERATOR

The machine studied is a 1.1 kW squirrel-cage induction machine manufactured by the "Electro-Insudstries" company located in Azazga. The Fig. 1 gives the photo of this machine, the rotor is the classical squirrel cage type and two three phase windings are located in the stator. The scheme of the self-excited double stator induction generator with capacitors banks connected to the stators is shown in Fig.2.

Fig 1. Photo of a Double Stator Induction Machine

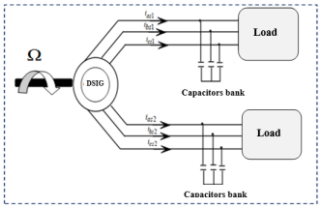

Fig 2. Scheme of SEDSIG

Voltage and flux equations characterizing the (SEDSIG) model in an arbitrary reference frame are given by:

Stator 1

$$\begin{cases} v_{ds1}=R_{s1}.i_{ds1}+\dfrac{d\varphi_{ds1}}{dt}-\dfrac{d\theta_{s1}}{dt}.\varphi_{qs1} \\ v_{qs1}=R_{s1}.i_{qs1}+\dfrac{d\varphi_{qs1}}{dt}+\dfrac{d\theta_{s1}}{dt}.\varphi_{ds1} \end{cases} \quad (1)$$

$$\begin{cases} \varphi_{ds1}=(L_{s1}+L_m)i_{ds1}+L_m(i_{ds2}+i_{dr}) \\ \varphi_{qs1}=(L_{s1}+L_m)i_{qs1}+L_m(i_{qs2}+i_{qr}) \end{cases} \quad (2)$$

Stator 2

$$\begin{cases} v_{ds2}=R_{s2}.i_{ds2}+\dfrac{d\varphi_{ds2}}{dt}-\dfrac{d\theta_{s2}}{dt}.\varphi_{qs2} \\ v_{qs2}=R_{s2}.i_{qs2}+\dfrac{d\varphi_{qs2}}{dt}+\dfrac{d\theta_{s2}}{dt}.\varphi_{ds2} \end{cases} \quad (3)$$

$$\begin{cases} \varphi_{ds2}=(L_{s2}+L_m)i_{ds2}+L_m(i_{ds1}+i_{dr}) \\ \varphi_{qs2}=(L_{s2}+L_m)i_{qs2}+L_m(i_{qs1}+i_{qr}) \end{cases} \quad (4)$$

Rotor

$$\begin{cases} v_{dr}=R_r.i_{dr}+\dfrac{d\varphi_{dr}}{dt}-\dfrac{d\theta_r}{dt}\varphi_{qr}=0 \\ v_{qr}=R_r.i_{qr}+\dfrac{d\varphi_{qr}}{dt}+\dfrac{d\theta_r}{dt}.\varphi_{dr}=0 \end{cases} \quad (5)$$

$$\begin{cases} \varphi_{dr}=(L_r+L_m)i_{dr}+L_m(i_{ds1}+i_{ds2}) \\ \varphi_{qr}=(L_r+L_m)i_{qr}+L_m(i_{qs1}+i_{qs2}) \end{cases} \quad (6)$$

The electromagnetic torque equation is given by:

$$C_{em}=p\frac{L_m}{L_r+L_m}\left[(i_{qs1}+i_{qs2})j_{dr}-(i_{ds1}+i_{ds2})j_{qr}\right] \quad (7)$$

The self-excitation of the two stator windings is described by the following equations:

$$\begin{cases} \dfrac{dv_{ds1}}{dt}=v_{qs1}.\dfrac{d\theta_{s1}}{dt}-\dfrac{1}{C_1}.i_{ds1} \\ \dfrac{dv_{qs1}}{dt}=-v_{ds1}.\dfrac{d\theta_{s1}}{dt}-\dfrac{1}{C_1}.i_{qs1} \end{cases} \quad \begin{cases} \dfrac{dv_{ds2}}{dt}=v_{qs2}.\dfrac{d\theta_{s2}}{dt}-\dfrac{1}{C_2}.i_{ds2} \\ \dfrac{dv_{qs2}}{dt}=-v_{ds2}.\dfrac{d\theta_{s2}}{dt}-\dfrac{1}{C2}.i_{qs2} \end{cases} \quad (8)$$

III. Simulation Results And Discussion

The simulation results of the linear model and the saturated one are respectively presented in figures (3,4) and (5,6).

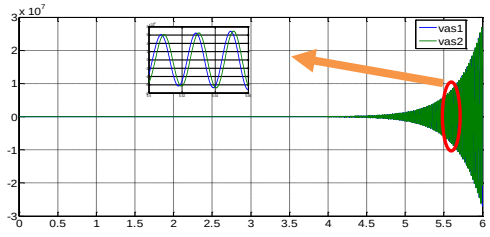

Fig 3. Stator 1 Stator 2 voltages evolution

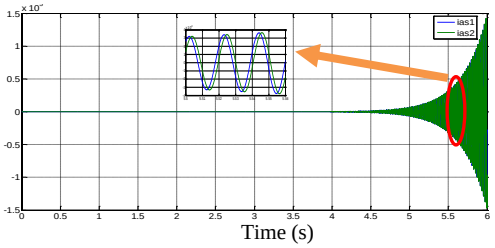

Fig 4. Stator 1 and Stator 2 currents evolution

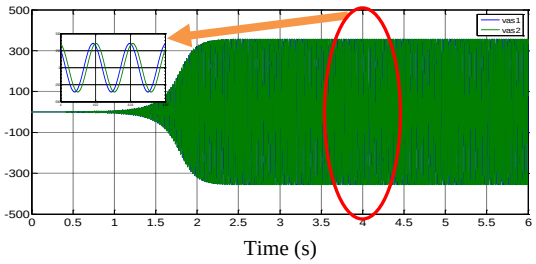

Fig 5. Evolution of stators voltages for N=1425 rpm and C_1= C_2=18μF

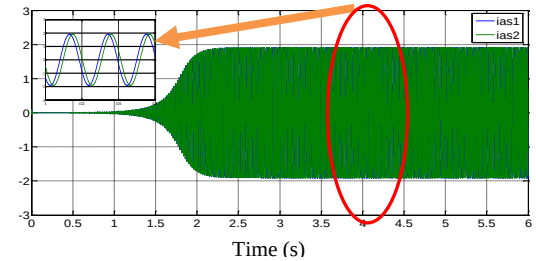

Fig 6. Evolution of stators currents for N=1425 rpm and C_1= C_2=18μF

IV. Conclusion

In this paper, an analytical model of self-excited double-stator induction generator (SEDSIG) is developed and implemented in Matlab/Simulink environment. The obtained results showed that the linear model is divergent. The consideration of the magnetic saturation is then obligatory. This is the most important characteristic of the self-excited induction generator, since it is the saturation itself wich sets the operating point.

References

[1] Amimeur, H., Abdessemed, R., Aouzellag, D., Merabet, E., & Hamoudi, F. (2010). A sliding mode control associated to the field-oriented control of dual-stator induction motor drives. *Journal of Electrical Engineering*, *10*(3), 7-12.

[2] Singh, G. K. (2008). Modeling and experimental analysis of a self-excited six-phase induction generator for stand-alone renewable energy generation. *Renewable energy*, *33*(7), 1605-1621.

[3] Chinmaya, K. A., & Singh, G. K. (2018). Performance evaluation of multiphase induction generator in stand-alone and grid-connected wind energy conversion system. *IET Renewable Power Generation*, *12*(7), 823-831.

[4] Khlifi, M. A. (2019). Analysis of an off-grid self-excited dual wound asynchronous generator for wind power generation. *International Journal of Advanced and Applied Sciences*, *6*(6), 35-42.

[5] Marwa, B. S., Larbi, K. M., Mouldi, B. F., & Habib, R. (2013, *March). Dual stator induction motor operation from two PWM* voltage source inverters. *In* 2013 *International Conference on Electrical Engineering and Software Applications (pp. 1-4). IEEE*.

[6] Ogunjuyigbe, A. S. O., Ayodele, T. R., & Adetokun, B. B. (2018). Modelling and analysis of dual stator-winding induction machine using complex vector approach. *Engineering Science and Technology, an International Journal*, *21*(3), 351-363.

[7] Amimeur, H., Abdessemed, R., & Merabet, E. (2008). Modeling and analysis of dual-stator windings self-excited induction generator. *Journal of Electrical Engineering*, *8*(3), 6-6.

[8] Wang, K., & Wu, X. (2022, May). Analysis of Self-excited Voltage Building of High-low Voltage Dual Stator-winding Induction Generator Considering Mutual Leakage Inductance. In *2022 IEEE 5th International Electrical and Energy Conference (CIEEC)* (pp. 1185-1189). IEEE.

L'influence de la densité de courant *Jc* sur le comportement magnetothermique de limiteur du courant de défaut superconducteur (SFCL)

Lotfi Alloui*, Khene Mohamed Lotfi, Mimoune Souri Mohamed, Benmebarek Fethi
Electrical Engineering and Industrial Electronics Laboratory (L2EI)
Département d'Electrotechnique Laboratoire de Modélisation des Systèmes Energétiques LMSE, Université de Biskra
Biskra, Algérie
*email :lotfi.alloui@univ-biskra.dz

Résumé-*Les limiteurs de courant de défaut supraconducteur SFCL sont principalement influencés par la densité du courant Jc. Dans cet article, nous exposons une étude numérique tridimensionnelle de limiteur de courant de défaut supraconducteur a haute température critique et l'impact de la densité du courant de la pastille supraconductrice sur le comportement électromagnétique et thermique du limiteur de courant de défaut supraconducteur. En utilisant la méthode des volumes finis (MVF), pour résoudre le problème numérique***)

Mots Clés- *Supraconducteur a haute température critique, Méthode des volumes finis, Limiteur de courant.*

I. INTRODUCTION

La demande d'énergie électrique augmente à la fois en termes de quantité et de qualité. Cela conduit à une augmentation de la puissance des équipements intégrés dans les réseaux et à l'expansion de la connectivité. L'augmentation significative de la puissance de court-circuit entraîne une difficulté accrue à contrôler les procédés de coupure des courants en cas de défaut. D'un autre côté, elle demande d'améliorer la sélectivité afin de ne sélectionner que les zones de défaut sans perturber le fonctionnement des zones restées saines.

Le principe de limitation de courant repose sur l'utilisation d'une impédance variable en série avec le réseau. Cependant, elle peut être à la fois résistive dans le cas des réseaux DC et inductive dans le cas des réseaux AC. La limitation du courant est due à une augmentation soudaine de l'impédance, qui doit être suffisamment rapide (moins de 1 ms) pour restreindre le premier pic de courant à une valeur seuil nettement inférieure à la valeur théorique de court-circuit. Lorsque le limiteur est en défaut, il est presque soumis à la pleine tension du réseau, ce qui entraîne une grande perte de puissance [1]. Les applications des supraconducteurs à haute température critique dans le domaine du génie électrique ne cessent d'augmenter depuis leur apparition. L'utilisation de ces matériaux dans le domaine de la réduction du courant de défaut dans les réseaux électriques est l'une des applications les plus prometteuses. Grâce à leur invisibilité dans le régime assigné ou nominal (résistance nulle), ces limiteurs présentent l'avantage de pouvoir restreindre les courants de défaut dans un temps de réponse très court par rapport aux limiteurs de courant classiques ou aux disjoncteurs traditionnels. La détermination précise des grandeurs électromagnétiques et thermiques est indispensable pour une telle application. Les résultats des simulations des comportements magnétique-thermique de limiteur de courant supraconducteur obtenus à partir de code numérique développé et mis en œuvre sous l'environnement MATLAB sont présentés dans cet article. Nous avons utilisé la méthode des volumes finis pour résoudre l'ensemble des équations aux drivées partielles spécifiques aux phénomènes physiques à traiter [2] [3].

II. MODELE NUMERIQUE

Il est essentiel de simuler le comportement magnétique et thermique d'un limiteur de courant supraconducteur après l'application d'un courant de défaut alternatif. Pour résoudre le problème électromagnétique, nous avons employé une formulation électromagnétique en trois dimensions (3D) en *A-V* donnée par [4-5-6-7] :

$$\nabla\times(\nu_0\nabla\times\boldsymbol{A})-\nabla(\nu_0\nabla.\boldsymbol{A})+\sigma(\boldsymbol{E},\boldsymbol{B},T)\left(\frac{\partial\boldsymbol{A}}{\partial t}+\nabla V\right)=\boldsymbol{J_s} \quad (1)$$

$$\nabla.\left(\sigma(\boldsymbol{E},\boldsymbol{B},T)\left(\frac{\partial\boldsymbol{A}}{\partial t}+\nabla V\right)\right)=0 \quad (2)$$

Il est essentiel de résoudre le problème thermique afin de déterminer tous les paramètres $\boldsymbol{\sigma}$, $\boldsymbol{E}$ et $\boldsymbol{J}$. Pour cela, nous avons employé l'équation de diffusion thermique [5]:

$$\rho.C_P\frac{\partial T}{\partial t}-\nabla.(\kappa.\nabla T)=P \quad (3)$$

La résolution des équations 1, 2 et 3 permet de résoudre les problèmes liés à l'électromagnétisme et à la chaleur. Les équations qui les définissent sont très non linéaires. Pour la résolution numérique du problème mathématique mentionné précédemment et qui se distingue par une problématique fortement non linéaire, notamment la loi apparente de la conductivité électrique, nous suggérons d'utiliser le MVF afin d'assurer une convergence accrue. Effectivement, plusieurs recherches ont démontré que les approches numériques conservatrices permettent d'éviter les oscillations numériques [5-6-7]. Afin d'éviter le problème de convergence, nous avons employé la méthode du volume fini dans sa version tridimensionnelle [5]. Le système d'équations différentielles sur chaque volume de contrôle v_e. les résultats issus de la mise en ouvre de la MVF peuvent - être trouvés dans [7-8-9]

III. LES PARAMTRES DE SIMULATION

Le principe fondamental du limiteur de courant supraconducteur SFCL repose sur les caractéristiques de matériaux supraconducteur de type YBaCuO avec une température critique Tc est égale a 92 °K. Le modèle de la

pastille est présenté dans la fig. 3. La pastille de type rectangulaire (4×4×4 mm^3).

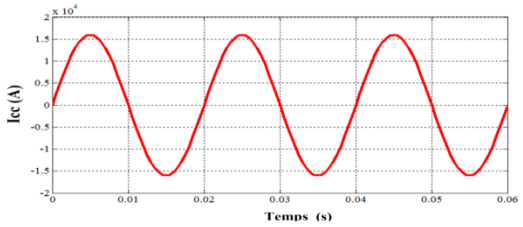

Fig. 1. L'allure du courant de court-circuit appliqué.

IV. RESULTATS ET INTERPRETATION

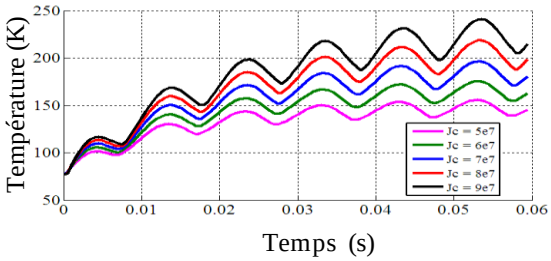

Fig. 2. La variation de température pour les différentes valeurs de ***Jc*** (5, 6, 7, 8 et 9 ×10^7 A/m^2).

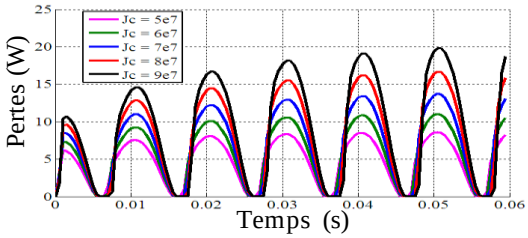

Fig.3. Variation des pertes pour les différentes valeurs de ***Jc*** (5, 6, 7, 8 et 9 ×10^7 A/m^2).

D'après les données exposées (Fig. 4 et 5), il est évident que lorsque la densité du courant ***Jc*** augmente, la température au sein de la pastille supraconductrice augmente de manière significative, principalement en raison de

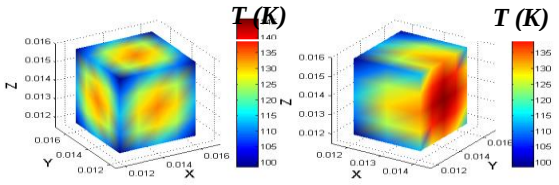

Fig. 4 : Répartition spatiale de la température au sein de la pastille supraconductrice pour ***Jc = 5×10^7 A/m^2***.

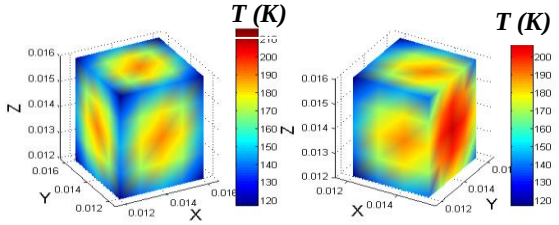

Fig. 5 : Répartition spatiale de la température au sein de la pastille supraconductrice pour ***Jc = 9×10^7 A/m^2***.

Les figures (6 et 7) représentent la répartition spatiale de la température au sein de la pastille supraconductrice en 3D respectivement pour la valeur de $Jc = 5\times10^7 A/m^2$ et $Jc = 9\times10^7 A/m^2$. Selon les résultats présentés, on peut dire que la température se répartie d'une manière non homogène à l'intérieur de la pastille supraconductrice, en effet, la température au centre de la pastille supraconductrice est plus élevée. Les surfaces extrêmes de la pastille supraconductrice sont les plus froides. Ceci est due principalement à l'effet de transfert de chaleur entre du fluide cryogénique et la pastille supraconductrice très renforcé aux nivaux des surfaces.

V. CONCLUSION

Une étude a été menée après plusieurs simulations afin d'analyser le temps de transition, les pertes et la répartition de la température dans le limiteur du courant supraconducteur. Les résultats des simulations exposées ont démontré l'impact de la valeur du courant critique *Jc* sur le comportement magnétothermique du limiteur du courant supraconducteur SFCL, ainsi que sur le temps de transition de l'état supraconducteur vers un état normal appelé temps de réponse du limiteur SFCL.

REFERENCES

[1] YANNICK COINTE. " Limiteur supraconducteur de courant continu " Thèse de doctorat de l'Institut National Polytechnique de Grenoble, 2007.

[2] S. BELKHIRI, L. ALLOUI, F. BENMEBAREK, L. KHENE, et S.M. MIMOUNE " MODELISATION DES PHENOMENES ELECTROMAGNETIQUE ET THERMIQUE D'UN LIMITEUR DE COURANT SUPRACONDUCTEUR DE SECONDE GENERATION ", Courrier du Savoir – N°23, pp.161-166, 2017.

[3] S. BELKHIRI, L. ALLOUI, et F. BENMEBAREK, " The Influence of the Geometrical Properties of Bulk Superconductors on Limiting Fault Current in an Electrical Network ", Advanced Electromagnetics, Vol. 8 No. 4, (2019).

[4] J. Clerk Maxwell, A Treatise on Electricity and Magnetism, 3rd ed., vol. 2. Oxford: Clarendon, 1892, pp.68–73.

[5] L. Alloui, F. Bouillault and S.M. Mimoune, 'Numerical study of the influence of flux creep and of thermal effect on dynamic behaviour of magnetic levitation systems with a high-Tc superconductor using control volume method,' Eur. Phys. J. Appl. Phys. 45, 20801. 2009.

[6] L. Alloui, M. L. Khene, A. Kameni, F. Bouillault, S. M. Mimoune and M. Feliachi,'Analysis of Trapped Magnetic Field During Magnetization Process by Using SPA Method of Bulk Superconductor,'. IEEE TRANSACTIONS ON MAGNETICS, VOL. 51, NO. 3, 2015.

[7] L. M. Khene, L. Alloui, F. Benmebarek, S. M. Mimoune, '3D Simulation of the influence of the external magnetic field on superconducting permanent magnets'. Physica C, Superconductivity and its applications 609. 2023.

[8] F. Benmebarek, L. Alloui, L.M. Khene, A. Kameni, H. Becha, T. Azib, S.M. Mimoune, '3D modeling of magneto-thermal phenomena in superconductors with defects', Physica C: Superconductivity and its Applications, Volume 613, 2023.

[9] L. ALLOUI, K. BEN ALIA, F. BOUILLAULT, S.M. MIMOUNE, L. BERNARD et J. LEVEQUE, " Numerical study of the relation between the thermal effect and the stability of the levitation system excited by an external source '', Physica C 487 (2013) 1–10.

Session 5 (Orale):

Magnetic Material Modeling and Applications

- Modeling of asymmetrical minor hysteresis loops using the Jiles-Atherton hysteresis model
- Information transport in ferromagnetic materials having cubic crystallizations
- Effet de la Non-Linéarité Magnétique sur l'Évaluation de l'Impédance d'un Dispositif CND
- Influence of Magnetic Field on Spin waves Dispersion in Ferromagnetic Multilayers

Modeling of asymmetrical minor hysteresis loops using the Jiles-Atherton hysteresis model

Bachir SELMOUNE [1], Mourad HAMIMID [1], Souri Mohamed MIMOUNE [2], Sofiane AIDEL [1]

[1]*LPMRN Laboratory, University Mohamed El Bachir El Ibrahimi of Bordj Bou Arreridj,34000 BBA, Algeria*
[2]*Laboratoire de Modélisation des Systèmes Energétiques LMSE, Université de Biskra, BP 145, 07000 Biskra, Alegria*

***Abstract*- This research presents an enhanced analysis of the Jiles-Atherton model, particularly under harmonic excitation. It emphasizes the anhysteretic magnetization's dependence on two primary parameters: the mean field parameter (α) and the shape parameter (a). The study introduces a novel representation for these parameters to correct the non-physical depiction of asymmetrical minor hysteresis loops in the original model. These parameters are redefined through functions linked to the major loop's reversible and saturation induction. An optimization process is employed to align the model with empirical data, ensuring minor loops are accurately represented using the new parameters, with validation showing a strong correlation between simulation and measurements.**

Keywords— Jiles-Atherton model, Harmonics, Optimization, Anhysteretic magnetization, Asymmetrical minor loops.

I. INTRODUCTION

The J-A model is a famous model in the literature for describing hysteresis phenomena, and its usefulness has been validated in different conditions [1]. This study addresses a solution to a problem frequently referenced by researchers, particularly in relation to the J-A model's asymmetrical minor hysteresis loops [2–7]. The J-A model does not provide an adequate response if the waveform of the magnetic flux density (*B*) is non-sinusoidal, as opposed to its response when B is entirely sinusoidal. This results in a non-physical behavior where the asymmetrical minor hysteresis loop does not close [3, 4]. Several researchers have proposed adjustments to the J-A model to address this difficulty. For instance, researchers suggested modifying the four parameters of the model (a, α, c, and k) to improve the asymmetrical minor loops [3]. Another proposed adjustment of the parameters 'c' and 'k' based on the variation of the magnetic field yields acceptable results [4]. A further proposal involved adding a new multiplier to the irreversible magnetization (M_{irr}), effectively limiting the rate of variation of the irreversible magnetization. This limitation is achieved by introducing a parameter R, which is also linked to losses and associated with the irreversible component [7]. The J-A model primarily depends on anhysteretic magnetization [1]. The physical solution to this phenomenon involves altering the anhysteretic magnetization to improve the model's response. Given that the handiest way to modify the anhysteretic magnetization is by modifying its coefficients (*a, α*, and *Ms*), and considering that the saturation magnetization (*Ms*) is constant, only two parameters (*a, α*) want to be evaluated for the minor loops because of their direct dating with anhysteretic magnetization.

II. THE MODIFIED INVERSE JILES – ATHERTON MODEL

The following equation describes the inverse Jiles-Atherton hysteresis model (IJ-A) [10]:

$$\frac{dM}{dB}=\frac{K\delta c\dfrac{dM_{an}}{dH_e}+\left(M_{an}-M\right)}{\mu_0\left(K\delta+\left(1-\alpha\right)\left(K\delta c\dfrac{dM_{an}}{dH_e}+\left(M_{an}-M\right)\right)\right)} \tag{1}$$

Where the effective field

$$H_e=H+\alpha M \tag{2}$$

The Anhysteretic magnetizations [8, 9] is given by

$$M_{an}=Ms\left(\coth\frac{H_e}{a}-\frac{a}{H_e}\right) \tag{3}$$

In the current study, we conducted calculations using non-oriented magnetic sheets composed of 3% Fe-Si, featuring laminations with a thickness of 0.5 mm. The experimental results were obtained by utilizing an Epstein frame [4, 5]. The calculations were performed using the IJ-A model, and the five model parameters (Table I) were obtained through an optimization procedure.

TABLE I. PARAMETERS OF THE MODEL UNDER SINUSOIDAL WAVE-FORM FLUX DENSITY

Value	Parameters of model
$1.48\cdot10^{6}$	*Ms. (A/m)*
71.33	*a (A/m)*
65.5	*k (A/m)*
$1.47\cdot10^{-4}$	*α*
0.316	*c*

It is important to note that the measured data was removed from the reference [5] using the program MATLAB® called GRABIT. The simulation of the major hysteresis loop aligns well with the actual measurements. However, the minor loops do not match the measured ones in Fig 1 and lack physical significance. The introduction of third and fifth harmonics in the flux density waveform produces four asymmetrical minor loops on the major loop, with two on the edges and two in the middle, detailed in the next figure.

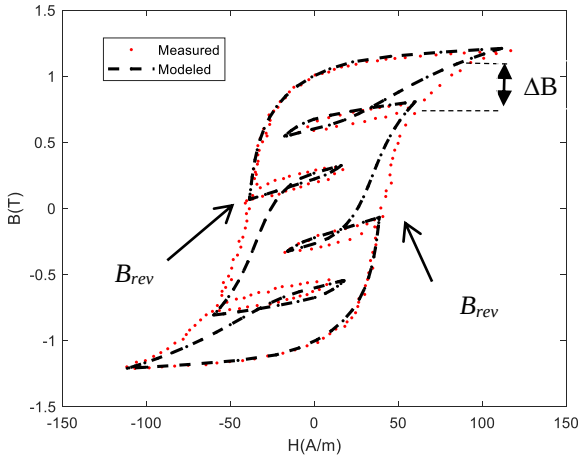

Fig. 1 Modeled and measured hysteresis loops with the original J-A model under the waveform of flux density with harmonics

III. ASYMMETRICAL MINOR HYSTERESIS LOOPS MODEL

In the study of asymmetrical minor hysteresis loops, the primary parameters that affect these loops are 'a' and 'α'. This research achieves a modification of the anhysteretic magnetization by adjusting these parameters. They are connected to the major loop parameters, and the relationship involves calculating the ratio of the reverse flux density B_{rev} for the minor loop to the saturation flux density B_{sat} of the major hysteresis loop.

$$\begin{cases} a_{min} = a_{maj}\left(B_{rev}/B_{sat}\right)^{\gamma} \\ \alpha_{min} = \alpha_{maj}\left(B_{rev}/B_{sat}\right)^{\beta} \end{cases} \quad (4)$$

Parameters $a_{\min}$ and $\alpha_{\min}$ pertain to minor loops, a_{maj} and α_{maj} to major loops. Coefficients γ and β result from optimization process, Table 2.

TABLE II. THE OPTIMIZED COEFFICIENTS.

Parameters	In 3rd harmonic	In 5th harmonic
γ	0.6	-0.76
β	- 0.15	-0.73

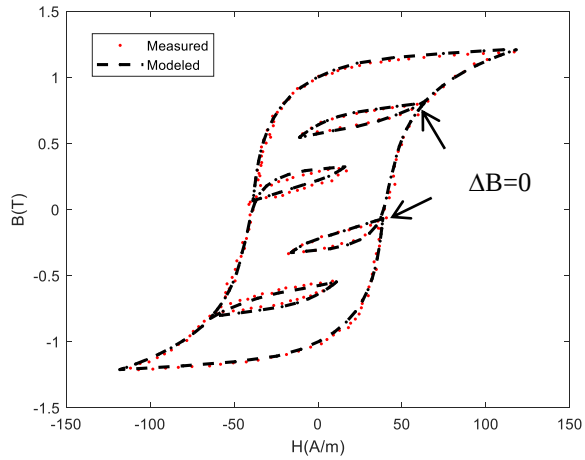

Fig.2 Modeled and measured hysteresis loops with the modified J-A model under the waveform of flux density with harmonics

In the Fig 2, we observe that the minor loops are fully closed. By employing just two Eq (4), our modeled hysteresis loop effectively simulates the measured loops both inside and outside the asymmetrical minor hysteresis loops. Notably, this new model remains robust even in scenarios involving harmonics in the excitation

CONCLUSION

In this study, we propose a precise assessment method for asymmetrical hysteresis minor loops by manipulating the anhysteretic magnetization parameters. The fundamental concept hinges on recalibrating these parameters using novel expressions, which take into account the ratio between saturation flux density and reverse flux density. Specifically, this adjustment is selectively applied to the ascending and descending branches of the asymmetrical minor hysteresis loops, while maintaining consistency with the parameters of the major loop beyond these minor loops. Our results demonstrate remarkable agreement with measured data, validating the efficacy of our modified model. By refining our understanding of hysteresis behavior, this approach contributes to the broader field of magnetic materials research.

REFERENCES

[1] D. C. Jiles and D. L. Atherton, "Theory of ferromagnetic hysteresis," *J. Magn. Magn. Mater.*, vol. 61, no. 1-2, pp. 48-60, 1986.

[2] Atyia, A. H. S., & Ghanim, A. M., "Limitations of Jiles–Atherton models to study the effect of hysteresis in electrical steels under different excitation regimes," *COMPEL-The international journal for computation and mathematics in electrical and electronic engineering*, vol. 43, no. 1, pp. 66-79, 2024.

[3] M. Hamimid, S. M. Mimoune, M. Feliachi, and K. Atallah, "Non centered minor hysteresis loops evaluation based on exponential parameters transforms of the modified inverse Jiles–Atherton model," in *Physica B: Condensed Matter*, vol. 451, pp. 16-19, 2014.

[4] A. Benabou, J. V. Leite, S. Clénet, C. Simão, and N. Sadowski, "Minor loops modelling with a modified Jiles–Atherton model and comparison with the Preisach model," in *J. Magn. Magn. Mater.*, vol. 320, no. 20, pp. e1034-e1038, 2008.

[5] J. V. Leite, N. Sadowski, P. Kuo-Peng, and A. Benabou, "Minor loops calculation with a modified Jiles-Atherton hysteresis model," *Journal of Microwaves, Optoelectronics and Electromagnetic Applications (JMOe)*, vol. 8, no. 1, pp. 49S-55S, June 2009.

[6] Mohan Unniachanparambil, G., & Kulkarni, S. V., "Use of a scaling power law to incorporate asymmetrical minor loops in the inverse Jiles–Atherton model," *IET Electric Power Applications*, vol. 13, no. 12, pp. 2090-2095, 2019.

[7] J. V. Leite, A. Benabou, and N. Sadowski, "Accurate minor loops calculation with a modified Jiles-Atherton hysteresis model," *COMPEL-The international journal for computation and mathematics in electrical and electronic engineering*, vol. 28, no. 3, pp. 741-749, 2009.

[8] B. Selmoune and M. Hamimid, "Anhysteretic Magnetization Effect on the Centered and Non-Centered Minor Hysteresis Loops in Jiles-Atherton Model," *Instrumentation, Mesures, Metrologies*, vol. 20, no. 6, 2021.

[9] Martin, F., Chen, R., Taurines, J., & Belahcen, A., "Anisotropic hysteresis representation of steel sheets based on a vectorization technique applied to Jiles-Atherton model," *IEEE Transactions on Magnetics*, 2023.

[10] Y. Liu, H. Zhang, S. Liu, and F. Lin, "Modeling analysis of pulsed magnetization process of magnetic core based on inverse Jiles-Atherton model," *Review of Scientific Instruments*, vol. 89, no. 5, May 2018

Information transport in ferromagnetic materials having cubic crystallizations

Rebiha Challali
Laboratory of physics and quantum chemistry
Mouloud Mammeri University
Tizi-Ouzou, Algeria
rebiha.challali@ummto.dz

Boualem Bourahla
Laboratory of physics and quantum chemistry
Mouloud Mammeri University
Tizi-Ouzou, Algeria
boualem.bourahla@ummto.dz

Abstract**—** *The information transport across the ferromagnetic interface in the solid medium can be determined by knowing the behavior of spin waves. For modelling, we consider a model system resulting from the juxtaposition of two cubic structures with different mesh sizes. We study the magnetic interface sc/bcc (simple cubic/body centered cubic) and its inverse bcc/sc.*
The magnetic transport and diffusion phenomena of spin waves across the interface, which are the magnetic excitations that collectively propagate through the interface, are the subject of our analysis. The transmission and reflection coefficients of the magnon are calculated as the elements of a Landauer-type scattering matrix, using the matching method. The numerical simulations are carried out specifically for three different cases of magnetic exchange on the interface's own domain. The influence of softening, homogeneity and hardening of the magnetic coupling in this domain on the magnonic transmittance across the sc/bcc and bcc/sc interfaces has been observed.
Keywords**—***Spin waves, Magnonic transmittance, ferromagnetic interface*

I. INTRODUCTION

Information and communication technology continues to revolutionize the world. Relying on electronic devices made from semi-conductors that use electric charge current to operate. Spintronic devices, on the other hand, rely on the concepts of spin current for information processing and storage. These devices suffer from the phenomenon of multiple electron diffusion, which means that the electronic spins are not systematically conserved. Magnonic devices, also known as spin wave devices *(SWDs)*, are therefore been identified as an alternative to these technologies. They work with the concept of magnetic spin transport. The great advantage of using *SWDs* to transport and process information lies in the exploitation of their magnetic properties. In fact, their operation is based on the use of collective spin oscillations *(Spin Waves)*, which enable them to limit electronic scattering processes due to collisions between electrons, impurities and structural defects on the one hand, and to reduce leakage currents due to quantum phenomena on the other. They are very good competitors to *CMOS (Complementary Metal Oxide Semiconductor)* technologies [1]. They have the ability to achieve long spin diffusion wavelengths, opening the way for research into fully reprogrammable logic devices. However, scientists are increasingly focusing on miniaturizing electronic components by synthesizing thin films and multilayers in ultra-high vacuum. The physical, electrical and magnetic properties of these nano-scale structures differ from those of conventionally sized materials. The difference lies at the interfaces [2], where interesting physical phenomena occur [3], such as the appearance of Fano resonances in the transmittance spectra of spin waves. Selective transmission of information as a function of the propagation frequency of these waves is then observed and can be controlled and directed as required, simply by controlling the way in which the nanostructures are assembled. In this communication, we propose to study information transmission by calculating the transmission and reflection coefficients of spin waves propagating in magnonic devices, with interfaces connecting ferromagnetic cubic structures with different meshes.

II. MODEL DESCRIPTION

We have simulated and analyzed the information transport through the phenomenon of spin wave scattering across the ferromagnetic interface. To model an interface, we consider the juxtaposition of two semi-infinite subsystems A and B, of cubic crystallization and ferromagnetic order. The lattice parameters of the two crystals are assumed to be very close ($a_A = a_B = a$) and all spin moments, in the ground state, have the same orientation and the same absolute value S on each atom of the two sub-lattices. The system analyzed is free from any type of interaction with its environment. Note that the incident spin wave follows the [100] direction. As we will see, the direction of incidence plays a major role in scattering and localization phenomena so it is important to consider the direction of incidence when crossing the mesh. This leads us to consider the *sc/bcc* and *bcc/sc* interfaces differently.

III. INFORMATION TRANSPORT THROUGH THE FERROMAGNETIC INTERFACE

A. Propagation of Spin Waves in Perfect Cubic Structure

The precessional motion of a spin vector, located on an atomic site of a perfect system *bcc* or *sc* (before and after of the interface region) is described by the Heisenberg Hamiltonian [4], which describes all the interactions between the spin vectors. It is given by:

$$H = -2\sum_{p\neq \acute{p}} J_{p\acute{p}}.\overrightarrow{S_p}.\overrightarrow{S_{\acute{p}}} \qquad (1)$$

where $\overrightarrow{S_p}(\overrightarrow{S_{\acute{p}}})$ are spin vectors located in $p(\acute{p})$ sites. The magnetic exchange constant $J_{p\acute{p}}$ couples adjacent sites $p(\acute{p})$ of the system. The exchange constants between spins in the *bcc* structure are denoted by J_B, those in the *sc* structure are denoted by J_A and those between the two contacting layers (at the interface) are denoted by J_d. Using the matching method [5], the precessional motion equations of spins that are far from the interface zone can be put into the matrix form as an eigenvalue problem:

$$\left[\Omega I - D_v(\varphi_x, \varphi_y, \xi)\right] |C>= 0 \qquad (2)$$

Where Ω is the dimensionless normalized frequency, D_v is called the matrix dynamic of the perfect lattice, φ_x, φ_y and ξ

are the phase factors in the Ox, Oy and Oz directions respectively. I denotes the identity matrix and $|C>$ are the spin vectors. The propagating and evanescent spin modes are described by the doublet $\{\xi, \xi^{-1}\}$. The curve giving the group velocity at which the wave packet moves from the *sc* system to the *bcc* system is shown in Fig. 1(a) and from the *bcc* system to the *sc* system in Fig. 1(b). The velocity is non-zero over the frequency interval [0, 7.2], corresponding to the displacement range of the propagating modes of the *sc* perfect system, and [0, 16], for the *bcc* perfect system.

B. *Spin Waves Scattering Across the Ferromagnetic Interface*

To describe the magnonic diffusion, we use all the solutions of the system corresponding to $|\xi| \leq 1$. These solutions are obtained by Gagel's method [6], which consists in linearizing the equations of motion by increasing the eigenvector basis of the original system. A magnon incident on the ferromagnetic interface zone scatters into two parts: one transmitted and the other reflected. The precessional fields generated can be expressed as a combination of the eigenmodes of the semi-infinite system. We have the following expressions:

$$r = r_{\nu\bar{\nu}} = \frac{V_{g\nu}}{V_{g\bar{\nu}}} |R_{\nu\bar{\nu}}|^2 \quad (3)$$

$$t = t_{\nu\bar{\nu}} = \frac{V_{g\nu}}{V_{g\bar{\nu}}} |T_{\nu\bar{\nu}}|^2 \quad (4)$$

$r_{\nu\bar{\nu}}$ and $t_{\nu\bar{\nu}}$ are the reflection and transmission coefficients previously normalized by the group velocities (V_{g_ν}, $V_{g_{\bar{\nu}}}$) of the plane wave, ν is the propagating mode, and $\bar{\nu}$ is the incident mode. $R_{\nu\bar{\nu}}$ and $T_{\nu\bar{\nu}}$ are respectively the probabilities of the magnon reflection and transmission respectively.

By isolating the terms describing the wave incident on the spins of the two lattices *bcc* and *sc* at the boundaries (before and after the interface) using relation (2), the system of linear and inhomogeneous equations takes the matrix form [2]:

$$\left[D\left(J_d, J_A, J_B, \varphi_x, \varphi_y, \xi\right)\right][D_R]\vec{X} = -D\left(J_d, J_A, J_B, \varphi_x, \varphi_y, \xi\right).\vec{V}_{in} \quad (5)$$

D is the dynamic matrix of the domain containing the interface, $[D_R]$ is the matching matrix, $\vec{V}_{in}$ is the incident vector and $\vec{X}$ is a vector that groups together the unknown variables of the interface lattices.

To solve the system of equations (5), we use the matching method [5]. We can determine the transported information by magnon mode for any incident energy [7].

Numerical results for magnon scattering across the *sc/bcc* and *bcc/sc* interface for the possibilities of exchange integral values are shown in Fig. 2, taking into account only first-near-neighbor interactions. In each case $J_d = (J_A + J_B)/2$. Case (a) refers to softening interactions with $J_d = 0.9$, case (b) refers to homogeneity interactions with $J_d = 1.0$ and case (c) refers to hardening interactions with $J_d = 1.1$.

Note that any scattering of the wave across the interface joining the *sc* lattice to the *bcc* lattice, is felt by a large narrowing of the scattering range of the signal ($\Omega \in [0, 4]$ instead of the interval [0, 7.2]). In addition, we see the appearance of resonance peaks as the signal propagates from *bcc* to *sc* (see Fig 1. Magnonic Transmittance). Note that these resonances do not exist when the spin wave travels in the opposite direction through the interface. This point plays an important role and depends on the subsystem in which the wave is incident.

In conclusion, the two models that allow the simulation of coherent diffusion and the magnonic transport across the interface between the *sc* and *bcc* structures can be used to amplify or filter certain spin bands. Our analysis can be applied to the study of magnetic interface properties in multilayer systems. The transmission spectra also demonstrate the role of crystallization on the dynamics of the nano-junction zone. It can also serve as a model for the study of other magnetic materials constructed in the same way as the system under study.

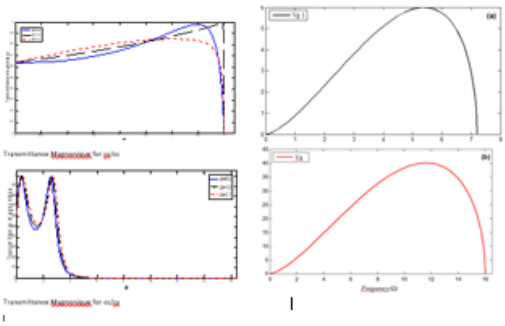

Fig .1. Group Velocity of *sc* (a) and *bcc* (b) perfect systems and Magnonic Transmittance

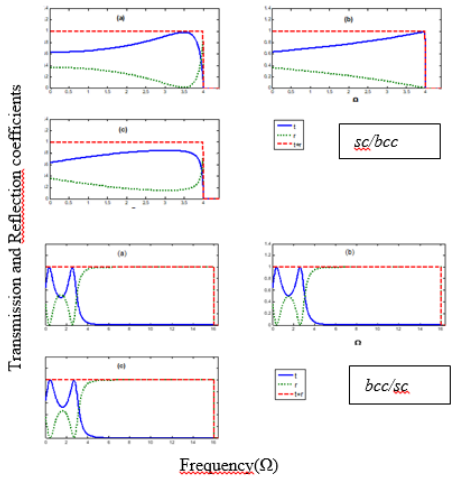

Fig 2. Transmission and reflection spectrum.

REFERENCES

[1] T. Schefer, J. Robert, M. Bailleul and M. Kostylev, J. Magn. Magn. Mat. 565, 170002 (2023).
[2] L. Ferrah, B. Bourahla and S. Blizak, Spin11,2150028 (2021).
[3] B. Bourahla, A.Khater, M. Abou Ghantous, Eur. Phys. J.Web Conf. 29, 00011 (2012).
[4] D. Ghader and A. Khater, J. Phys. Condens. Matter 31, 315801 (2019).
[5] R.Challali, S. Sait, B. Bourahla and L. Ferrah. Spin 12, 2350001 (2023).
[6] C. Berthod, F. Gagel and K. Maschke, Phys. Rev B 50, 18299 (1994).
[7] L. Djebala and B. Bourahla, Spin 11, 2150066 (2021).

Effet de la Non-Linearité Magnétique sur l'Évaluation de l'Impédance d'un Dispositif CND

Mehaddene Hamid
dept.Electrotechnique
Université Mouloud Mammeri
Tizi-Ouzou, Algérie
mehaddenehamid@yahoo.com

Mohellebi Hassane
dept. Electrotechnique
Université Mouloud Mammeri
Tizi-Ouzou, Algérie
hass.2000@yahoo.com

***Résumé*— L'objectif de ce travail est de présenter une méthode basée sur la méthode des éléments finis pour prendre en compte la non-linéarité des matériaux ferromagnétiques lors de l'analyse en contrôles non destructifs par courants de Foucault. L'étude du problème a été réalisée en exploitant un programme de calcul par éléments finis mis en œuvre sous environnement Matlab pour la résolution de l'équation magnétodynamique 2D. Un modèle analytique décrivant le comportement non linéaire de l'aimantation M(H) d'un acier ferromagnétique a été intégré. Les résultats de la simulation numérique obtenus sont comparés aux résultats issus de l'expérimentation.**

Mots-clés -- Contrôle non destructif, Courants de Foucault, Non-linéarité, Acier ferromagnétique.

I. INTRODUCTION

Dans la littérature scientifique, la plupart des modèles physiques régissant les problèmes de contrôle non destructifs (CND) par courants de Foucault (EC) des matériaux magnétiques considèrent la théorie linéaire de l'électromagnétisme (perméabilité magnétique relative constante). Cependant, les problèmes d'inspections réels impliquent souvent des comportements non linéaires, dans le cas d'un échantillon de pièce en aciers ferromagnétiques où les signaux de contrôle non destructif par courants de Foucault présentent inévitablement des réponses non linéaires [1].

Il est bien connu que les signaux d'impédance collectés par les instruments à courants de Foucault (EC) présentent des comportements non linéaires lorsqu'ils sont appliqués à des échantillons ferromagnétiques. La manifestation la plus courante de la non-linéarité est que le signal d'impédance devient dépendant de l'intensité du champ magnétique d'excitation (H_{exc}). Un échantillon ferromagnétique peut transformer l'impédance (Z) en une quantité dépendante de la densité de courant (J_s) grâce à sa réponse non linéaire au champ d'excitation (H_{exc}) [2, 3].

C'est pourquoi il est nécessaire de prendre en compte cette caractéristique afin de décrire de manière adéquate ces phénomènes.

II. MODÉLE ANALYTIQUE DE L'AIMANTATION

Pour prendre en compte la non-linéarité, un modèle analytique décrivant le comportement non-linéaire de l'aimantation M(H) d'une tôle ferromagnétique est utilisé afin d'evaluer la perméabilite magnétique variable [4] :

$$M(H_{exc}) = H_{exc} + C_1 * arctg(C_2 * H_{exc}) \quad (1)$$

$$C_1 = \frac{2}{\pi} M_{sat} \quad (2)$$

$$C_2 = \frac{\mu_{ri}-1}{C_1} \quad (3)$$

$H_{exc}, \mu_0, M_{sat} et \mu_{ri}$, représentent respectivement le champ magnétique d'excitation, la perméabilité magnétique du vide, l'aimantation à saturation et la perméabilité magnétique relative initiale.

Les valeurs du champ magnétique d'excitation (H_{exc}) sont issues de l'expérience pour un acier ferromagnétique (AISI 430) et sont données par la figure ci-dessous.

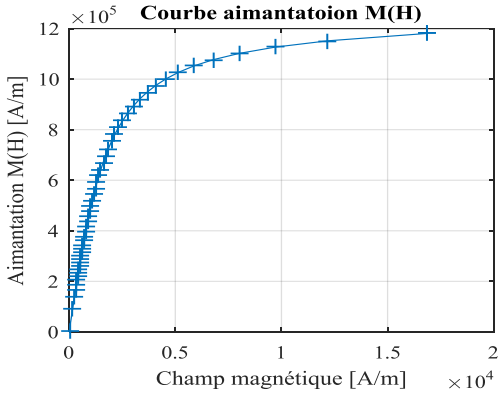

Fig. 1. Courbe M(H) de l'acier ferromagnétique AISI430.

Si l'état initial du matériau est démagnétisé, la loi de comportement M(H_{exc}) décrira la courbe de première aimantation au fur et à mesure que le champ H_{exc} augmente. On remarque qu'au-delà d'un certain champ d'excitation, l'aimantation varie très peu et tend asymptotiquement vers une valeur d'aimantation à saturation M_{sat}.

Pour valider le modèle analytique décrivant le comportement non linéaire de l'aimantation M(H) de l'acier ferromagnétique AISI430, les résultats du modèle analytique sont comparés aux données expérimentales et sont montrés sur la figure-2.

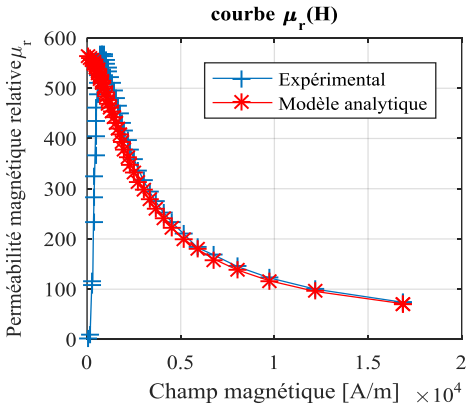

Fig. 2. Courbe μ_r(H) de l'acier ferromagnétique AISI430.

III. APPROCHE ET RESULTATS

L'équation aux dérivées partielles (EDP) qui décrit les phénomènes électromagnétiques des dispositifs CND-CF est obtenue à partir de la combinaison des équations de Maxwell et des relations du milieu, en terme du potentiel vecteur magnétique A_z, sous la forme harmonique suivante:

$$-\frac{\partial}{\partial x}\left(\frac{1}{\mu(H)}\frac{\partial A_z}{\partial x}\right)-\frac{\partial}{\partial y}\left(\frac{1}{\mu(H)}\frac{\partial A_z}{\partial y}\right)+j\sigma\omega A_z = J_{sz}(H_{exc}) \quad (4)$$

J_{sz} est la densité de courant d'excitation, σ est la conductivité électrique et $\mu(H)$ est la perméabilité magnétique variable.

La résolution de (4) fait intervenir les relations :

$$B(H_{exc}) = \mu_0 * \left(H_{exc} + M(H_{exc})\right) \quad (5)$$

$$\vec{B} = \overrightarrow{rot}\, A \quad (6)$$

Dans le cas de matériaux ferromagnétiques, à forte aimantation, la courbe B(H_{exc}) est non linéaire. Dans ce travail cette non-linéarité est prise en compte par un processus itératif dans lequel: partant d'une valeur initiale du champ magnétique d'excitation (H_{exc}) puis le processus itératif est exécuté jusqu'à ce que le système converge.

L'algorithme de résolution utilisé peut être résumé comme suit :

1- Calcul de la perméabilité magnétique relative à partir d'un modèle analytique de calcul de l'aimantation issu de la littérature Eq (1).

2- Injecter cette perméabilité magnétique relative dans le code de calcul par éléments finis Eq (4).

3- Déduire le champ magnétique H_{EF} en utilisant la relation du milieu.

4- Teste du champ (H_{exc}) initial injecté dans le modèle avec le champ (H_{EF}) calculé jusqu' à convergence.

5- Calcul de l'impédance pour chaque valeur du champ d'excitation (H_{exc}) avec les relations suivantes [1]:

$$Re(Z) = -\frac{N^2\omega}{J_{sz}(H_{exc})S^2}\iint_s 2\pi r I_m(A)\, ds \quad (7)$$

$$Im(Z) = \frac{N^2\omega}{J_{sz}(H_{exc})S^2}\iint_s 2\pi r R_e(A)\, ds \quad (8)$$

Le calcul de l'impédance est effectué en considérant un courant de 8 mA et une fréquence f=600 Hz [1].

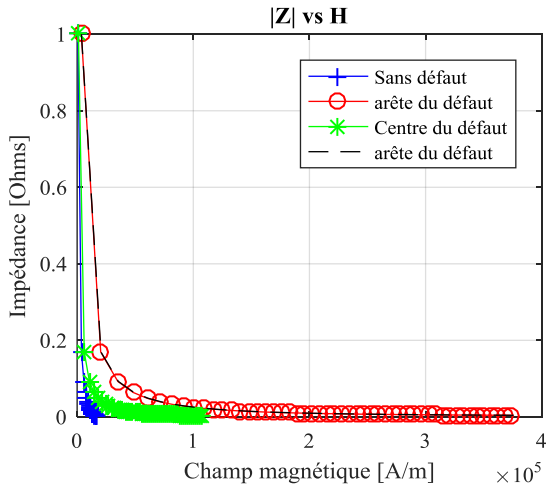

Fig. 3. Variation de l'impédance en fonction du champ magnétique d'excitation.

La figure-3, montre la variation de l'impédance de la bobine pour plusieurs emplacement. On constate que pour chaque position, l'impédance suit le comportement de la courbe de $\mu_r(H)$.

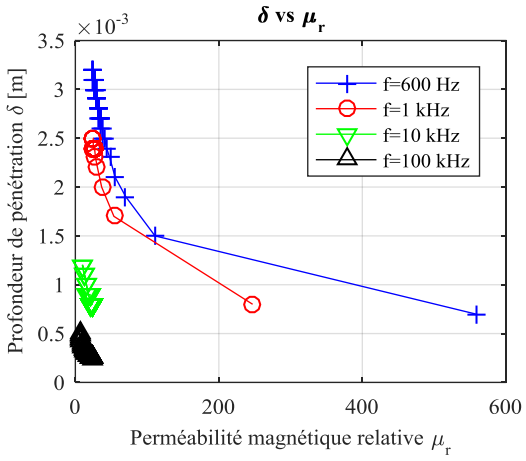

FIg.4 Variation de la profondeur de pénétration en fonction de la perméabilité magnétique relative.

Le graphique ci-dessus montre l'effet de la fréquence sur la profondeur de pénétration dans un acier ferromagnétique. Pour des perméabilités magnétiques relatives importantes, la fréquence doit être faible pour garantir une certaine profondeur de pénétration ce qui constitue un résultat conforme au données de la littérature scientifique. Par conséquent, la validité du modèle éléments finis associes a un modèle non linéaire de perméabilité magnétique se trouve renforcée.

CONCLUSION

Dans ce travail, une solution numérique aux problèmes de calcul de l'impédance en hypothèse non linéaire a été proposée. Le comportement de l'impédance observé montre explicitement que l'impédance de la bobine varie en fonction de l'intensité du courant d'excitation. Ces résultats pourront être exploités dans la conception de dispositifs CND pour l'inspection et la détection de défauts dans les matériaux non-linaires.

REFERENCES

[1] H. Mehaddene, H. Mohellebi, A. Berkache and G. Berthiau, "Eddy Currents Non-Destructive Testing and Evaluation of Ferromagnetic Medium,"*PRZEGLĄD ELEKTROTECHNICZNY (Electrical Review)*, vol. R95, pp. 112–116, February 2019.

[2] N.Nakagawa, "A Theory of Nonlinear Eddy Current NDE Model and its Experimental Tests,"19th World Conference on Non-Destructive Testing 2016, Special Issue of e-Journal of Nondestructive Testing, Vol. 21(7) (eJNDT)ISSN 1435-4934 .

[3] A. Skarlatos, T. Theodoulidis, ''Study of The Non-Linear Eddy Current Response in a Ferromagnetic Plate: Theoretical Analysis for the 2D Case'', *NDT & E International*, vol. 93, pp 150-156, 2018.

[4] F. Azzouz, M. Felliachi, '' Non-Linear Surface Impedance Taking Account of Thermal Effect,'' *IEEE Transactionsons on Magnetics*, vol. 37, No. 5, pp. 3175-3177, 2001.

Influence of Magnetic Field on Spin waves Dispersion in Ferromagnetic Multilayers

Ouiza Haddag
Laboratory of physics and quantum chemistry
Mouloud Mammeri University
Tizi-Ouzou, Algeria
ouiza.haddag@ummto.dz

Ouahiba Nafa
Laboratory of physics and quantum chemistry
Mouloud Mammeri University
Tizi-Ouzou, Algeria
ouahiba.nafa@ummto.dz

Boualem Bourahla
Laboratory of physics and quantum chemistry
Mouloud Mammeri University
Tizi-Ouzou, Algeria
boualem.bourahla@ummto.dz

Abstract**—** *Theoretical approach is used to understand and predict the impact of an external magnetic field on spin waves in periodic multilayers made of alternating three atomic plans transition metals and three atomic plans rare earth material. The magnetic field is perpendicular to the layers. The matrix dynamics and the dispersion relations of this system is obtained used the Heisenberg Hamiltonian.*

Keywords**—** *spin waves, ferromagnetic multilayers, external magnetic field.*

I. INTRODUCTION

Recently, many experimental and theoretical studies are interested to propreties of magnetic multilayers [1-3]. The reasons for this are due to their potential application in industry and their new properties, which appear, like the effect of interfaces. The new periodicity introduces band gaps in the dispersion relations for fundamental excitations in the material, as presence of an anisotropy field which can direct the spins perpendicular to the layers [4-5]. Collective features are also observed in magnetic excitations. Even in diapers magnetic and non-magnetic systems, this allows their applications in the field of sensors and information storage. The propagation of spin waves in solid matter is the main property, which forms the basis of the various uses and technological applications of magnetic multilayers. The presence of interfaces in this type of materials can have a significant effect on spin dynamics[6-7]. Therefore, knowledge of their atomic scale and their impact is necessary to understand their fundamental properties and propose ways to control their magnetic behavior for device applications in different fields. In this work, we study the magnetic properties in multilayers, of the TM/RE type. In particular, we analyze the influence of the magnetic field on the spin waves scattering in a ferromagnetic material consisting of three atomic planes of Iron and three atomic planes of Dysprosium.

II. STRUCTURAL MODEL

A typical 2D cross section of the structural model considered in this paper is shown in Fig. 1. The system studied is periodic multilayers made of alternating of three atomic planes of Iron and three atomic planes of Dysprosium. The magnetic field is perpendicular to the layers. The exchange interactions in each layer are between atoms of the same chemical nature (J_{FeFe}= *6.1 eV* [8] and J_{DyDy}=*7.5 eV* [9]). The magnetic exchange interaction J_{FeDy} is taken as the arithmetic mean of the values J_{FeFe} and J_{DyDy} $J_{FeDy} = (J_{FeFe} + J_{DyDy})/2$.

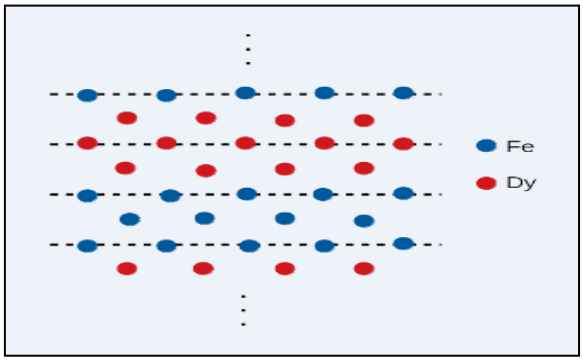

Fig. 1: A schematic representation of multilayer model system Fe/Dy

III. THEORETICAL APPROACH

For ferromagnetic Heisenberg exchange interactions between nearest neighbors and the Zeeman energy of the spins in an external field, the Hamiltonian of the ground state is given by the following expression

$$H = H_{ex} + H_{Zeeman} \quad (1)$$

The first term is the exchange energy between nearest neighbors *i* and *j* given by

$$H_{ex} = -\frac{1}{2}\sum_{i,j} J_{ij} S_i S_j \quad (2)$$

the second term is the energy of the individual spins in the presence of a magnetic field is given by

$$H_{Zeeman} = g\mu_B \sum_i S_i H_0 \quad (3)$$

where S_i, S_j are the spin vectors, J_{ij} is the exchange integral between magnetically nearest neighbor sites *i* and *j* , *g* is the Landé factor, μ_B is the Bohr magneton and H_0 the external applied field.

The equation (1) allowed to write the spin dynamics of the six atomic sites Fe and Dy that constitute the cell unit.

We obtain six equations which may be cast in the matrix form

$$[\Omega I - D(\eta)]/u> = 0/u> \quad (4)$$

Where *I* is the identity matrix and $|u>$ denotes the vector of spins amplitudes along the principal axes in a unit cell and *D* is the dynamical matrix. $\eta \equiv e^{i\varphi x}$, $e^{i\varphi y}$ and $e^{i\varphi z}$ are the Bloch phase factors along the principal axes, between neighboring sites. $\varphi_\alpha = q_\alpha a$ is the normalized wave vector in the α-direction. $\Omega = \omega/\omega_0$ is a dimensionless frequency.

The ω is the frequency of spin lattice precession and ω_0 is the characteristic frequency.
The resolution of Eq. (4) determines the eigenfrequencies Ω as well as the corresponding eigenvectors $|u>$ of the system. To illustrate the model, we have presented the dispersion curves $\Omega(\varphi_x)$, in Fig. 2, as a function of the normalized wavevector φ_x, where q_x runs in the interval $[-5\pi/a, +5\pi/a]$, a is the lattice parameter.

IV. Numerical Applications and Discussions

The dispersion branches for the spin waves in the multilayer system Fe/Dy are represented, in Fig. 2. They are plotted over the interval of $\varphi_x \in [-5\pi/a, +5\pi/a]$ for two possibilities of H_0 : Fig.2.(a) corresponds to $H_0 = 0$ and Fig.2.(b) to $H_0 \neq 0$.

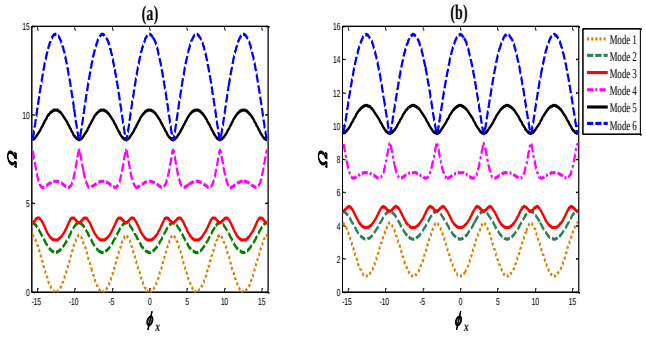

Fig.2: Spin waves dispersion modes in a ferromagnetic multilayer , made of alternate of three layers of Fe and Dy : (a) for $H_0 = 0$ and (b) for $H_0 \neq 0$

We obtained six spin branches, there is just one acoustical mode in Fig. 2.(a), it is characterized by a limiting behavior, tending to zero frequency when q_x tends to zero; but for the others spin modes are optical modes, with branches that differ from zero in the long wavelength limit.

When we apply an external electric field, the spin modes shift towards high energies. This is very well shown in Fig.2.b.

The spin waves could be used in quantum technology, as ultra-precise sensors and in the development of quantum computers.

References

[1] B. Skubic, E. Holmström, and O. Eriksson , "Magnetic moments and exchange interactions in $Fe_{0.82}Ni_{0.18}$/V bcc (001) multilayers ", Phys. Rev. B 70, 094421 (2004).

[2] L.V.Panina, K. Mohri, " Magneto-impedance in multilayer films", Sens. Actuators A, 81, 71–77(2000).

[3] P.V. Prudnikov, V.V. Prudnikov, M.V. Mamonova, N.I. Piskunova, "Influence of anisotropy on magnetoresistance in magnetic multilayer structures ", J. Magn. Magn. Mater, 482, 201-205(2019).

[4] I. S. Y. Liu, P. Yang, P. J. Kelly, "Gilbert damping for magnetic multilayers with perpendicular magnetic anisotropy", Phys. Rev. B 109, 014416 (2024).

[5] P.M.T. Johnson, R. Jungblut, P.J. Kelly, F.J.A. Broeder, "Perpendicular magnetic anisotropy of multilayers: recent insights", 148, 118-124 (1995).

[6] O. Busel, O. Gorobets, Y.Gorobets, "Propagation of spin waves through an interface between ferromagnetic and antiferromagnetic materials", J. Supercond. Nov. Magn.,32, 3097-3102(2019).

[7] H. Puszkarski, "Spin-wave surface parameter characterization of magnetic thin film interfaces", J. Phys. Colloques 45, C5-325-C5-327(1984).

[8] E. Talbot , P. E. Berche , D. Ledue , R. Patte, "Magnetic properties of Fe/Dy multilayers: a Monte Carlo investigation", J. Magn. Magn. Mater., 316, Issue 2, Pages 281-284,September (2007).

[9] Tzu-Hung Chuang, "High wave-vector magnon excitations in ultrathin Fe (111) films grown on Au/W (110) and Fe (001) films grown on Ir(001) ", doctoral theses (2013).

Session 6 (Orale):

Electromechanical and Induction Devices

- 2D Parametric Study of a DC Induction Heater for Aluminum Billets
- Cooling of heat sink system using an active vibration piezoelectric beam and passive techniques using Al 2 O 3 nanofluid pumping
- Bearing Fault Diagnosis Method based on EEMD and Quantile Weighted Permutation Entropy
- Contrôle de la température pour le Laminage à chaud par le chauffage par induction
- Quadrotor control using cascaded feedforward linearization and LPV modeling
- Modeling and Evaluating of Solid Oxide Fuel Cell Performance using Trap-designed Interconnects

2D Parametric Study of a DC Induction Heater for Aluminum Billets

Ibrahim HEDOUACHE
Electrical Engineering and Industrial Electronics Laboratory (L2EI)
University of Jijel
Jijel, Algeria
Ibrahim.HEDOUACHE@univ-jijel.dz

Hocine BOUCHEKHOU
Electrical Engineering and Industrial Electronics Laboratory (L2EI)
University of Jijel
Jijel, Algeria
hbouchekhou@gmail.com

Souri Mohamed MIMOUNE
Laboratory of Energy Systems Modeling (LMSE)
University of Biskra
Biskra, Algeria
s.mimoune@univ-biskra.dz

Roujaina BOUGANDOURA
Electrical Engineering and Industrial Electronics Laboratory (L2EI)
University of Jijel
Jijel, Algeria
roujaina.bougandoura@univ-jijel.dz

Hicham ALLAG
Electrical Engineering and Industrial Electronics Laboratory (L2EI)
University of Jijel
Jijel, Algeria
allag_hic@yahoo.fr

***Abstract*—This study presents a 2D simulation of a DC induction heater designed for aluminum billets. The heater utilizes an iron core to concentrate the magnetic field in the air gap generated by DC flowing through copper windings. The aluminum billet is positioned within the air gap of the core and rotated by a motor (1450 rpm) to achieve uniform heating. The simulation investigates the behavior of the heater under various operating conditions, analyzing the resulting heating processes.**

Keywords— DC induction heating, iron core, aluminum billet, copper windings, magnetic field, rotation speed, temperature distribution, COMSOL Multiphysics.

I. INTRODUCTION

Induction heating is gaining significant traction across various industrial applications, including heat treatment and assembly processes. When a stationary conductor is placed within a rapidly changing magnetic field, eddy currents are induced within the conductor. These eddy currents generate heat due to Joule heating [1].

Induction heating isn't limited to stationary conductors; moving a conductor through a static magnetic field also effectively induces eddy currents and resulting heating [2].

A laboratory-scale DC induction heater with iron yoke for aluminum billet was designed and tested by J. Yang in China in 2014 [3]. A novel DC induction heater prototype with movable iron blocks was fabricated to validate the feasibility of the adjustable air gap method by J. Ma in China in 2016 [4].

In this study, 2D numerical model was built using COMSOL Multiphysics to analyze the temperature distribution. The results obtained from the simulation verified that magnetic field density, rotation speed and heating time are significant parameters affecting the temperature distribution. 2D simulations are simpler and less complex, making them faster and easier to run.

II. INDUCTION HEATER MODEL

A. Design of DC induction heater

The model consists of a DC power supply, C-shape iron core, copper windings, aluminum billet end electrical motor. The billet to be heated is placed in the air gap of the iron core and is driven by the motor. The magnetic field in the gap is guided by an iron core, which is responsible for heating the billet and it is generated using copper windings.

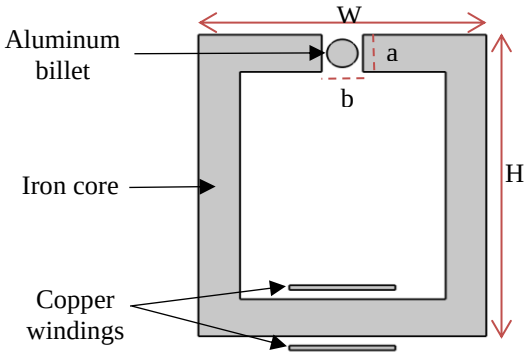

Fig. 1. DC induction heater topology.

Copper windings consist of 6 coils which is wound by 70 turns of each coil, all of them are in parallel connections they are wound on the bottom of the iron yoke, as shown in fig. 1. We assumed that all the coils are immersed in liquid nitrogen to handle high currents (I=200 A).

III. NUMERICAL MODEL

The numerical model of induction heating contains two models: electromagnetic model and thermal model. These two models are calculated by COMSOL Multiphysics.

A. Electromagnetic Model

The electromagnetic equation expressed as:

$$\vec{\nabla} \times \vec{H} - \sigma \upsilon \times \vec{B} = \vec{J} \quad (1)$$

$$\vec{J} = \sigma \vec{E} \quad (2)$$

$$\upsilon = (y \cdot \omega, -x \cdot \omega, 0) \quad (3)$$

B, H, E, J and σ are respectively the magnetic flux density field intensity, electrical field, current density and conductivity $\vec{B} = \mu \vec{H}$. υ and ω are the rotational and angular velocity of the billet, respectively.

B. Thermal Model

Thermal model calculates heating power by calculating the induction resistance loss inside the billet as follows:

$$Q = J \, . \, J/\sigma \quad (4)$$

In order to calculate the heating process, the thermal model

TABLE I. Geometrical Parameters of DC Induction Heater

Symble	*Quantity*	*Value*
H	Hight of the iron core	560 (mm)
W	width of the iron core	500 (mm)
a	Hight of the air gap	80 (mm)
b	Width of the air gap	80 (mm)
R_{cw}	Copper wire radius	1.25 (mm)

must be coupled with the electromagnetic one.

$$\rho Cp\frac{\partial T}{\partial t} + \nabla.(-k\nabla T) = Q \qquad (5)$$

where ρ, Cp and k are respectively, the density of billet (30 mm of radius), heat capacity and thermal conductivity.

IV. SIMULATION RESULTS AND DISCUSSIONS

Figures 2 shows the distribution of the magnetic flux density. We observe that the maximum value is at the bottom of the iron core, then it reduces along its height.

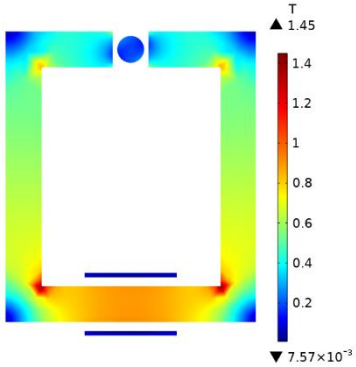

Fig. 2. Magnetic flux density distribution in the total topology.

The two following figures illustrate the distribution of induction heating power density (3.a), temperature's distribution (3.b) in the billet and magnetic flux density, fig.4. We observe that the magnetic field decreases as we move towards the center of the billet.

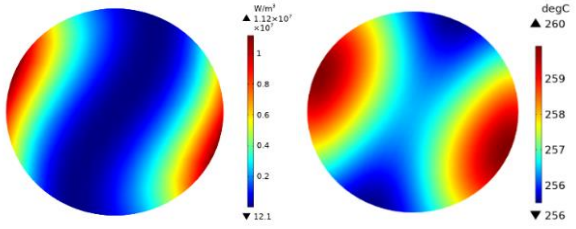

(a) (b)

Fig. 3. Distribution of: Induction heating power density (a) and temperature in the billet (t= 300 s) (b).

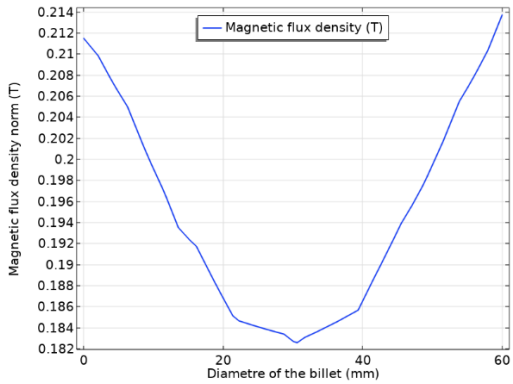

Fig. 4. Magnetic flux density distribution in center of the billet.

Figures 5 shows the location of the temperature calculation point (0,315).

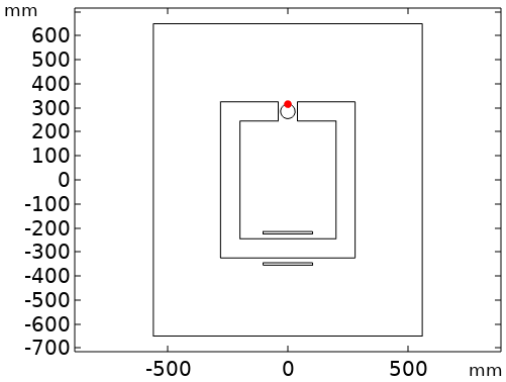

Fig. 5. Temperature Calculation Point.

From figure 6, we observe that the temperature increases as the electric current value increases, and the temperature rise becomes more noticeable with longer heating times.

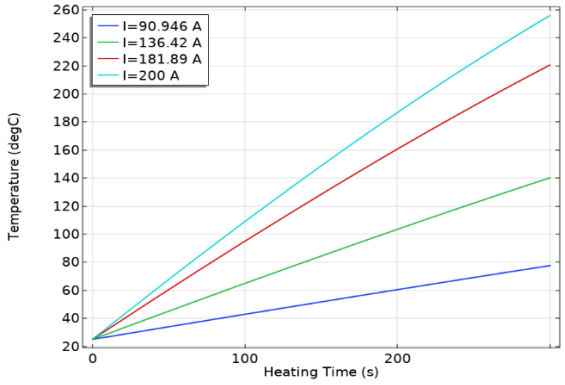

Fig. 6. Temperature distribution on the billet surface; with four values of electrical current at different time

VI.CONCLUSION

In this study, we present the results of a 2D simulation for a DC induction heater with an iron core used to heat aluminum billets. The temperature distribution within the billet depends on several parameters, including magnetic field density, electrical current, rotation speed and heating time. 2D model simulations require significantly less computational power and time to complete.

VI. REFERENCES

[1] Abdi, A., Y. Ouazir, G. Barakat, and Y. Amara, "Transient quasi-3D magneto-thermal analyticalsolution in PM induction heating device," COMPEL — The International Journal for Computationand Mathematics in Electrical and Electronic Engineering, Vol. 39 No. 5, 1131–1144, 2020.

[2] M. Messadi, L. Hadjout, Y. Ouazir, T. Lubin, S. Mezani, A. Rezzoug, and N. Takorabet, "Eddy current computation in translational motion conductive plate of an induction heater with consideration of finite length extremity effects," IEEE Trans.Magn,, vol. 52, Issue: 3 , 1–4, March 2016.

[3] J. Yang, H. Gao, Y. W. Wang, D. Q. Xu, Z. Hong, Z. Jin, and Z. Y. Li et al., "Design and experimental results of a DC induction heater prototype for aluminum billets," IEEE Trans. Appl. Supercond., vol. 24,no. 3, Jun. 2014, Art. no. 0500704.

[4] J. Ma, J. Sheng, Z. Yao, H. Gan, H. Li, and X. Ai, "Experimental and Numerical Study of a DC Induction Heater Prototype With an AdjustableAir Gap Structure," IEEE T. Appl. Supercond., vol. 26, no. 4, pp. 1–5, Jun.2016

Cooling of heat sink system using an active vibration piezoelectric beam and passive techniques using Al_2O_3 nanofluid pumping

Bouttout Abdelouahab
National Center of Studies and Integrated Research of Building Engineering, CNERIB, Cité Nouvelle El-Mokrani, Souidania, 16097, Algeria.
Mail: Bouttout@gmail.com
ORCID: 0000-0003-3907-0471

Rouibah Nassir
National Center of Studies and Integrated Research of Building Engineering, CNERIB, Cité Nouvelle El-Mokrani, Souidania, 16097, Algeria.
Mail: rouibahnassir@gmail.com

***Abstract*—Industries in the electronics sector grapple with challenges arising from elevated power densities and heightened heat generation in electronic devices. It underscores the significance of effective thermal management as a solution for maintaining peak performance and averting failures caused by thermal issues.**

The study focuses on forced convection flow through power supply with identical heat sink devices, exploring two cooling techniques: air piezoelectric fan and Al2O3 nano fluid.

The finite volume method is employed to solve governing equations. In the first case, the effects of pulsation flow frequencies and temperature modulation frequency on heat transfer rates are investigated in detail. In the first case, for the piezoelectric fan, the study finds that the time-averaged Nusselt number for each electrical device depends on pulsation frequency and heat modulation, consistently exceeding that in steady-state conditions. Results indicate a specific band of frequencies where heat transfer enhancement surpasses 55%, with maximum efficiency observed at a certain pulsation frequency. The temperature of the heat sink and power pumping at different Reynolds numbers has been studied. The power loss is notably higher compared to steady-state conditions. The study validates numerical simulations with experimental results.

In the second case, Al2O3 nano fluid is used to identify resonance heat transfer over heat sinks, occurring when external forcing frequency matches the natural frequency of the nanofluid flow. The results reveal instability at a critical Reynolds number for nano fluid Al2O3, with enhanced heat transfer rates in specific frequency bands. The enhanced heat transfer can reach 30-170% within a defined range of Strouhal numbers and corresponding frequencies.

Keywords—forced convection, cooling, heat sink, piezoelectric fan, nanoflui Al_2O_3

I. INTRODUCTION

In many industrial applications, the heat flux is increased due to many complicated manufactured processes. In this case, many equipment and components has sensitivity of temperature variation during their function. In order to keep the functionality of component in their temperature level, it is important to transport the calories away from the hot spot locations. In electronic component the heat flux dissipation of CPU can achieved the 110-140 W, it increases significantly with input voltage and frequency [1]. Bar-Cohen et al. [2] showed that the durability can be improved significantly by operating the device with reasonable temperature below than 85 °C. In addition, the reliability of silicon chips can decrease by 50 % for every 10 °C temperature rise. In addition to change in the architectural configuration of heat exchangers such as, chaps and roughness of surfaces in order to increase heat transfer rate, it is important to modify the physical characteristics of the fluid. Nano fluids particles dispersed in base fluid demonstrate a good heat transfer transport phenomena [3]. Nanofluids are engineered suspensions of nanometer-sized solid particles or nanoparticles in a base fluid, exhibiting extraordinary thermophysical properties compared to conventional cooling fluids. The combination of nanoparticles and base fluids results in an enhanced heat transfer coefficient and improved thermal conductivity, making nanofluids promising candidates for efficient cooling. Monireh Asadi Abchouyeh et al. [4] studied the heat transfer and nanofluid flow around four sinusoidal side obstacles in a horizontal channel using Latice Boltzman Method LBM. The effects of the Reynolds number and nanoparticles volume fraction at different nondimensional amplitudes of the wavy wall of the sinusoidal obstacles are studied. An increase of the Reynolds number leads to a rise of the temperature gradient on the walls of the channel. An increment of nanoparticles concentration results in the heat transfer enhancement. H.A. Mohammed et al. [5] presents laminar mixed convection flow of Al_2O_3/water nanofluids through two hot obstacles mounted on the bottom wall of horizontal channel. The effect on heat transfer of different parameters such as Richardson number, Rayleigh number, nanoparticles volume fraction and aspect ratios of obstacles are examined. Their results show the difference between average Nusselt numbers obtained from the three sets of thermophysical models does not exceed 3%. In addition, the increasing the nanofluid concentration from 0% to 5%, leads to increasing less than 10% of the average Nusselt number over the obstacles.

Kafel A. Mohammed et al. [6] present a summary of experimental and numerical works of heat transfer enhancement through facing step and corrugated channels using conventional fluids and nano fluids. Laminar and turbulent flows regimes through facing step and corrugated

channels are presented. Their previous works show that good agreement between numerical and experimental studies to enhance heat transfer. The corrugated facing step channel is new design proposed to enhance heat transfer rate. The heat transfer enhancement was evaluated up to 60% when using nanofluid in the facing step channel configurations. Regression equations can correlate relationships between the Nusselt number and the flow parameters. The friction factor is important parameter to calculate the pressure drop through inlet and outlet of the corrugated channel and keep optimum heat transfer enhancement.

Pishkar, B. Ghasemi et al. [7] presents a numerical study of laminar mixed convection in horizontal channel using pure water and Cu-water nanofluid over two blocks mounted on the bottom wall heated at a constant temperature. Different parameters are studied: Reynolds and Richardson numbers, the solid volume fraction, and the distance and the thermal conductivity of the blocks. The distance and the thermal conductivity of the blocks has significantly effect on the heat transfer rate. The influence of the solid volume fraction on the heat transfer is clearer at higher Reynolds number.

Bouttout et al. [8] studied numerically the hydrodynamic amplification and thermal instabilities by imposing pulsation during forced convection of air-cooling of nine identical heated blocks mounted on a horizontal channel. The new feature of this work is that a narrowband of frequencies which the enhancement of heat transfer of all electronic components is in the range of 25%-55% compared with steady non pulsation flow is obtained. Good agreement between numerical simulations and experimental results available from literature is obtained. Recently, Bouttout et al. [9] investigated forced convection flow of air through power supply box with piezoelectric fan of nine identical electrical devices. The efficiency of piezoelectric fan is expressed by the maximum temperature of the ninth electrical device which not exceed 80 °c for time-averaged velocity of 0.556 m/s and vibration frequency of 34.75 Hz of piezoelectric fan. the pressure drop and power pumping of piezoelectric fan are obtained for different Reynolds numbers. The power loss was 4.6 times higher than for the piezoelectric fan at Re=500.

Non-fluid cooling in various heat sink configurations and obstacles has been explored by numerous researchers [9], [10], [11]. However, limited attention has been given to unsteady modes and resonance heat transfer phenomena.

The present work examines the combination of the two methods such as an active method using piezoelectric beam (pulsation of the fluid at the entrance of the channel) with a passive method (the addition of the nanoparticles-Al_2O_3 in the base fluid). We numerically simulate the exitance of large band of frequencies for which the heat transfer is maximal and proved the existence of resonance heat transfer using nonfluid. The Resonance heat transfer occurs when the frequency of an external forcing (pulsation or oscillation) matches the natural frequency of the nanofluid or the system. When this resonance condition is met, the nanofluid experiences significant energy transfer, leading to enhanced heat dissipation capabilities.

REFERENCES

[1] S.M. Sohel Murshed, C.A. Nieto de Castro. A critical review of traditional and emerging techniques and fluids for electronics cooling. Renewable and Sustainable Energy Reviews 78 (2017) 821–833.

[2] Alena Pietrikova, Tomas Girasek, Peter Lukacs, Tilo Welker, Jens Muller. Simulation of cooling efficiency via miniaturised channels in multilayer LTCC for power electronics. Journal of ELECTRICAL ENGINEERING, VOL 68 (2017), NO2, 132–137.

[3] Tamas Orosz — Zoltan Adam Tamus. IMPACT OF THE COOLING EQUIPMENT ON THE KEY DESIGN PARAMETERS OF A CORE–FORM POWER TRANSFORMER. Journal of ELECTRICAL ENGINEERING, VOL 67 (2016), NO6, 399–406.

[4] Vladimır Goga— Juraj Paulech— Michal Vary. COOLING OF ELECTRICAL Cu CONDUCTOR WITH PVC INSULATION – ANALYTICAL, NUMERICAL AND FLUID FLOW SOLUTION. Journal of ELECTRICAL ENGINEERING, VOL. 64, NO. 2, 2013, 92–99.

[5] A. Bar-Cohen, A.D. Kraus, S.F. Davidson, Thermal frontiers in the design and packaging of microelectronic equipment, Mechanical Engineering, 105, pp.530-539, 1983.

[6] A. Dogan, M. Sivrioglu, S. Baskaya, Experimental investigation of mixed convection heat transfer in a rectangular channel with discrete heat sources at the top and the bottom, International Communications in Heat and Mass Transfer, 32, pp.1244-1252, 2005.

[7] B. Ghasemi, Mixed convection in a rectangular cavity with a pulsating heated electronic component. Numerical Heat Transfer, Part A, 47, pp.505–521, 2005.

[8] C.Y. Soong, P.Y. Tzeng, C. D. Hsieh, Numerical study of bottom-wall temperature modulation effect on thermal instability and oscillatory cellular convection in rectangular enclosure. International Journal of Heat and Mass Transfer 44 (2001) 3855-3868.

[9] H.A. Mohammed, Omer A. Alawi, M.A. Wahid, Mixed convective nanofluids flow in a channel having backward-facing step with a baffle, Powder Technology (2014),

[10] Kafel A. Mohammed, A.R. Abu Talib, A.A. Nuraini, K.A. Ahmed.Review of forced convection nanofluids through corrugated facing step. Renewable and Sustainable Energy Reviews 75 (2017) 234–241.

[11] I. Pishkar, B. Ghasemi. Cooling enhancement of two fins in a horizontal channel by nanofluid mixed convection. International Journal of Thermal Sciences 59 (2012) 141-151.

[12] J.W. Moon, S.Y. Kim, H.H. Cho, Frequency-dependent heat transfer enhancement from rectangular heated block array in a pulsating channel flow. International Journal of Heat and Mass Transfer, 48, pp.4904-4913, 2005.

[13] Paisarn Naphon, Osod Khonseur. Study on the convective heat transfer and pressure drop in the micro-channel heat sink. International Communications in Heat and Mass Transfer 36 (2009) 39–44.

[14] R.K.B. Schacht, A. Hausdorf, B. Wunderle, S. Rzepka, B. Michel, Efficiency optimization for a frictionless air flow blade fan – design study, 14th IEEE Conference on Thermal and Thermomechanical Phenomena in Electronic Systems.(ITHERM)2014,pp.1019-1026.

Bearing Fault Diagnosis Method based on EEMD and QuantileWeighted Permutation Entropy

Ahmed Taibi
L2EI Laboratory, Jilel University BP 98 Ouled Aïssa 18000, Jijel, Algeria
taibi.ahmed@univ-jijel.dz

Nabil Ikhlef
L2EI Laboratory, Jilel University BP 98 Ouled Aïssa 18000, Jijel, Algeria
ikhlefnabil@yahoo.fr

Lyes Aomar
L2EI Laboratory, Jilel University BP 98 Ouled Aïssa 18000, Jijel, Algeria
aomarlyes@univ-jijel.dz

***Abstract*— Vibration signals of rolling bearings are often non-stationary and non-linear, thus it is difficult to extract sensitive features using traditional signal processing methods. Therefore, a new method for diagnosing bearing faults, based on the Ensemble Empirical Mode Decomposition (EEMD), Sample Quantile Weighted Permutation Entropy (SQWPE), and Whale Optimization Algorithm Least Squares Support Vector Machine (WOA-LSSVM), was proposed. Firstly, EEMD is utilized to decompose the original bearing vibration signal into several Intrinsic Mode Functions (IMFs), and the Pearson correlation coefficient (PCC) is employed to select the IMFs that contain the main failure information. Secondly, the SQWPE is calculated for each selected IMF to construct the feature vectors. Finally, the obtained feature vectors are inputted into the WOA-LSSVM algorithm for training and classification. The effectiveness of the proposed method were verified using experimental data.**

Keywords—Fault diagnosis, rolling Bearing, EEMD, SQWPE, WOA, LSSVM

I. INTRODUCTION

Rolling bearings are among the essential components of rotating machines that play an essential role in modern industry. Its failure is one of the most common reasons for machine failure. According to many researches, more than 44% of rotating machinery equipment failures are caused by bearing faults. Therefore, the fault diagnosis of rolling bearings has attracted great attention from research communities so as to avoid catastrophic failures and increase the reliability of industrial equipment [1] [2]. Rolling bearing failure diagnosis can be characterized in three steps: signal processing , feature extraction, and fault classification .

To extract effective fault feature information from vibration signal data, various signal analysis algorithms are typically employed, including Wavelet Transform (WT) [3], Empirical Mode Decomposition (EMD) [4], Ensemble Empirical Mode Decomposition (EEMD), and Variational Mode Decomposition (VMD). Then, entropy-based feature extraction techniques, such as Sample Entropy (SE), Permutation Entropy (PE) [5], and Weighted Permutation Entropy (WPE), are commonly utilized in fault diagnosis applications. However, the above methods have some inherent disadvantages, for example, in Sample entropy It takes a long time to find the entropy values, Thus, the loss of important information. PE calculation often involves parameters such as embedding dimension and time delay, which need to be carefully chosen. Suboptimal parameter selection can lead to inaccurate results and affect the performance of the diagnostic model. Therefore, to address some of these shortcomings, in this study we proposed SQWPE to extract features.

In this study, we employ EEMD to analyze vibration signals, SQWPE for fault feature extraction, and the LSSVM classifier optimized by WOA for identifying and classifying different bearing faults .

II. PROPOSED FAULT DIAGNOSIS APPROCH

To enhance the accuracy of bearing fault detection, this paper introduces a novel intelligent fault diagnosis approach. The specific steps of this approach are outlined below:

1) Decomposing rolling bearing vibration signals into several Intrinsic Mode Functions (IMFs) using the Ensemble Empirical Mode Decomposition (EEMD) method.
2) Using the Pearson correlation coefficient (Pcc) to select the IMFs that contain the main failure information.
3) Calculate the sample quantile weighted permutation entropy (SQWPE) for each selected IMF to construct the feature vector.
4) Applying steps 1 to 3 to all vibration signals to generate a matrix containing faults features.
5) Normalize the fault feature matrix values to the range [0, 1] using the mapminmax function in MATLAB.
6) The normalized fault features are randomly divided into two groups: a training sample set and a testing sample set
7) The training set is employed as input to the enhanced LSSVM classifier using the WOA algorithm, to train and obtain a classification model, while the test set is fed into the trained model to identify and classify the different types of bearing defects.

III. EXPERIMENTAL IMPLEMENTATION

In order to verify the effectiveness of the proposed method, empirical data from Case Western Reserve University (CWRU) was used. The experimental seat is mainly composed of three-phase induction motor, loading motor and torque sensor. A deep groove ball bearing has been used SKF6205 experiment. The bearing's shaft rotates at a speed of 1730 r/min, with a sampling frequency of 12000 Hz. The considered bearing faults include ball fault (BF), inner race fault (IRF), outer race fault (ORF) and normal operation (NO). Table I presents different types of failure in rolling bearing, and more details can be found in reference [6].

To construct the experimental data matrix, the bearing vibration signal is partitioned into four classes. Each class comprises 144 samples, with each sample containing 2048 data points, resulting in a total of 576 samples. Two-thirds of the data matrix are selected as training data, while the remaining one-third will be used as testing data.

In this study, we employed the EEMD algorithm to decompose various vibration signals into Intrinsic Mode Functions (IMFs). Subsequently, we selected four components (IMFs) with higher correlation to the original signal using the Pearson correlation coefficient. Following this, we calculated the Sample Quantile Weighted Permutation Entropy (SQWPE) for each IMF to construct the feature vectors. These feature vectors were then normalized to the range [0, 1]. Finally, we fed the normalized feature vectors into an improved LSSVM classifier using the WOA algorithm to classify different bearing faults. The identification rates of our proposed method and other methods are presented in Table II. Additionally, the detailed classification results for the EEMD-WPE-LSSVM method and our proposed method (EEMD-SQWPE-WOA_LSSVM) are depicted in Figures 1 and 2, respectively.

From table II, we notice that the identification rate of the proposed method (EEMD-SQWPE-WOA_LSSVM) reaches 100%, while in the other methods it is equal to 96.35 % when using the EEMD-WPE-WOA_LSSVM method and 95.31% in the case of the EEMD-WPE-LSSVM method. This indicate the superiority and effectiveness of the proposed method compared with other methods in diagnosis of bearing fault.

TABLE I. DIFFERENT TYPES OF FAILURE IN ROLLING BEARING

Bearing conduction	Assigned labels	Category label
Normal	NO	1
Ball Fault	BF	2
Inner Race Fault	IRF	3
Outer Race Fault	ORF	4

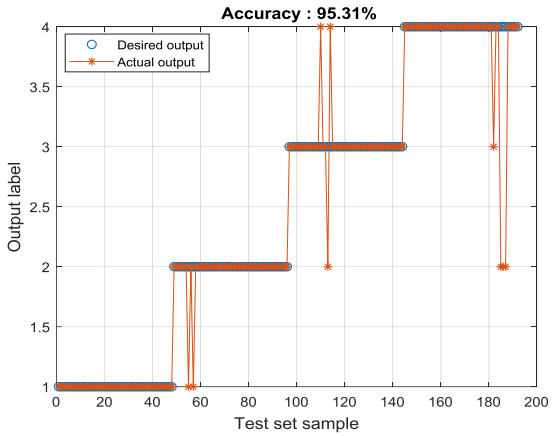

Figure 1. Classification results of EEMD-WPE-LSSVM method

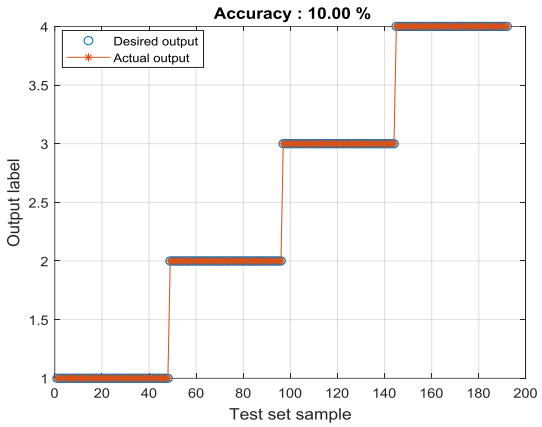

Figure 2. Classification results of proposed method (EEMD-SQWPE-WOA_LSSVM).

TABLE II. COMPARISON OF IDENTIFING RATE OF DIFFERENT METHODS

Methods	Identifying rate (%)
EEMD-WPE-LSSVM	95.31 %
EEMD-WPE-WOA_LSSVM	96.35 %
EEMD-SQWPE-LSSVM	97.91 %
EEMD-SQWPE-WOA_LSSVM	100 %

IV. CONCLUSIONS

To achieve accurate and efficient identification of various fault states in bearings, this paper introduces a novel approach for bearing fault diagnosis based on the EEMD, SQWPE and WOA-LSSVM algorithm. The key conclusions drawn from this study are outlined below:

1- The results obtained demonstrated the ability of SQWPE to extract features compared to WPE.

2-The efficacy and viability of the method proposed in this research were substantiated through the utilization of experimental data and comparison with other methods.

REFERENCES

[1] A. Taibi, N. Ikhlef, and S. Touati, " A novel intelligent approach based on WOAGWO-VMD and MPA-LSSVM for diagnosis of bearing faults," Int J Adv Manuf Technol 120, 3859–3883, March 2022.

[2] Q. Chen, S. Dai, and H. Dai, "A Rolling Bearing Fault Diagnosis Method Based on EMD and Quantile Permutation Entropy," Mathematical Problems in Engineering, vol. 2019, pp. 1–8, Sep. 2019.

[3] H. Zhu, Z. He, J. Wei, J. Wang, and H. Zhou, "Bearing Fault Feature Extraction and Fault Diagnosis Method Based on Feature Fusion," Sensors, vol. 21, no. 7, p. 2524, Apr. 2021.

[4] C. Grover and N. Turk, "Rolling Element Bearing Fault Diagnosis using Empirical Mode Decomposition and Hjorth Parameters," Procedia Computer Science, vol. 167, pp. 1484–1494, 2020.

[5] K. Noman, D. Wang, Z. Peng, and Q. He, "Oscillation based permutation entropy calculation as a dynamic nonlinear feature for health monitoring of rolling element bearing," Measurement, vol. 172, p. 108891, Feb. 2021.

[6] CWRU (2008) Case Western Reserve University Bearing Date Center Website; CWRU: Cleveland, OH, USA. Available online: https://engineering.case.edu/bearingdatacenter/download-data-file.

Contrôle de la température pour le Laminage à chaud par le chauffage par induction

M. Rezig, K. Srairi
Department of Electrical Engineering,
University of Biskra,
Laboratory of Energy Systems Modeling
(LMSE), BP 145, Biskra 07000 – Algeria
E-mail: m.rezig@univ-biskra.dz,
ksrairi@yahoo.fr

Abstract— ***Le travail actuel concerne le contrôle de la température pour le Laminage à chaud par le chauffage par induction. Le Matériau Disques plats en acier au bore, diamètre extérieur 460 à 710 mm, épaisseur 3.2 à 10 mm Température 725 ° C Fréquence 75 kHz . Plus précisément, il s'agit des couches d'acier utilisées dans les systèmes de chauffage par induction. Le problème étudié est lié à la régulation de la température de Matériau Disques plats en acier, puis à l'utilisation du modèle pour le laminage. Sur cette base, un modèle d'aimantation basé sur des algorithmes numériques et prenant en compte les variations de température sont proposées. Des variations de température de comptage sont proposés.***

Keywords— plats en acier, température, chauffage par induction, algorithmes numériques

I. INTRODUCTION

Le système de chauffage par induction dans les procédés de laminage est désormais une constante partagée par les producteurs de laminés à chaud les plus qualifiés. L'avantage principal lié à l'utilisation du four à induction, dans les différentes parties du train de laminage suivant les différentes exigences, est le contrôle de la température pour différents matériaux et pour différentes dimensions.
Toutefois Induction est présente sur le marché également avec des applications de chauffage de barres pour le laminage continu, permettant la flexibilité dans le changement de production également avec de petits lots de matière, la réduction de la décarburation superficielle même avec un chauffage en atmosphère éventuel. Depuis toujours, l'homme tente d'améliorer sa vie au quotidien ; le chauffage par induction qui est couramment employé dans les différentes activités humaines ; sa fonction est de chauffer des matériaux sans contact avec la source d'énergie, La facilités de réglage et de mise en marche automatique, l'absence de combustion et de dégagement de gaz toxiques, la propreté des appareils, sont autant d'avantages du chauffage par induction.

Le chauffage par induction a acquis une très grande importance dans l'industrie, notamment, dans la métallurgie, dans ce cas on s'intéresse à chauffer des barres en métaux pour le laminage et utilisation spécifique.

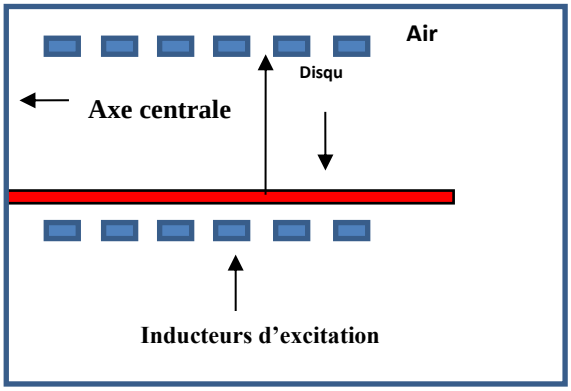

Fig1. Système de chauffage par induction

I. MISE EN EQUATIONS MATHEMATIQUES

L'étudié ainsi de la modélisation physique d'un tel système présenté dans la Fig.1 ; fait intervenir à la fois les équations de la magnétodynamique et la diffusion de la chaleur, il s'agit en effet de déterminer la répartition spatio-temporelle du champ magnétique créé par l'inducteur dans l'espace environnant, puis d'effectuer un calcul de température en utilisant cette puissance dissipée comme source thermique.[5].

Les équations de la magnétodynamique sont issues des équations de Maxwell et l'équation de diffusion de la chaleur est régie par la loi de Fourier, de la façon suivante [8] [9].

II. Model magnétodynamique

Le problème électromagnétique se modélise à l'aide des quatre équations de Maxwell. Pour une configuration axisymétrique dans le cas où la charge est immobile par rapport à l'inducteur [6]. Celle-ci est décrite comme suivant :

$$\overrightarrow{\mathrm{rot}}\left(\upsilon\ \overrightarrow{\mathrm{rot}}\ \vec{A}\right)+\sigma\ \frac{\partial \vec{A}}{\partial t}=\vec{J}_{ex} \qquad (1)$$

III. Model thermique

La température est l'image de la distribution des courants induits laquelle dépend des paramètres suivants ;
La structure géométrique et les Propriétés électromagnétiques, L'évolution de la température est

essentiellement gouvernée par la puissance dissipée par les courants induits. L'équation de la chaleur s'écrit donc ici :

$$k\,\nabla^2 T + \bar{q} = 0 \qquad (2)$$

La valeur de la température atteinte dépende [6], des propriétés électromagnétiques et de la structure géométrique ; Où le terme source provient des puissances dissipées par effet Joule et les conditions aux limites de DIRICHLET et NEUMANN [6][7].

IV. *Model Numérique*

L'ensemble des modèles mathématiques des deux phénomènes magnétique et thermique est décrit par des équations aux dérivées partielles. La résolution d'un tel problème fait appel aux méthodes numériques, parmi ces méthodes nous avons adopté la méthode des volumes finis. Les deux équations (1) et (2) seront intégré sur chaque volume fini, correspondant au nœud principal P, et délimité par les frontières (e, w, s, n) [5]. Après intégration, nous obtenons sous la forme matricielle le système d'équation qui s'écrit sous la forme :

$$[M+iL]\{A^*\} = \{F\} \quad (3)$$

Où : $[M+iL]$ est la Matrice coefficients, $\{A^*\}$ est le Vecteur inconnu et $\{F\}$ est le vecteur source.

La discrétisation par volumes finis est appliquée aux deux systèmes et produit des matrices de système linéaire. On notera que le système de conduction de chaleur a la condition limite de convection mixte [4]:

$$-k\frac{\partial T}{\partial n} = h(T - T_\infty) \qquad (4)$$

II.1 Partie I

Dans le but de mener ce système ayant un disque une seule couche pour la chauffer diamètre extérieur 460 à 710 mm, épaisseur 3.2 à 10 mm Température 725 ° C Fig. 2 et 2., nous avons modélisé leurs comportements magnétique et thermique. Le système de chauffage adopté est composé d'une bobine à six inducteurs à excitation. La plaque étant en acier inoxydable, L'un des défis de chauffage par induction est de choisir la forme et la position de la bobine de ça pour les valeurs de l'entre fer e_1=0.0020 m et les propriétés du courant électrique pour chaque pièce spécifique et ainsi atteindre un profil de température souhaité dans cette pièce, les inducteurs sont connecter en série par une densité de courants source Js = 2,5.10 ^{3} A/m ayant une variation de température a une gamme de fréquence f = 50 KHz

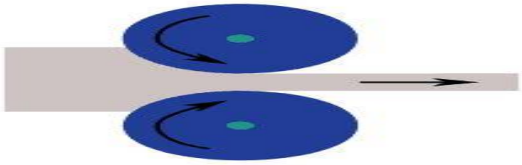

Fig2. Système de laminage a chaud

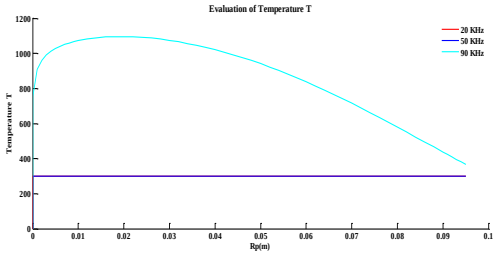

Fig 3. Évaluation spatiale de la température

[1] S. Llorente, F. Monterde, J.M. Burdío, and J. Acero, "A *comparative study of resonant inverter topologies used in induction cookers*", Applied Power Electronics Conference and Exposition (APEC), Vol. 2, 10-14 March 2002, pp. 1168-1174.

[2] F. Forest, S. Faucher, J. Y. Gaspard, D. Montloup, J. J. Huselstein, and C. Joubert, "*Frequency-synchronized resonant converters for the supply of multiwinding coils in induction cooking appliances*," IEEE Trans. Ind. Electron., vol. 54, no. 1, pp. 441–452, Feb. 2007.

[3] N. Tsopelas and N. J. Siakavellas, "Influence of some parameters on the effectiveness of induction heating," IEEE Trans. Magn., vol. 44, no. 12, pp. 4711–4720, Dec. 2008.

[4] L. C. Meng, K. W. E. Cheng, and W. M. Wang, "Thermal impacts of electromagnetic proximity effects in induction cooking system with distributed planar multicoils," IEEE Trans. Magn., vol. 47, no. 10, pp. 3212–3215, Oct. 2011.

[5] L. Alloui '' *Modélisation tridimensionnelle par la méthode des volumes finis phénomènes Electromagnétiques et thermiques couplées dans les dispositifs de chauffage par induction* '', Thèse de magister, Université Biskra- Algérie, 2003

[6] Jin-Kyu Byun, Kyung Choi '' *Optimal Design Procedure for a Practical Induction Heating Cooker*",IEEE transaction on magnetics, Vol.36, No.4, Juillet 2000.

[7] Jin-Kyu Byun, Kyung Choi, Song-Yhahn, Optimal Temperature Control for Induction Heating Devices Using Physical and Geometrical Design Sensitivity: IEEE transaction on magnetics, Vol.33, No.5, September 1998.

[8] M. Feliachi and G. Develey, Magneto thermal behaviour finite element analysis for ferromagnetic materials in induction heating devices: IEEE transaction on magnetic, Vol 27, No 6, P 5235-5237, Nov1991

[9] A.ABDELKADER MEKKI, A. KANSAB , M.MATALLAH , M.FELIACHI , Fixed-band hysteresis temperature control of induction cooking system, PRZEGLĄD ELEKTROTECHNICZNY, ISSN 0033-2097, R. 95 NR 9/2019

[10] Fabrizio Dughiero, ELECTROMAGNETIC PROCESSING OF MATERIALS TECNOLGIE DEI PROCESSI ELETTROTERMICI" Induction Heating: fundamentals" 2018

[11] P. Fabrègue, « Métallurgie du laminage à chaud»; Techniques de l'ingénieur. M7860, (2000).

[12] A. Le bon, « aspect -métallurgiques du laminage a chaud » ; nstitut de recherches de la sidérurgie 185, rue du pd Roosevelt, 78104st germain en laye.

Quadrotor control using cascaded feedforward linearization and LPV modeling

Achraf.M Senoussi
ICCC laboratory
University of Biskra
Biskra, Algeria

Mohamed Boumahrez
LMSE laboratory
University of Biskra
Biskra, Algeria

Aimen Bouaiss
LMSE laboratory
University of Biskra
Biskra, Algeria

Souri.M Mimoune
LMSE laboratory
University of Biskra
Biskra, Algeria

***Abstract*—This paper presents a real-time control scheme for quadrotors based on a cascaded model predictive control(MPC) architecture that uses linear parameter varying (LPV) and feedforward linearization techniques in the inner and outer layer, respectively. In the outer layer, the non-linear dynamics of the transitional control are linearized using feedforward linearization, followed by the implementation of a linear MPC controller. In the inner layer, the attitude control utilizes the LPV approach to formulate the Nonlinear model as a linear like with varying parameters. The effectiveness of the proposed control scheme is demonstrated in terms of tracking performance, computational time, and handling of varying parameters Through simulation using a high-fidelity simulator of a real UAV. Furthermore, a comparison with other similar approaches in the literature is included to showcase the advantages of the proposed scheme.**

***Index Terms*—MPC control, LPV modeling, Quadrotor control.**

I. Introduction

Quadrotor is one of the most popular UAVs. Their small size and lightweight make it capable of maneuvering in tight spaces that larger UAV cannot access. A quadrotor is an aircraft powered by four rotors that allow movement in 3D space and rotate in three directions. This actuator configuration makes the quadrotor an under-actuated nonlinear system with six degrees of freedom and four control inputs. The overall lifting force and the three possible torques are induced by the motor speed variations. Which creates challenges for maintaining stability under different operating conditions. Accordingly, it is necessary to design controllers based on an efficient optimal methodology to ensure stability while taking into account the complex dynamic behavior and physical actuator limitations.

A considerable amount of research has been carried out in the UAV control, considering several control strategies ranging from linear approaches like PID and LQR [3] to nonlinear approaches such as sliding mode control [2]. Recently, intelligent control such fuzzy logic and neural network [7] learning have also been considered. However, these methods are not capable of explicitly considering the quadrotor constraints.

In this sense, model predictive control has emerged as the most appropriate control technique for tackling this issue. In fact, MPC is able to handle linear and non-linear MIMO constrained dynamics. However, the model complexity may lead to high computational time. Which prevents real time application. Consequently, a trade-off between the performance and model complexity should be achieved. In response to these challenges presented by current controllers, we propose a cascaded approach in order to split the control problem into transitional and attitude systems. then, two MPC controllers implemented based on feedforward linearization and linear parameter varying model (LPV) approaches for position and attitude control, respectively. LPV describes nonlinear systems as linear with varying parameters. Ensuring more robustness to linear controllers while still being computationally efficient. which is broadly used for quadrotor control. for instance, The authors in [1] utilized a centralized MPC controller applied for autonomous racing vehicles. where the dynamics are described as an LPV model. Another work used a combination of feedback linearization and LPV in cooperation with LQR based on linear matrix inequalities (LMIs) for Position-Heading quadrotor control [6]. Additionally, Many works examined LPV modeling for fault tolerant control [4], [5].

The remainder of the paper is organized as follows: Section 2 provides a description of the quadrotor model. In Section 3, we present an overview of the overall proposed control scheme. In Section4, we present the results obtained from our case study and compare them with alternative approaches found in the literature. Finally, Section 5 concludes the paper by summarizing our findings and outlining potential directions for future research.

II. Quadrotor case study

The quadrotor dynamics model can be obtained using the Newton-Euler approach as follows

$$\begin{aligned}
\ddot{x} &= (\cos\phi\sin\theta\cos\psi + \sin\phi\sin\psi)\frac{U_1}{m} \\
\ddot{y} &= (\cos\phi\sin\theta\sin\psi - \sin\phi\cos\psi)\frac{U_1}{m} \\
\ddot{z} &= -g + \cos\phi\cos\theta\frac{U_1}{m} \\
\ddot{\phi} &= \dot{\theta}\dot{\psi}\frac{I_y - I_z}{I_x} - \frac{J_{TP}}{I_x}\dot{\theta}\Omega + \frac{U_2}{I_x} \\
\ddot{\theta} &= \dot{\phi}\dot{\psi}\frac{I_z - I_x}{I_y} + \frac{J_{TP}}{I_y}\dot{\phi}\Omega + \frac{U_3}{I_y} \\
\ddot{\psi} &= \dot{\phi}\dot{\theta}\frac{I_x - I_y}{I_z} + \frac{U_4}{I_z}
\end{aligned} \tag{1}$$

where $[x, y, z]$ denotes the position of the quadrotor in E-frame, and $[\phi, \theta, \psi]$ describes the quadrotor orientations in E-frame, with roll, pitch and yaw angles, respectively. On the other hand, (p, q, r) represents the angular velocities in B-frame. g, m are the gravitational acceleration and the quadrotor mass, respectively. $I = diag(I_x, I_y, I_z)$ denotes the moments of inertia regarding x, y, z axes, respectively. J_{TP} denotes the rotor inertia, and $\Omega = -\Omega_1 + \Omega_2 - \Omega_3 + \Omega_4$ presents the algebraic sum of the four propeller speeds, assuming the quadrotor is a six-degrees-of-freedom rigid body. U_1 is the thrust force along z axis while U_2, U_3, U_4 are the torque applied to x, y, z axis, respectively, obtained by varying the rotor speeds. Those control inputs are proportional to the square of the rotor speeds according to the following drive map matrix

$$\begin{bmatrix} U_1 \\ U_2 \\ U_3 \\ U_4 \end{bmatrix} = \begin{bmatrix} c_T & c_T & c_T & c_T \\ 0 & -lc_T & 0 & lc_T \\ -lc_T & 0 & lc_T & 0 \\ -c_Q & c_Q & -c_Q & c_Q \end{bmatrix} \begin{bmatrix} \Omega_1^2 \\ \Omega_2^2 \\ \Omega_3^2 \\ \Omega_4^2 \end{bmatrix} \quad (2)$$

The parameter values employed in the quadrotor model for the considered quadrotor case study (AScTec Hummingbird) are presented in [6].

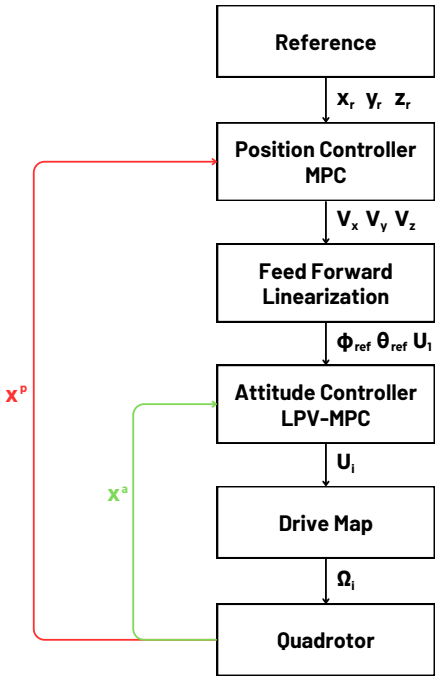

Fig. 1. Complete quadrotor multilayer control scheme.

III. Control Approach

Based on the previous model equations, the system dynamics is naturally separated into a hierarchy of two independent nonlinear subsystems. The first sub-system derived from the lower three equations in (1) defines the attitude system ruled by the control inputs (U_2, U_3, U_4). While the upper three equations in Eq. (1) to describe the transitional system with U_1 serving as a control input. The coupling appears in the translation system equations via the control orientations, while Ω establishes the coupling in the attitude system. Benefiting from the separation between transitional and attitude subsystems, a multilayer control scheme is proposed to control the quadrotor as shown in Figure 1. Firstly, the outer control loop tracks desired position (x_r, y_r, z_r) by generating the linearized control inputs (V_x, V_y, V_z). Then, the feedforward linearization Block transforms These inputs into the first control input U_1 together with feasible desired angles (ϕ_r, θ_r). These angles are fed along with the desired ψ_r to the inner control loop, which generates the proper torques (U_2, U_3, U_4) to guarantee attitude control. Finally, the control signals are transformed into rotor speeds Ω_i using an inverse calculation of Eq. (2). Eq. (3) present Attitude LPV model while Eq. (4) describe the linearized position model.

$$\boldsymbol{A}^a(\boldsymbol{\Gamma}) = \begin{bmatrix} 0 & 1 & 0 & 0 & 0 & 0 \\ 0 & 0 & 0 & -\frac{\gamma_3 \cdot J}{I_x} & 0 & \gamma_2 \cdot \frac{I_y - I_z}{I_x} \\ 0 & 0 & 0 & 1 & 0 & 0 \\ 0 & \frac{\gamma_3 \cdot J}{I_y} & 0 & 0 & 0 & \gamma_1 \cdot \frac{I_z - I_x}{I_y} \\ 0 & 0 & 0 & 0 & 0 & 1 \\ 0 & \frac{\gamma_2}{2}\frac{I_x - I_y}{I_z} & 0 & \frac{\gamma_1}{2}\frac{I_x - I_y}{I_z} & 0 & 0 \end{bmatrix}$$

$$\boldsymbol{B}^a = \begin{bmatrix} \frac{1}{I_x} & 0 & 0 \\ 1 & 0 & 0 \\ 0 & 0 & 0 \\ 0 & \frac{1}{I_y} & 0 \\ 0 & 0 & 0 \\ 0 & 0 & \frac{1}{I_z} \end{bmatrix} \qquad \boldsymbol{C}^a = \begin{bmatrix} 1 & 0 & 0 & 0 & 0 & 0 \\ 0 & 0 & 1 & 0 & 0 & 0 \\ 0 & 0 & 0 & 0 & 1 & 0 \end{bmatrix} \quad (3)$$

$$\boldsymbol{A}_p = \begin{bmatrix} 0 & 1 & 0 & 0 & 0 & 0 \\ 0 & 0 & 0 & 0 & 0 & 0 \\ 0 & 0 & 0 & 1 & 0 & 0 \\ 0 & 0 & 0 & 0 & 0 & 0 \\ 0 & 0 & 0 & 0 & 0 & 1 \\ 0 & 0 & 0 & 0 & 0 & 0 \end{bmatrix} \qquad \boldsymbol{B}_p = \begin{bmatrix} 0 & 0 & 0 \\ 1 & 0 & 0 \\ 0 & 0 & 0 \\ 0 & 1 & 0 \\ 0 & 0 & 0 \\ 0 & 0 & 1 \end{bmatrix}$$

$$\boldsymbol{C}_p = \begin{bmatrix} 1 & 0 & 0 & 0 & 0 & 0 \\ 0 & 0 & 1 & 0 & 0 & 0 \\ 0 & 0 & 0 & 0 & 1 & 0 \end{bmatrix} \quad (4)$$

IV. Results

In order to assess the efficiency of the proposed approach, closed-loop simulations have been carried out including the motor dynamics using MATLAB/SIMULINK environment. Runge-Kutta integration (ode45) was used with a discretization time of 0.01s (100 Hz).

Comparison is evaluated based on both computation time and mean square tracking error (MSE) with two other schemes: Scheme 2, where the same combination of feedforward linearization and LPV are used together with LMI LQR.

Scheme 3 based on a cascaded nonlinear MPC without accounting for the gyroscopic effect due to the extra complexity.

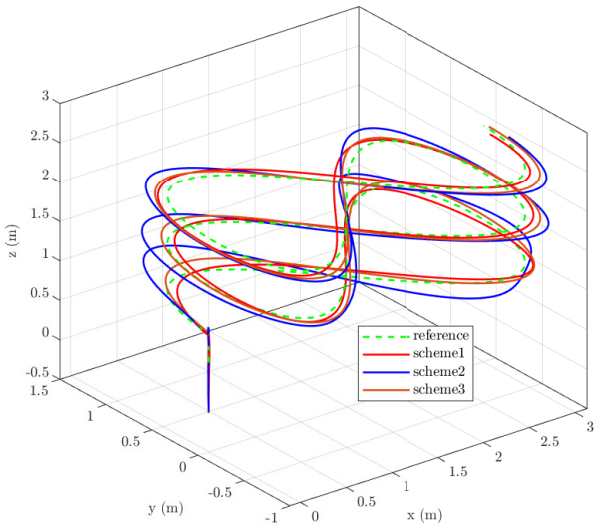

Fig. 2. Quadrotor trajectory

TABLE I
TRACKING PERFORMANCE COMPARISON

scheme	POS MSE (cm^2)	ATT MSE (deg^2)
Proposed scheme	78.47	2.1
LQR-based scheme	553.19	2.8
Cascaded NMPC	91.30	5.66

TABLE II
COMPUTATIONAL TIME PER ITERATION

scheme	position (ms)	attitude (ms)
Proposed scheme	1.5	1.6
LQR-based scheme	$1.7 \cdot 10^{-4}$	$3.9 \cdot 10^{-4}$
Cascaded NMPC	17.01	6.96

Figure 2 shows the trajectory tracking for the different schemes, while Table I illustrates position-heading reference tracking results. The results clearly demonstrate that the quadrotor controlled by the second scheme, which uses LQR-based LMIs in both loops, is significantly inferior in comparison to the other two schemes. On the other hand, Scheme 1 and Scheme 3 are able to closely follow the desired reference trajectory. In general, The proposed scheme over performed both other schemes.

Table II presents the computational time required for each control loop. The results indicate that both the feedforward linearization MPC and LPV-MPC required significantly less computational time over NMPC. In general, the LQR scheme was the most efficient in terms of computational time, although it presents worst performance and does not respect the physical constraints regarding control inputs and states.

V. CONCLUSION

This paper has proposed a cascaded MPC for quadrotor control based on linear parameter-varying modeling approach and feedforward linearization. The considered control-oriented model has been used into two cascaded model predictive controllers, achieving accurate position and attitude tracking while maintaining low computational cost. The results demonstrate the effectiveness of the proposed control scheme in comparison to LQR-based scheme and cascaded NMPC in terms of tracking error and computational time. These findings suggest that the proposed control scheme is a promising scheme for quadrotor control. Future research will focus on incorporating the state estimator and considering disturbances.

REFERENCES

[1] Eugenio Alcalá, Vicenç Puig, Joseba Quevedo, and Ugo Rosolia. Autonomous racing using linear parameter varying-model predictive control (lpv-mpc). *Control Engineering Practice*, 95:104270, 2020.

[2] Dhafer J. Almakhles. Robust backstepping sliding mode control for a quadrotor trajectory tracking application. *IEEE Access*, 8:5515–5525, 2020.

[3] Vahid Safari Dehnavi and Masoud Shafiee. The design of fractional i-lqr controller for constrained quadrotor using grasshopper optimization algorithm. In *2022 30th International Conference on Electrical Engineering (ICEE)*, pages 994–999, 2022.

[4] Julio Alberto Guzmán-Rabasa, Francisco Ronay López-Estrada, Brian Manuel González-Contreras, Guillermo Valencia-Palomo, Mohammed Chadli, and Madain Pérez-Patricio. Actuator fault detection and isolation on a quadrotor unmanned aerial vehicle modeled as a linear parameter-varying system. *Measurement and Control (United Kingdom)*, 52:1228–1239, 2019.

[5] Johannes Stephan, Lorenz Schmitt, and Walter Fichter. Linear parameter-varying control for quadrotors in case of complete actuator loss. *Journal of Guidance, Control, and Dynamics*, 41(10):2232–2246, 2018.

[6] Carlos Trapiello, Vicenç Puig, and Bernardo Morcego. Position-heading quadrotor control using lpv techniques. *IET Control Theory Applications*, 13:783–794, 2019.

[7] Zhiye Zhao and Xiaozheng Jin. Adaptive neural network-based sliding mode tracking control for agricultural quadrotor with variable payload. *Computers and Electrical Engineering*, 103:108336, 2022.

Modeling and Evaluating of Solid Oxide Fuel Cell Performance using Trap-designed Interconnects

Aimen Bouaiss
LMSE laboratory
University of Biskra
Biskra, Algeria

Souri.M Mimoune
LMSE laboratory
University of Biskra
Biskra, Algeria

Achraf Senoussi
ICCC laboratory
University of Biskra
Biskra, Algeria

Lotfi Khene
LMSE laboratory
University of Biskra
Biskra, Algeria

Lotfi Aloui
LMSE laboratory
University of Biskra
Biskra, Algeria

***Abstract*—This study explores the optimization of SOFC performance through trap-designed interconnects, with the aim of improving mass transfer and electrochemical efficiency. Numerical investigations were conducted to assess the impact of trap parameters including the three-dimensional size (width, length, and height), on cell performance.**

The results demonstrate that trap design effectively resolves a common issue associated with straight interconnects: poor reactant distribution in under-rib areas. Increasing trap size enhances SOFC performance, with trap length identified as the primary contributor to improvement. However, widening traps beyond 0.3 mm does not result in further performance enhancements. The optimal configuration for a three-trap design is determined to be 12 mm in length, 0.3 mm in width, and 1 mm in height, resulting in a remarkable 14% increase in power output compared to conventional designs. By employing trap-designed interconnects, the analysis revealed a trade-off between electrical performance and mechanical strength, with a notable increase in electrolyte failure probability. The authors recommend incorporating support layers to enhance SOFC durability in response to these findings.

***Index Terms*—FEM modeling, Mass transfer, Solid oxide fuel cell, Failure probability**

I. Introduction

Solid Oxide Fuel Cells (SOFCs) hold significant promise in the transition towards clean energy. Beyond their established role in adjacent cells separation, electrical conduction, and durability, interconnects in SOFCs are increasingly recognized as critical design elements for optimizing cell performance [5], [6], [8]. Many researchers have explored novel approaches. For instance, Kong et al. [3] introduced a novel interconnect design called X-type interconnects. This design reduces the effective current path while also facilitating greater oxygen supply to areas beneath the ribs, addressing limitations experienced in conventional interconnects. Fu et al. [2] Also introduced a novel interconnect design named beam and slot interconnects (BSI). Their experimentation revealed that SOFC stacks equipped with BSI demonstrated remarkable reductions in contact, activation, and concentration losses by 96.4%, 8.5%, and 47.4%, respectively. Yan et al. [9] proposed a spiral-like interconnects for planar SOFCs. The novel structure has been confirmed to significantly improve mass transfer performance and fuel availability at the reaction area with an acceptable range of pressure drop. Chen et al. [1] proposed bi-layer interconnects enhancing the sofc output due to concentration overpotential reduction.

This paper introduces a novel interconnect design featuring rectangular trap grooves, as depicted in Figure 1, and presents a comprehensive study on the impact of flow channels with traps. The traps design is adapted to SOFC application to provide a remedy for a well-reported issue in SOFC literature, that is the poor reactants distribution underneath the rib area [3], [4], [7]. In this work, a fully coupled model for SOFC (electro-chemico-thermo-mechanical modeling) is presented and validated using experimental data from the literature. The traps design is analyzed to identify the optimal trap configuration and compare it with the conventional interconnects (base design) by assessing its effects on electrochemical performance, temperature, current distribution, and the mechanical stability of the cell structure.

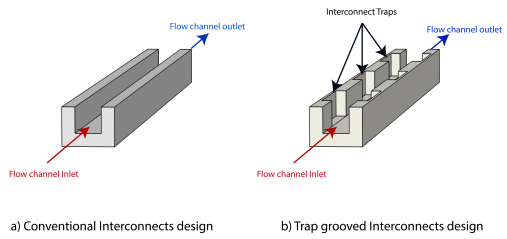

Fig. 1. Schematic comparison of SOFC interconnects: (a) base design, (b) traps design.

II. SOFC model description

A. SOFC geometry

In this study, a three-dimensional numerical model of a SOFC unit was developed using FEM software COMSOL Multiphysics. The model incorporates Ni-YSZ as the anode electrode, LSM-YSZ as the cathode electrode, YSZ serves as the ceramic electrolyte, and steel as the material employed for the interconnects. The employed SOFC structure is illustrated in Figure 2

B. Electrochemical reaction model

The charge-transfer rate for both anode and cathode reactions is defined by the Butler-Volmer equation as follows [10]:

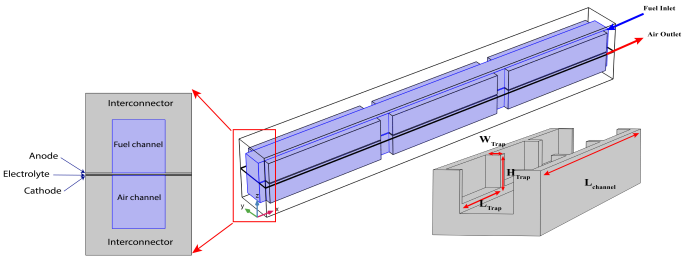

Fig. 2. Schematic of SOFC components and geometric dimensions

$$i_{v,a} = A_{v,a} \cdot i_0 \left(\frac{C_{\mathrm{H_2}}}{C_{\mathrm{H_2,ref}}} \exp\left(\frac{0.5F}{RT} \eta_{\mathrm{act},a} \right) - \frac{C_{\mathrm{H_2O}}}{C_{\mathrm{H_2O,ref}}} \exp\left(\frac{-1.5F}{RT} \eta_{\mathrm{act},a} \right) \right) \quad (1)$$

$$i_{v,c} = A_{v,c} \cdot i_0 \left(\exp\left(\frac{3.5F}{RT} \eta_{\mathrm{act},c} \right) - x_{O_2} \frac{C_{O_2}}{C_{O_2,\mathrm{ref}}} \exp\left(\frac{-1.5F}{RT} \eta_{\mathrm{act},c} \right) \right) \quad (2)$$

Here, a and c denote the index for anode and cathode, respectively. i_v (A/m^3) is the volumetric current density, A_v (m^2/m^3) is the Specific surface area. η_{act} is the activation overpotential. i_0 is the exchange current density measuring the kinetics of the electrochemical reaction.

C. Momentum and mass transport

Assuming fluid continuum in our model, Navier-Stokes equation and conservation of mass are solved simultaneously to define the velocity field and pressure in the gas channels. Gases flow is modeled by the weakly compressible flow, Ma $>$ 0.3, i.e. viscosity is not constant along the channel. conservation and Navier-Stokes equations are written as:

$$\rho \nabla \cdot u = 0 \quad (3)$$

$$|\nabla \cdot (\rho \vec{u} \vec{u})| = -\nabla p + \nabla \cdot \left[\mu \left(\nabla \vec{u} + \nabla \vec{u}^T \right) - \frac{2\mu}{3} (\nabla \cdot \vec{u}) I \right] + F \quad (4)$$

Given the study's objective to evaluate the enhancement of species transport using the traps-design interconnects, both gas diffusion and convection are employed within the model using the following equation:

$$\rho (u \cdot \nabla) \omega_i + \nabla \cdot j_i = R_i \quad (5)$$

Equation 5 could be broke down to different mass transport mechanisms (from left to right). The first term accounts for convection, where ω_i is the mass fraction. The second term represents the species diffusion, where j_i is the mass flux vector. R_i is the mass rate term of production/consumption of species in the active layers

D. heat transport model

$$\rho_{mix} \cdot c_p^{\mathrm{eff}} \cdot \overrightarrow{u} \cdot \nabla T = \nabla \left(\lambda^{\mathrm{eff}} \nabla T \right) + Q_{tot} \quad (6)$$

Where ρ_{mix} is the gas mixture density, c_p^{eff} is the effective heat capacity, ∇T is the temperature gradient, λ^{eff} is the effective thermal conductivity, and Q_{tot} is the total heat source/sink term

E. mechanical model

The total strain ε in this model is written as a sum of thermal strain ε_{th} and elastic strain ε_{el} , as follows:

$$\varepsilon = \varepsilon_{th} + \varepsilon_{el} \quad (7)$$

$$\varepsilon_{\mathrm{th}} = \alpha \left(\mathrm{T} - \mathrm{T_{ref}} \right) \quad (8)$$

Where α is the thermal expansion coefficient (TEC) and T_{ref} is the zero-stress temperature, which is set to 1073 K.

$$\sigma = D.\varepsilon_{\mathrm{el}} + \sigma_0 \quad (9)$$

Here, σ is the stress tensor, σ_0 is the residual stress mainly introduced by cooling cycles. D represents the elasticity matrix.

III. Results

Variation maps are depicted in Figure 4 to identify the optimal trap dimensions (length, width, height) for a three-trap interconnects design. This was achieved by fixing one parameter at a time and observing the resulting variations. The results indicate consistent performance improvement when increasing length and height to the maximum studied values. Meanwhile, increasing traps width beyond 0.3mm hinders the electrical performance of the cell. The results show that increasing traps length and height increases the SOFC performance consistently. In the other hand, increasing traps width boosts the electrical performance of the cell until reaching the optimal value which is 0.3mm, which after the output current density starts decreasing. The optimal traps design enhances the performance by a significant 14%, boosting the current density from 5078 A/m^2 in base design to 5907 A/m^2

Figure 3 presents a comparison of current and power density between the SOFC with the optimal traps design configuration ($N_{trap} = 3$, $L_{trap} = 6mm$, $W_{trap} = 0.3mm$, $H_{trap} = 1mm$) and the SOFC with base design.

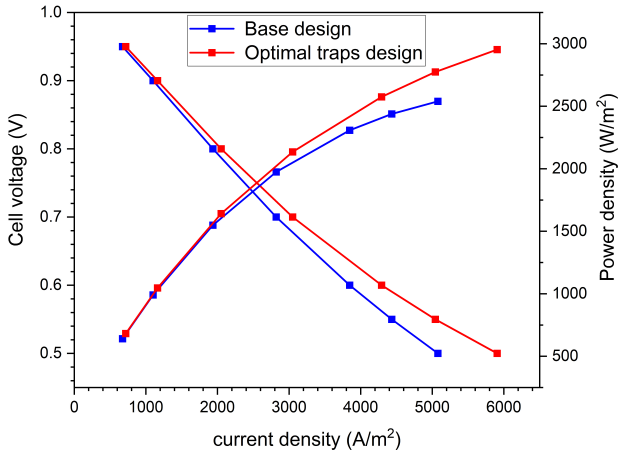

Fig. 3. Performance comparison between SOFC with base design and optimal traps design.

IV. Conclusion

In this paper, trap design interconnects are introduced for the first time in SOFCs and compared with conventional straight interconnects. A three-dimensional FEM model with fully coupled multiphysics was validated using experimental data to serve as the base case for performance comparison. Trap configuration of $N_{trap} = 3$ $L_{trap} = 12mm$, $W_{trap} = 0.3mm$, $N_{trap} = 1mm$, was selected after investigating variations in cell performance. This optimal trap design resulted in a 14% increase in average current density at 0.5 V. The trap design was found to address the issue of low reactant fractions under the ribs of interconnects, a problem widely reported by scholars. Additionally, it increased electronic distribution in that area, representing the shortest electron path.

References

[1] Qiuyang Chen, Qiuwang Wang, Jian Zhang, and Jinliang Yuan. Effect of bi-layer interconnector design on mass transfer performance in porous anode of solid oxide fuel cells. *International Journal of Heat and Mass Transfer*, 54(9–10):1994–2003, 2011.

[2] Quanrong Fu, Zhiyi Li, Wei Wei, Fengxia Liu, Xiaofei Xu, and Zhijun Liu. Performance enhancement of a beam and slot interconnector for anode-supported sofc stack. *Energy Conversion and Management*, 241:114277, 2021.

[3] Wei Kong, Zhen Han, Siyu Lu, Xiang Gao, and Xiaorong Wang. A novel interconnector design of sofc. *International Journal of Hydrogen Energy*, 45(39):20329–20338, 2020.

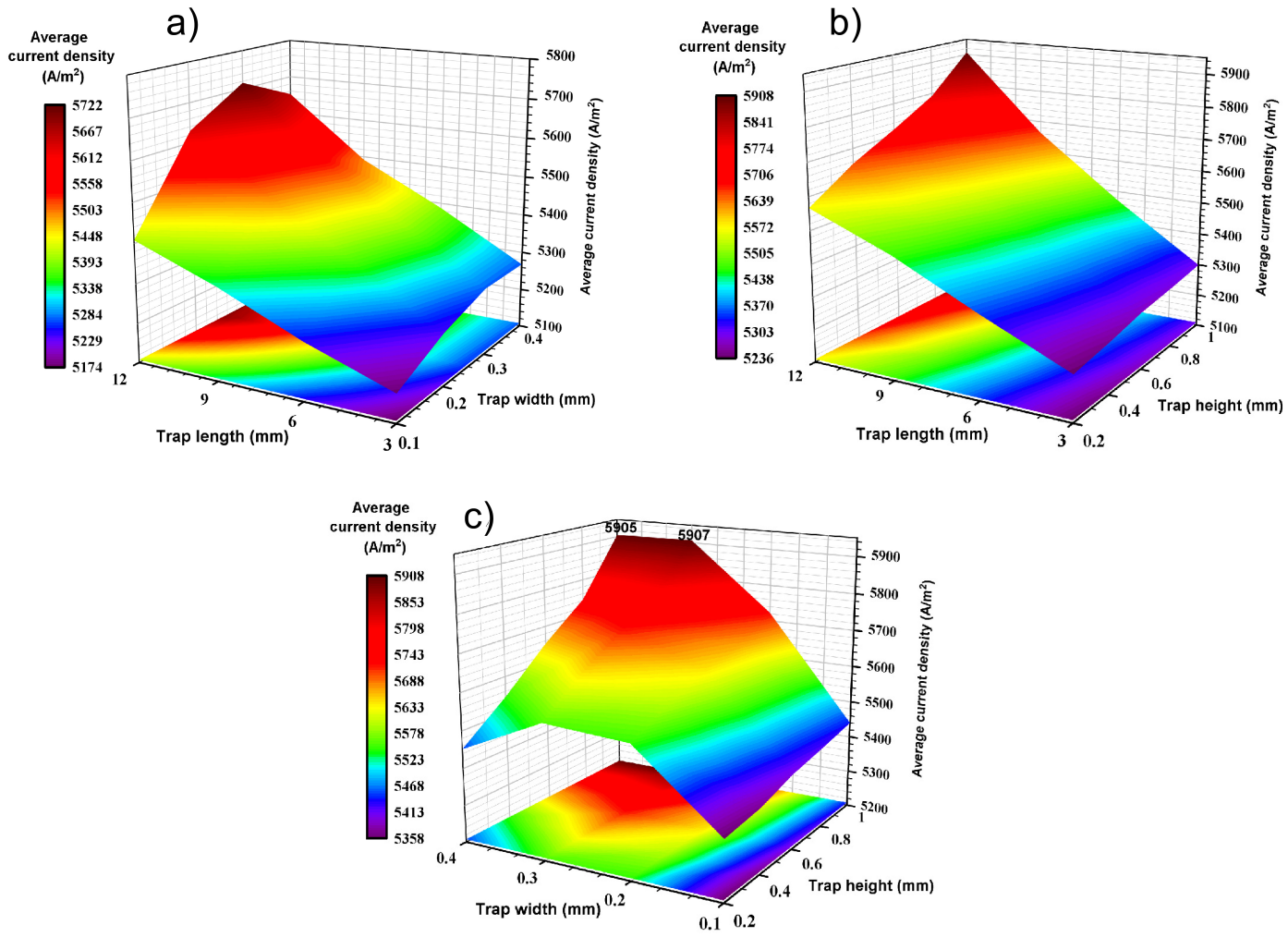

Fig. 4. SOFC cell performance at 0.5V with, (a) variation of traps length and width while fixing height at 0.6 mm, (b) variation of traps length and height while fixing width at 0.3, (c) variation of traps width and height while fixing length at 12 mm.

[4] Wei Kong, Jiayu Li, Shixue Liu, and Zijing Lin. The influence of interconnect ribs on the performance of planar solid oxide fuel cell and formulae for optimal rib sizes. *Journal of Power Sources*, 204:106–115, 2012.

[5] Manjunath Naik, K. Santhy, and B. Rajasekaran. Understanding early-stage oxidation mechanism of crofer 22 apu solid oxide fuel cell steel interconnect using glow discharge optical emission spectroscopy and grazing incidence x-ray diffraction. *Thin Solid Films*, 782:140043, October 2023.

[6] Roberto Spotorno, Fiammetta Rita Bianchi, Daniele Paravidino, Barbara Bosio, and Paolo Piccardo. Test and modelling of solid oxide fuel cell durability: A focus on interconnect role on global degradation. *Energies*, 15(8):2762, April 2022.

[7] Chen Wang, Zheng Li, Qijiao He, Meng Zhu, and Meng Ni. Effect of interconnector rib on optimization of sofc structural parameters. *Journal of The Electrochemical Society*, 169(9):094511, September 2022.

[8] Junwei Wu and Xingbo Liu. Recent development of sofc metallic interconnect. *Journal of Materials Science amp; Technology*, 26(4):293–305, April 2010.

[9] Min Yan, Pei Fu, Xiang Li, Min Zeng, and Qiuwang Wang. Mass transfer enhancement of a spiral-like interconnector for planar solid oxide fuel cells. *Applied Energy*, 160:954–964, 2015.

[10] Wenying Zhang, Wenchao Zhang, Xiong Kuang, Lichao Jia, and Dong Yan. Numerical optimization of obstacles channel geometry for solid oxide fuel cells. *International Journal of Hydrogen Energy*, 48(97):38438–38453, 2023.

Séminaire International " Modélisation Analytique et Numérique en Électrotechnique"

MANE'2024

Université Mouloud MAMMERI, 8-9 Juin 2024, Tizi-Ouzou, Algérie

Programme du Séminaire

Samedi 8 Juin 2024 8H30-10H	**Accueil des Participants**	
10H-11H	**Séance d'Ouverture**	
Samedi 8 Juin 2024 11H-11H40mn	**Plénière 1: Modélisation Analytique en Électronique de Puissance** Prof. Seddik Bacha, *Laboratoire G2ELab, INP Grenoble, France*	
Président: **Prof. M. R. Mékideche,** *Université de Jijel*, **Prof. A. Mekhaldi,** *Ecole National Polytechnique, Alger*		
Samedi 8 Juin 2024 11H40mn-12H40mn	**Session 1 (Orale): Numerical and Analytical Solution of PDEs (I)**	
Présidents : **Prof. T. Hacib,** *Université de Jijel,* **Prof. M. Rachek,** *Université de Tizi-Ouzou*		
01	Analytical 3D Magnetic Model Calculation for Halbach PM Planar Topology Considering Edge effect	Ammar Abdi, Youcef Ouazir, Oussama Khaled, **USTHB**
02	Modeling and Simulation of Turn-to-Turn Voltage Stress of Electrical Machine Winding Fed by Steep Fronted Pulses	N. Radja and M. Rachek **Univ. Tizi-Ouzou, Algeria**
03	Modeling of diffusion layer thickness variation of laminate in case of a current supply	[1]Yousfi Ghania, [1]Mohellebi Hassane, [2]GABI Yasmine **Univ. Tizi-Ouzou, Algeria** **[2]Fraunhofer Institute, IZFP, Germany**
04	Effect of Misalignment and Coil Diameter on Wireless Power Transfer in an Electric Vehicle	Ihab Anis Zergua, NaamaneMohdeb, Nabil Ikhlef,**Univ. Jijel, Algeria**
Samedi 8 Juin 2024 12H50mn	**Déjeuner**	
Samedi 8 Juin 2024 14H	**Après Midi**	
Samedi 8 Juin 2024 14H-14H40mn	**Plénière 2: Stratégie de Commande des Génératrices Penta-Phasées** Prof. Mourad Ait Ahmed, *Laboratoire IREENA,* *Ecole Polytechnique Nantes, France*	
Président: **Prof. S. Bacha,** *Laboratoire G2ELab, INP Grenoble, France*		
Samedi 8 Juin 2024 14H40mn-15H55mn	**Session 2 (Orale): Inductive, Smart sensors and actuators**	
Présidents : **Prof. D. Trichet,** *Laboratoire IREENA, France*, **Prof. S. M. Mimoune,** *Université de Biskra, Algérie*		
01	Inspection of surface defects on a composite material by the stochastic finite element model	Mahmoudi Thinhinane, Oudni Zehor **Univ. Tizi-Ouzou, Algeria**
02	Contribution to Characterisation of Unidirectional Carbon Fiber Reinforced Plastic (CFRP) Using High-Frequency Eddy Current Profiling Device Technology	Amirouche Harouz[1], Mohammed El Hadi Latreche[2], Henning Heuer[3,4], Hassene Mohellebi[1], **[1]Univ. Tizi-Ouzou, [2]Univ. Constantine, Algeria** **[3]Fraunhofer Institute, IZFP, Germany**
03	Capteur gravimétrique à ondes acoustiques de surface(SAW)	*Sait Smail[1,2]*, ***Univ. TiziOuzou,* USTHB, Algeria**
04	Numerical modelling of mircomagnetic methods in 3MA linear and non-linear Eddy current methods	Yasmine Gabi, Klaus Szielasko ***Fraunhofer Institute for non-destructive testing, Saarbrucken, Germany***

Samedi 8 Juin 2024 15H55-16H10mn	**Pause Café**	
Samedi 8 Juin 2024 16H10mn-17H10mn	**Session 3 (Orale): Semi-Analytical and Fast Resolution Methods**	
Présidents : **Prof. B. Maouche,** *Université de Béjaia***, Dr. Z. Oudni,** *Université de Tizi-Ouzou*		
01	New semi-analytical approach to study the interactions between conventional and superconducting coil	Roujaina Bougandoura, Hocine Bouchekhou, Ibrahim Hedouache and Hicham Allag, **University of Jijel-Algeria**
02	High Frequency Impedance computation of exciting coil using Coupled Electric Circuits Method	Ferroudaj Bouali, and Hassane Mohellebi, **Univ. Tizi-Ouzou, Algeria**
03	Elaboration de modèles semi-analytiques pour la récupération d'énergie	Badea Idir, Bachir Maouche, Sakina Zerguini **Univ. Béjaia, Algeria**
04	Modeling of Skin/Sensor Contact Impact on EEG Signals Encountred in Neurosciences	Assia Ait Hamou, Sara Sahraoui, Hassane Mohellebi, **Univ. Tizi-Ouzou, Algeria**

Dimanche 9 Juin 2024 8H30mn	**Arrivée des Participants**
Dimanche 9 Juin 2024 9H-9H40mn	**Plénière 3: Visualization of Magnrtic Flux Density, for Non Destructive Testing : A Brief Technical Review From Meters to Micrometers** Prof. Jinyi Lee *Department of Electronic Engineering, Chosun University* Gwangju, Republic of Korea
Président: **Dr. Y. Gabi** , *Fraunhofer Institute for Non- Destructive Testing, Germany*	

Dimanche 9 Juin 2024 9H40mn-10H40	**Session 4 (Orale): Numerical and Analytical Solutions of PDEs (II)**	
Présidents : **Prof. M. R. Mekideche,** *Université de Jijel,* **Prof. Y. Ouazir,** *USTHB*		
01	Modélisation 3D de l'influence des dépendances de la température ou du champ magnétique sur la courbe d'hystérésis dans les supraconducteurs à HTc	Khene Mohamed Lotfi, Lotfi Alloui, Benmebarek Fethi, Mimoune Souri Mohamed **Univ. Biskra, Algeria**
02	General Properties of Global and Blow-up Solutions For Parabolic Equation of Fractional Order	Bilal Basti, RabahDjemiat, **Univ.Djelfa, Univ. M'Sila, Algeria**
03	Transient hybrid model based on the strong coupling of magnetically coupled electric circuits and reluctance network	Yacine Messaoudi, M'hemed Rachek, Tarik Merzouki **Univ. Tizi-Ouzou, Algeria**
04	Analytical Modeling and Simulation of Self-excited Double Stator Induction Generator for Autonomous Operating Mode	Fatma Lounnas, Salah Haddad **Univ. Tizi-Ouzou, Algeria**
05	L'influence de la densité de courant *Jc* sur le comportement magnétothermique de limiteur du courant de défaut supraconducteur (SFCL)	Lotfi Alloui*, Khene Mohamed Lotfi, Mimoune Souri Mohamed, Benmebarek Fethi **Univ. Biskra**

10H40mn-10H50mn	**Pause Café**
Dimanche 9 Juin 2024 10H50-11H30mn	**Plénière 4: Modeling of Electromagnetic Phenomena Within Laminate Composite** Prof. Didier Trichet *Laboratoire IREENA,* *Ecole Polytechnique Nantes, France*
Président: **Prof. S. M. Mimoune**, *Université de Biskra, Algérie*	

Dimanche 9 Juin 2024 11H30mn-12H30mn	**Session 5 (Orale): Magnetic Material Modeling and Applications**	
Présidents : **Prof. L. Alloui,** *Université de Biskra***, Dr. Y. Gabi,** *Fraunhofer Institute for Non-Destructive Testing, Germany*		
01	Modeling of asymmetrical hysteresis minor loops using the Jiles-Atherton hysteresis model	Bachir Selmoune, Mourad Hamimid, Sofiane Aidel **University of Bordj Bou Arreridj, Algeria**
02	Information transport in ferromagnetic materials having cubic crystallizations	Rebiha Challali, Boualem Bourahla **Univ. TiziOuzou**
03	Effet de la Non-Linearité Magnétique sur l'Évaluation de l'Impédance d'un Dispositif CND	Mehaddene Hamid, Mohellebi Hassane **Université Mouloud Mammeri, Tizi-Ouzou, Algérie**
04	Influence of Magnetic Field on Spin waves Dispersion in	Ouiza Haddag, Ouahiba Nafa,Boualem

	Ferromagnetic Multilayers	Bourahla, **Univ. TiziOuzou, Algérie**
Dimanche 9 Juin 2024 12H30mn-13H30mn	**Déjeuner**	
Dimanche 9 Juin 2024 13H30mn	**Après Midi**	

Dimanche 9 Juin 2024 13H30-14H10mn	**Plénière 5: Fraunhofer NDT System and Numerical Simulation** Dr. Yasmine Gabi *Fraunhofer Institute for Non- Destructive Testing, Saarbrucken, Germany*
Président:	**Prof. D. Trichet**, Prof. Didier Trichet *Laboratoire IREENA, Ecole Polytechnique Nantes, France*

Dimanche 9 Juin 2024 14H10mn-15H20mn	**Session 6 (Orale): Electromechanical and Induction Devices**	
Présidents : **Prof. M. Ait Ahmed,** *Laboratoire IREENA, France* **Prof. H. Mohellebi,** *Université de Tizi_Ouzou, Algérie*		
01	2D Parametric Study of a DC Induction Heater for Aluminum Billets	Ibrahim Hedouache, Hocine Bouchekhou, Souri Mohamed Mimoune, Roujaina Bougandoura, Hicham Allag **Univ. Jijel**
02	Cooling of heat sink system using an active vibration piezoelectric beam and passive techniques using Al 2 O 3 nanofluid pumping	Bouttout Abdelouahab, Rouibah Nassir, **NCISB, Algiers, Algeria**
03	Bearing Fault Diagnosis Method based on EEMD and Quantile Weighted Permutation Entropy	Ahmed Taibi, Nabil Ikhlef, Lyes Aomar, **Univ. Jijel, Algeria**
04	Contrôle de la température pour le Laminage à chaud par le chauffage par induction	M. Rezig, K. Srairi **Univ. Biskra, Algeria**
05	Quadrotor control using cascaded feedforward linearization and LPV modeling	Achraf M. Senoussi, Mohamed Boumahrez, AimenBouaiss, Souri M. Mimoune **Univ. Biskra, Algeria**
06	Modeling and Evaluating of Solid Oxide Fuel Cell Performance using Trap-designed Interconnects	Aimen Bouaiss, Souri.M Mimoune,Achraf Senoussi, Lotfi Khene, Lotfi Aloui **Univ. Biskra**
Dimanche 9 Juin 2024 15H30mn-16H	**Séance Débats et Clôture**	
16H- 17H	**Visite Guidée**	

SOMMAIRE